SPECTROSCOPY OF REACTIVE MOLECULES AND CLUSTERS

Thesis by
Matthew S. Johnson

In Partial Fulfillment of the Requirements
for the Degree of
Doctor of Philosophy

California Institute of Technology
Pasadena, California

1996
(Submitted June 12, 1995)

Dedicated to Karin,
for her love and patience.

Acknowledgments

I am indebted to all of the scientists with whom it has been my pleasure to work at Caltech, especially the members of the Okumura research group. Jim Spotts is thanked for his friendship, and for sharing his love of the art of experimentation. I greatly enjoyed working with Keith Kuwata on the photoelectron and ion predissociation projects. I would like to thank my office mate Jong-Ho Choi for his hard work, counsel and assistance. Thank you to Yi-Bin Cao for his work in building the time-of-flight instrument, and for his steadfast dedication to scientific ideals. I will always remember Bermi Haas, Christine Nelson, Jessie Haldeman, Alex Wong, Teresa Moore and Timothy Minton who each helped in their own way. I reserve my deepest thanks for Professor Mitchio Okumura, who took me into his lab and shared his inspiration, ideas and dedication to excellence.

I would like to thank the members of my committee, Professors John Bercaw, Sunney Chan, Bill Goddard and Geoff Blake, for challenging me, and for offering their encouragement and support. In addition, Professor Jack Beauchamp's advice and humor were greatly appreciated. I might not have attended Caltech if it hadn't been for Professor Harry Gray, who invited me to the Macalester College Alumni House for a soda and a chat one cloudy winter day in 1989. I am indebted to the outstanding support staff in the Division of Chemistry. Tom Dunn, Ray Garcia and Guy Duremberg were always able to give time and attention to whatever problems needed solving.

I offer my heartfelt thanks to the people who were able to help me in preparing my thesis. Jim Spotts offered assistance from beginning to end, including help with

drawings, a floor to sleep on and food to eat. Keith Kuwata provided crucial assistance in compiling data and in performing calculations. Many thanks to the proofreaders, Chuck Williamson, Søren Pedersen, Jim Spotts, Keith Kuwata, Alex Wong, Teresa Moore, Karin Johnson and Ted DiMagno. I thank my family for their love and support. My best friend Tim McGuire has contributed more than he knows in many ways. Thanks also to all members of the Physical Chemistry soccer team past and future, and good luck against JPL! Finally, I would like to thank the W. R. Grace Company, the U. S. Department of Energy and the generosity of Mrs. Evelyn Bray for financial support of my studies.

"It is questionable if all the mechanical inventions yet made have lightened the day's toil of any human being."

John Stuart Mill

Principles of Political Economy

Abstract

This thesis presents spectroscopic investigations of reactive molecules and clusters. The techniques of laser excited fluorescence, infrared predissociation spectroscopy, and photoelectron spectroscopy were employed to investigate systems relating to fundamental cluster chemistry, ion solvation, and atmospheric ozone depletion.

An instrument was developed to investigate van der Waals complexes of refractory elements. A pulsed laser ablation cluster source harnessed the cooling power of a supersonic free jet to condense weakly bound neutral clusters. Laser excited fluorescence was used to characterize the products of the source, which included adducts of aluminum atoms with water molecules, hydrogen, and argon. The species $Al(H_2O)$, AlAr and AlH were identified.

The infrared predissociation spectra of positive and negative cluster ions were investigated using a tandem time-of-flight instrument. In this work the photofragment yield spectrum of mass-selected $I^-(H_2O)$ and $I^-(H_2O)_2$ complexes was measured between 3170 and 3800 cm^{-1}. The dominant features in the $I^-(H_2O)$ spectra were assigned as a hydrogen bonded OH stretch and a free OH stretch. *Ab initio* calculations were used to aid in spectral assignment and for geometrical information concerning $I^-(H_2O)$. Absorptions in the iodide water dimer cluster are attributed to a symmetric and an antisymmetric bonded OH stretch, and a free OH stretch.

Chlorine nitrate is a key reservoir of stratospheric chlorine, and as such its photolysis branching ratio is crucial to partitioning of species involved with stratospheric

ozone depletion. The He(I) photoelectron spectrum of chlorine nitrate was measured and assigned in order to understand the photodissociation behavior of chlorine nitrate. The results include the ionization potential of the molecule (10.86 eV), and the assignment of the first ionization peak to a nonbonding chlorine atomic orbital.

Table of Contents

Chapter 1:

Introduction to Spectroscopy of Reactive Molecules and Clusters

Water is the universal solvent and has always occupied a central position in the minds of chemists. Moore and Winmill first discussed the hydrogen bond, responsible for water's intriguing and unique properties as a solvent, early in this century (1911).[1] Linus Pauling stated that hydrogen bonded networks are among the most intriguing building blocks of nature. In *The Nature of the Chemical Bond*, Pauling discusses the problem of the structure of liquid water and proposes that it is likely that there are certain configurations of groups of water molecules that occur with high frequency.[2] According to this discussion, the hydrogen bond involves an electronegative atom which forms a bond with one of the hydrogens of the water molecule. It cannot be a standard chemical bond because the molecular orbitals are occupied, and so the interaction must arise from an electrostatic dipole (and other multipole) interaction. Due to recent advances in the science of chemical physics, we are now in a position to investigate the hydrogen bonding interaction through cluster spectroscopy.

As noted by Colson and Dunning, clusters between water molecules, and water with other chemical species can now be built and investigated one molecule at a time.[3] In this way the process of solvation can be viewed as a continuum extending from small

theoretically tractable systems all the way to bulk solutions. Since the introduction of supersonic expansions as a tool of optical spectroscopy by Smalley and coworkers, a great variety of van der Waals complexes have been investigated.[4]

The majority of this thesis is an investigation of the fundamental interaction between one or two water molecules and an ion (I^-) or an atom (Al). In chapter 2, the construction of a machine is detailed that was built to investigate van der Waals clusters. The first system to be studied using this machine is the interaction of an aluminum atom with a water molecule, the investigation of which is detailed in chapter 3.

In chapter 4 the construction of an infrared photofragment spectrometer is detailed, a machine that has been used in the Okumura group to study a wide variety of positive and negative ion-water clusters. In chapter 5 the first observation of the infrared spectra of the $I^-(H_2O)$ and $I^-(H_2O)_2$ clusters is detailed, including the assignment of the observed spectra to specific cluster geometries.

In chapter 6 a different topic is encountered. The photoelectron spectra of the chlorine nitrate ($ClONO_2$) molecule was recorded for on a machine which was rebuilt for the experiment. The study was motivated by a desire to understand the absorption spectrum of $ClONO_2$, a molecule that serves as a reservoir of reactive chlorine in the earth's stratosphere. The impact of the study on knowledge about the earth's ozone layer is discussed.

In addition to the above chapters, three appendices are offered. The first details a number of circuits that proved crucial to the execution of the experiments detailed in chapters 2 through 6. The second appendix is a listing of a program which was written to automate scanning and data collection for the photoelectron spectrometer. In the final

appendix an investigation of the SiH_7^+ cluster ion is presented. This ion was the first new system to be studied by the time-of-flight infrared predissociation spectrometer.

References

[1] T. S. Moore and T. F. Winmill, *J. Chem. Soc.* **101**, 1635 (1912).

[2] L. Pauling, *The Nature of the Chemical Bond*, University Press, Oxford (1940).

[3] S. D. Colson and T. H. Dunning, Jr., *Science* **256**, 43 (1994).

[4] R. E. Smalley, B. L. Ramanakrishna, D. H. Levy, and L. Wharton, *J. Chem. Phys.* **61**, 4363 (1974). R. E. Smalley, L. Wharton, and D. H. Levy, *J. Chem. Phys.* **63**, 4977 (1975).

Chapter 2:

Construction and Characterization of the Neutral Cluster Spectrometer

2.1 Abstract

A description is given for a new apparatus constructed to investigate van der Waals complexes of refractory elements. The machine employs a pulsed laser ablation cluster source which harnesses the cooling power of a supersonic free jet expansion to condense weakly bound neutral clusters. The necessary elements were constructed to employ laser induced fluorescence as a probe of the clusters generated by the source. The performance of the cluster source was characterized by looking at the fluorescence of a number of systems including Al, AlH, C_6H_6 and AlAr.

2.2 Introduction

The experimental apparatus was designed in our laboratory to allow the study of fundamental interactions of light atoms in a cluster environment. Initial experiments are to involve the study of the interatomic potentials between aluminum, lithium, and boron atoms and H_2O, H_2, and D_2 "solvents." The studies presented in this chapter represent the first of these systems to be probed with our apparatus. The components of the apparatus are detailed in the following sections. An overview of the experiment is given in fig. 2.1.

2.3 The Refractory Atom Neutral Cluster Spectrometer

The apparatus detailed in the following sections will allow the creation and characterization of neutral clusters of refractory element atoms in a cluster environment.

2.3.1 Pulsed Valve and Gas Inlet System

The design of the pulsed valve follows that of Proch and Trikl,[1] who describe a robust and versatile piezoelectric valve capable of producing fully developed flows at high repetition rates and short pulse widths. The front of the valve was modified from the original design to allow mounting of either a block for laser vaporization (section 2.3.2) or an extended cryogenic source. A drawing of the modified pulsed valve front plate is given in fig. 2.2. In operation, a circular piezoelectric bimorph disk (Physik

Instrumente, University Model P-286.23) retracts back on a plunger, at the end of which is a small O-ring or Kel-F tip, from an orifice of 0.5 mm diameter. This allows a short pulse of gas to escape into the chamber. In the vacuum chamber the valve housing is supported by a triangular plate as shown in fig. 2.3. The piezoelectric element is driven by a high voltage pulse (typical characteristics 200 μs width by 350-800 V) and results in a gas pulse ~200 μs wide. A diagram of a circuit for driving the piezoelectric valve is given in appendix A. A Kal-Rez O-ring (Seal-Methods, Parker #003, AS-568A, compound 1050LF) was employed in the current experiments. In contrast to Viton and Buna, two other common O-ring materials, Kal-Rez does not swell in contact with aromatic hydrocarbons, is resistant to chemical attack, and has a longer lifetime due to the material's resistance to flattening and loss of elasticity.

In one of the first tests of the apparatus, the benzene fluorescence excitation spectrum was measured and found to match literature values.[2,3] In addition, by setting the laser to a resonance and varying the time delay between the pulsed valve and the LIF probe laser, the width of the gas pulse could be measured. For a minimum valve opening, fluorescence was seen for a period of 270 μs. This value serves as an upper bound to the gas pulse width, with the actual FWHM time estimated to be 200 μs. No bouncing or double opening of the valve was observed by this method. The valve has been operated with a variety of source gases (He, Ne, Ar, N_2) and seed molecules (benzene, water), and at backing pressures of up to ten atmospheres. No problems occurred except when the valve was operated with helium carrier gas. The voltage necessary to maintain a constant chamber pressure increased, until eventually the valve

would not open. According to the manufacturer, helium cannot be prevented from infiltrating the piezoelectric crystal. Discharge pathways are created which lead to dielectric breakdown of the crystal and permanent damage.

A simple stainless steel sourceline manifold was constructed to control gas flow into the pulsed valve. The regulated output of a gas cylinder may be attached directly to the manifold, or a system employing two mass flow controllers can be employed to provide a pre-set mixture of two gases. The controllers (Edwards 825-B) and a pressure transducer (MKS Baratron capacitance manometer, 0-10,000 Torr range, model 122AA-10000BB) are connected to a circuit that monitors the pressure and adjusts the flow accordingly; the ratio of mass flow between the two channels is always kept constant. In addition, the sourceline is connected to a mechanical pump (Alcatel 2008, 6 cfm) and a thermocouple gauge. A tee has been built to allow vapors of water or benzene liquid to be seeded into the carrier gas. The tee may be heated or cooled in a temperature bath to achieve a desired vapor pressure.

2.3.2 Laser Vaporization Source

The gas pulse flows into a channel where it sweeps over the surface of an aluminum rod. At a critical moment during this gas pulse a laser is fired at the aluminum rod, ablating aluminum atoms which are entrained and collisionally thermalized by the gas pulse. When the gas pulse exits the source it undergoes further supersonic expansion which leads to condensation of clusters around the aluminum

atoms. This source is a descendant of the laser ablation source developed by Smalley and coworkers.[4,5]

Following the direction of Costes *et al.*,[6] our source has been designed to maximize the production of atoms as opposed to clusters of the target element. Immediately after the pulsed valve stagnation region there is a channel of 1 mm diameter and 16 mm length through a black anodized aluminum block. The channel opens up into a region of 2.5 mm dia by 7.5 mm length, perpendicular to which is an aluminum rod (2024 aluminum alloy, 4.82 mm diameter). Views of the laser vaporization source may be seen in fig. 2.3 and fig. 2.4. The output of a Nd:YAG laser (Continuum Surelite I, 20 Hz) is doubled and then mixed to produce the third harmonic (355 nm) which is used to ablate the rod. Harmonic generation occurs in a temperature stabilized module (Quanta-Ray HG4-B), which has second, third, and fourth harmonic generation crystals. The harmonic generation is explained in chart 2.1. The fundamental and second harmonic (532 nm) beams are separated by a pair of high power dielectric mirrors (CVI, R_{max} 355 nm, T_{max} at 1064 nm and 532 nm). A periscope consisting of two high power dielectric mirrors transfers the beam from the laser table and into the vacuum chamber *via* a UV-grade lens (CVI, f = 700 mm). After the rod the expansion becomes a free supersonic jet, with concomitant cooling and cluster formation. The rod is translated and rotated by means of a special coupling to an 80-thread-per-inch screw. Rotary motion is provided to the screw by means of a stepping motor external to the chamber connected to a rotary motion feedthrough (MDC).

The ablation pulse (3-10 mJ/pulse @ 355 nm) creates a plasma whose temperature may reach 10,000 K. A two order of magnitude reduction in temperature is necessary to create weakly bound species such as AlAr (D_e of the ground state of AlAr is ~180 cm-1).[7] The mechanism of cooling is the supersonic expansion of the plume into the vacuum chamber.[8] The chamber was designed in order to assure the greatest possible pumping speed, in addition to serving as a flexible platform for a number of experimental techniques. Laser power levels were measured using a Scientech power meter (model AC2501 with AA30 analog indicator).

2.3.3 Vacuum Chamber

The main portion of the apparatus, housing the cluster source, consists of two specially designed chambers joined by an NW400 ISO coupling. The first of these is a four-way reducing cross, the second, a six-way cross (see fig. 2.5). Both are constructed of 3/16" thick stainless steel tubing and have a principal inner diameter of 12.75". The main function of the four-way cross is to serve as a beam stop chamber, allowing a second diffusion pump to be mounted to increase the total pumping speed. The laser vaporization cluster source resides in the six-way cross. The top flange of this chamber is a ten-inch ASA flange with a rotary motion feedthrough and window. Baffle arms and Brewster's angle windows (2 mm quartz), in addition to suprasil windows for the vaporization laser, are attached to NW400 ISO flanges on either side of the six-way cross. The front of the chamber has a mount for a skimmer (Beam Dynamics). Both chambers are pumped by cryo-trapped VHS-10 diffusion pumps with

Krytox pumping fluid. In contrast to traditional hydrocarbon oils, Krytox fluid, a perfluorinated polyether, is resistant to chemical attack by a wide range of compounds including oxidizing and halogenated species and reactive atoms such as Li and Al. Each diffusion pump is backed by a mist-trapped single stage direct drive Leybold-Hereaus mechanical pump (model S30A, pumping speed 30 cfm). This arrangement results in a pumping speed of approximately 8,000 *l*/s in the main chamber, and a base pressure of ~5 x 10^{-7} Torr. A second chamber downstream of the skimmer has been designed for use in REMPI or MATI studies. This chamber, a four-way reducing cross, is pumped by a baffled VHS-6 diffusion pump backed by an Alcatel ZT1030C pump (19 cfm), resulting in a pumping speed of 2400 *l*/s.

The laser vaporization source is mounted *via* the triangle plate on three 1" dia steel rods. The rods are attached to the skimmer plate, and the distance between the source and the skimmer may be varied by means of translating the triangle plate on bearing blocks. In addition, the entirety of the source chamber may be unbolted from the skimmer flange and rolled back to allow complete access to the cluster source. The source is attached to the skimmer plate, which is supported by the second chamber (not shown in fig. 2.5). The source chamber, weighing just under a ton, is supported on a rail system by bearing blocks (Thompson) and may be rolled back by the push of a finger. This access was of considerable importance in assembling and aligning the source.

2.3.4 Laser Induced Fluorescence Excitation

The species created by the laser vaporization source are probed by tunable UV radiation. On resonance with a transition (fluorescence quantum yield permitting), fluorescence emission is excited. This emission is focused onto a photomultiplier tube, and the electronic signal thus generated is sampled electronically and recorded by an A/D converter mounted in a PC (Keithley-Metrabyte DAS-1600). The program DYEDATA was modified from the original[9] and controlled scanning of the dye laser and data collection. Laser-induced fluorescence spectra of clusters were determined by scanning the wavelength of the UV laser and monitoring the fluorescence emission.

A three stage process was used to generate the tunable UV radiation. The foundation of the laser system is a two-crystal Nd:YAG laser (Continuum NY61-20). The laser has an injection seeder (Lightwave model SI-500). By seeding the oscillator cavity of the NY-61 with radiation from a temperature-stabilized cw single mode ring laser, single mode transform-limited operation will result. The oscillator is stabilized by a piezoelectric cavity mirror. Use of the injection seeder results in a narrower laser linewidth when frequency mixing is employed, as well as greater power, stability, and harmonic generation efficiency. The output of the oscillator cavity is amplified in a second Nd:YAG crystal, pumped by the same flashlamp as the first. The 1.064 μm radiation is frequency doubled to 532 nm in order to pump the dye laser. A summary of beam polarizations and crystal properties is given in table 2.1.

In the second stage, a dye laser (Continuum/Quantel TDL-51) generates light in the range of 844 nm to 532 nm. Different dyes (available from Exciton) are employed

to access this range. The two dyes of principal interest in this study are DCM which allows a tuning range of 607 nm to 676 nm, and LDS 698, which has a tuning range of 661 nm to 740 nm. These dyes allow pumping of the $s \leftarrow p$ transition of Al by mixing the dye laser output with residual IR, the $d \leftarrow p$ transition through frequency doubling. The dye laser employs a Moya cavity oscillator and two stages of amplification to achieve tunable radiation at a power of up to 60 mJ. The wavelength is controlled by a stepping-motor connected to a grating (2400 lines/mm) in the oscillator cavity. The stepping motor is driven by a card housed in a PC-AT. A program running on that computer allows the user to select a given output frequency or to conduct a predetermined frequency scan. In addition, the program can receive orders *via* the computer's COM port to allow another computer to control the operation of the dye laser.

In the third stage the UV extension system (Continuum UVX-3) allows doubling of the dye laser frequency, mixing of the frequency with residual 1.064 μm radiation, or doubling followed by mixing to generate near vacuum ultraviolet wavelengths. Crystal angles are controlled by tracking electronics. By picking off a fraction of the beam and focusing it onto two photodiodes, the electronics generate an error signal which is used to drive the stepping motor in the proper direction. Only when the dye laser power is high enough and the system is well aligned is the tracking system reliable. More often, when the scan is on the edge of the tuning curve, or mixing and doubling are employed simultaneously, manual tracking is necessary. A summary of the operation of the NY-61, TDL-51, and UVX-3 system, including

nonlinear optical crystals, frequency ranges, and beam polarizations is presented in table 2.1.

2.3.5 Fluorescence Detection

A series of prisms and mirrors brought the UV output of the laser system into the chamber such that the light was horizontally polarized. In this way, fluorescence in the vertical direction is optimized. The main source of noise in the experiment is laser light scattered directly into the detector (the second most important source of noise was plasma glow). Accordingly, a great amount of effort went into designing a system of baffles in order to minimize directly scattered light. This system employs five apertures of decreasing diameter (10, 8, 6, 4, and 2 mm) mounted in a tube that screws into the inside of the vacuum flange. An assembly drawing of the apparatus is given in fig. 2.6. In addition, Brewster's angle windows were used at the input and output windows of the chamber. At the output window, a Wood's horn prevented reflected light from going into the detector. Four irises were employed external to the chamber to collimate the beam. Even after a great deal of effort was expended on aligning the apertures and the beam, it was not possible to eliminate all of the directly scattered light. The addition of a black plate opposite the source from the field lens was seen to greatly reduce the directly scattered light. To give an example of the machine's sensitivity, it was possible to record the AlAr $B\ ^2\Sigma^+(4s)(v' = 4) \leftarrow X_1\ ^2\Pi_{1/2}(3p)(v'' = 0)$ transition at a signal-to-noise of 100 in 100 shots per point.

Fluorescence was collected by a field lens of 75 mm focal length (Corning 7940 UV grade) and 58 mm diameter located at a distance of ~ 8 cm from the interaction region. A second lens (f = 90 mm, Herasil) focuses the fluorescence through an iris to provide spatial filtering of the light (see fig. 2.5). In theory, only light originating on a line running between the interaction region and the iris is able to reach the detector. An aluminum mirror (Oriel, 51 mm dia.) directs the beam towards the photomultiplier tube (PMT). A third lens (f = 50 mm, 51 mm dia., Corning 7940) focuses the light onto the detector aperture. Just before the aperture is a mount for a filter. A 70 nm bandwidth interference filter centered at 400 nm (CVI F70-400-3, 25 mm dia), or a colored glass filter centered at 320 nm (CVI SVG-11-1.00), can be employed, depending on fluorescence wavelength, to eliminate a large portion of the plasma noise. The detector aperture may be varied between by a micrometer screw. The PMT mount was designed to be at the same position as the entrance to a Jarrell-Ash 0.5 m monochromator. The monochromator may be placed on top of the optical table to allow dispersed fluorescence studies to be conducted in order to probe the ground electronic state of cluster species. In this study a R372 PMT (Hamamatsu, 185-730 nm range, red enhanced bialkali photocathode) was used. A solar blind PMT is also available (Hamamatsu, 160 to 320 nm range, Cs-Te photocathode).

2.3.6 Electronics and System Operation

The output of the PMT is amplified by a homemade pre-amp, the circuit of which is given in appendix A. Models at gains of 14 dB, 30 dB, and 34 dB have been

constructed, and were used depending on the sensitivity requirements of the experiment. Special attention was paid to the elimination of stray capacitance and noise in these circuits to get rid of parasitic oscillations, which are always a problem in fast op-amps. The 30 dB gain amp has a rise time of 10 ns and a range of ±2.5 V. A 50 Ω terminator was used at the input of the pre-amp.

Two gated integrators (Stanford Research Systems model SR250) were used to extract the signal from the PMT response. One gate was set to capture the fluorescence signal and the second to integrate the plasma noise so that it could be subtracted from the raw data. By using a narrow gate width (~ 90 ns) on the fluorescence signal the contribution of plasma glow could be minimized. The detector response was monitored using an oscilloscope (Tektronix model TDS320, 2 channel, 100 MHz, 500 MS/s), that was also employed when setting the gated integrator gate delay and width. The output of the gated integrators was digitized by an A/D board resident in computer (Keithley-Metrabyte model DAS-1602).

An overview of the configuration of the electronics is given in fig. 2.1, which also indicates the flow of control in the experiment. Timing was controlled by two Stanford Research Systems digital delay generators (model DG-535). The delay generators trigger all of the other components of the machine starting with the pulsed valve and followed by the vaporization laser, the fluorescence laser, the gated integrators, and the A/D conversion. A typical timing setup is presented in fig. 2.7.

The program DYEDATA (Borland Turbo Pascal 7.0) was used to collect data and control dye laser scanning. It is a modified version of the program OPODATA

which was used to collect data in the time-of-flight experiment detailed in chapter 3. Analog-to-digital conversion was accomplished by a triggered data acquisition on a Keithley-Metrabyte DAS-1602 board, using single ended inputs in the range ±5 V. Because a significant amount of crosstalk was found between consecutive channels (up to one half of the signal applied to channel n would be seen on channel $n + 1$), channels 0, 2, and 4 were used. These channels were used for fluorescence signal, laser power, and plasma glow respectively. The operator enters the beginning and ending wavelengths of the scan, the number of shots to be averaged at each wavelength, and the wavelength step size between data points. The program controls the dye laser and accumulates the data, which can be saved to a file. This file in turn may be read directly into a spreadsheet program for data analysis.

2.3.7 Wavelength Calibration

Initial wavelength calibration of the dye laser was performed by steering the beam into a 0.5 m Jarrell-Ash monochromator. In this way the wavelength could be determined to within ~0.5 nm.

A more refined calibration of the dye laser wavelength was performed by the method of optogalvanic spectroscopy.[10] In this highly sensitive method, the output of the dye laser irradiates the region between the two electrodes of a standard neon glow lamp (GE-2J, General Electric, $0.13). When the laser is on resonance with an atomic transition of neon the current carrying capacity of the discharge is changed, because the population distribution of the various states has been altered. Transitions originating in

metastable states in Ne lead to positive voltage signals, while short-lived states lead to negative signals. The important variables are the pressure of neon gas, the separation of the electrodes and the discharge current. A DC power supply at ~100 V is attached to the bulb *via* a ballast resistor. A capacitor attached to this lead of the discharge couples a signal originating in voltage changes caused by changes in the current in the bulb. The signal is integrated, digitized, and stored on a computer. The 25 observed transitions based on the $2p^5 3p \leftarrow 2p^5 3s$ system of Ne cover most of the useful range of the dye laser, from 743.89 nm to 588.19 nm. A minimum resolution of 0.0068 nm (0.18 cm^{-1} at 622 nm) was achieved. In addition, the backlash of the sine drive in the dye laser oscillator grating was determined to be 0.015 nm. The dye laser has been calibrated based on a scanning direction of red to blue.

A thorough calibration was performed by measuring the laser induced fluorescence (LIF) spectrum of I_2. A few crystals of I_2 were placed in a glass cell; the air was then removed from the cell using a mechanical vacuum pump. Focusing of the laser beam was not necessary, but Brewster's angle windows were employed at the cell entrance and exit windows to reduce directly scattered light. The LIF was collected by a 1P28A photomultiplier tube, amplified, integrated, and digitized. A comparison of the measured LIF spectra with the I_2 spectral atlas[11] is presented in fig. 2.8. The advantage of using I_2 is that it provides an accurate wavelength determination over a similar region of the spectra (676 nm to 500 nm) with a high density of lines. The neon bulb averages 0.007 lines/cm^{-1} in the visible region, while I_2 provides 3 lines/cm^{-1}. The increased accuracy in calibration is well worth the extra effort of setting up the I_2 cell

and initially assigning the spectra. The spectra involves the $B\,^3\Pi^+_{ou} \leftarrow X\,^1\Sigma^+_g$ transition for $3 \leq v' \leq 62$ and $0 \leq v'' \leq 6$.

The most direct calibration method is to measure the atomic fluorescence spectrum of the material being ablated. Daily calibrations of the instrument were conducted based on transitions of the aluminum atom. Table 2.3 lists the wavelength and assignment of the relevant transitions.[12] The peaks are extremely intense and easily saturate the detector if precautions are not taken. In addition to their value in calibration, these peaks have been extremely important in optimizing the performance of the instrument.

2.4 Results

The following experiments were performed on the apparatus detailed in the previous section, with the intention of testing and characterizing the performance of the instrument. For the AlH system, the rotational temperature of the beam was minimized by systematically varying source conditions. In the case of AlAr, the ability of the machine to create a weakly bound metal-gas cluster and obtain its UV LIF spectrum was verified. The AlH results are discussed below, while the LIF spectrum of AlAr is presented in the following chapter.

2.4.1 The $A\,^1\Pi \leftarrow X\,^1\Sigma^+$ system of AlH

The beam temperature is of central importance in creating weakly bound species. By measuring the rotational envelope of the $A\ ^1\Pi$ (v' = 0) $\leftarrow X\ ^1\Sigma^+$ (v" = 0) transition of AlH, it was possible to determine the rotational temperature of this species created by chemical reaction of laser ablated Al atoms with H_2. A molecule in a free jet expansion may undergo 100 to 1,000 binary collisions.[13] High frequency vibrational modes of diatomic molecules typically require more than 10,000 collisions for relaxation, whereas rotational degrees of freedom require 1 to 100 collisions to become thermalized. Hence we would expect the rotational temperature to be the lowest, followed by the vibrational temperature. The electronic temperature will depend greatly on the specific state and its relaxation dynamics. Measured rotational temperatures often approach the internal temperature of the beam which is typically < 5 K.[14]

AlH was created by ablating a 2024 aluminum rod, combined with an expansion of pure H_2 gas at a backing pressure of 4500 Torr. AlH is formed through abstraction of a hydrogen atom from H_2 by an electronically excited Al atom. The heats of formation are as follows:[15]

$Al(^2D) + H_2$	170 kcal/mol
$Al(^2S) + H_2$	150 kcal/mol
AlH + H	114 kcal/mol
$Al + H_2$	78 kcal/mol

The reaction between Al and H_2 takes place in the high pressure gas channel of the source where the reaction products may be thermalized by collisions, and subsequently cooled by the supersonic expansion.

The LIF spectrum of the $A\ ^1\Pi \leftarrow X\ ^1\Sigma^+$ transition has been measured by Zhu, Shehadeh and Grant.[16] In this experiment a thin aluminum wire was wrapped around a tungsten filament. When the filament was resistively heated, the aluminum melted, wetting the surface of the tungsten. A pulse of H_2 gas resulted in formation of AlH at a rotational temperature of 650 K which was probed by laser induced fluorescence.

A typical AlH spectrum is given in fig. 2.9. Peak positions matched those predicted from accepted spectroscopic constants.[17] If a Boltzmann distribution of rotational temperature is assumed for AlH in the beam, integrated peak intensities may be used to determine the rotational temperature.

$$n_{(J=J')}/n_{(J=0)} = \exp(-\Delta E/kT)$$

$$T = -(\Delta E/k) * (\ln(n/n_0))^{-1}$$

where k is the Boltzmann constant, 0.6952 cm^{-1}/K, and n is the Hönl-London-normalized peak integral. For a Q-branch transition where $\Delta\Lambda = \pm 1$, the Hönl-London factor S_J^Q simplifies to $(2J+1)/4$ (here $J' = J''$), whereas for an R branch $S_J^R = 2 + J''$.[18]

The maximum of the plasma plume was initially observed at a delay time of 15 μs from the ablation pulse, with a FWHM of 3μs. This is significantly faster and

narrower than for any other source gas. Characteristic plume maxima for He, N_2, and Ar are ~ 25, ~ 50 and ~ 75 μs respectively. The temperature was first measured with a chamber pressure (corrected for the sensitivity of the gauge to H_2) of 4.3 x 10^{-5} Torr, and found to be ~ 70 K. (Chamber pressure is a linear function of the amount of gas flowing through the source.) The temperature was found to vary depending on the delay between the firing of the vaporization laser and the fluorescence excitation laser. Near the maximum of the plasma glow the temperature was hottest (60-100 K), whereas in the tail of the glow it decreased to ~20 K. The dependence of rotational temperature on LV-LIF delay time is presented in fig. 2.10*a*. When the pulsed valve was turned up to allow the maximum flow of H_2 through the source, the temperature decreased by a factor of 5 to 10-15 K. In this case (fig. 2.10*b*) the chamber pressure was 3.9 x 10^{-4} Torr. Two generalizations can be made from this experiment. The first is that the temperature of the beam drops significantly when the amount of gas going through the source is increased. The second is that colder beam temperatures may be found in the area of the tail of the plasma glow. In addition the total intensity of the peaks were seen to decrease for long vaporization-probe delay times. Consequently, there is a trade off between the colder temperatures of longer delay times and the attendant decrease in intensity.

Beam temperature and intensity were also measured as a function of the delay between the opening of the pulsed valve and the vaporization pulse. There was a strong dependence between peak intensity and valve-ablation delay time, intensities dropping off by a factor of 5 for delay times greater than 180 μs. One explanation is that there

could be too much gas present at long delays, which would prevent the plume of ablated material from expanding all the way into the channel; the plume would be 'blown out.' A weak dependence between pulsed valve-vaporization delay and temperature was found; the rotational temperature decreased for longer delay times. The best compromise is a delay of ~180 μs, where the temperature is at its minimum and the intensity has not yet fallen off.

2.5 Conclusion

A new apparatus has been constructed to investigate van der Waals complexes of refractory elements. The construction of a pulsed laser ablation cluster source which harnesses the cooling power of a supersonic free jet expansion to condense weakly bound neutral clusters has been detailed. Performance of the cluster source was characterized by the method of laser induced fluorescence.

2.6 References

[1] D. Proch and T. Trikl, *Rev. Sci. Instrum.* **60**(4), 713 (1989).

[2] E. Riedle, T. Knittel, T. Weber and H. J. Neusser, *J. Chem. Phys.* **91**(8), 4555 (1989).

[3] T. Suzuki and M. Ito, *J. Chem. Phys.* **91**(8), 4564 (1989).

[4] J. B. Hopkins, P. R. R. Langridge-Smith, M. D. Morse and R. E. Smalley, *J. Chem. Phys.* **78**, 1627 (1983).

[5] D. E. Powers, S. G. Hansen, M. G. Geusic, D. L. Michalopoulos and R. E. Smalley, *J. Chem. Phys.* **78**, 2866 (1983).

[6] M. Costes, C. Naulin, G. Dorthe, G. Daleau, J. Joussot-Dubien, C. Lalaude, M. Vinckert, A. Destor, C. Vaucamps and G. Nouchi, *J. Phys. E.: Sci. Instrum* **22**, 1017 (1989).

[7] M. J. McQuaid, J. L. Gole and M. C. Heaven, *J. Chem. Phys.* **92**(5), 2733 (1990).

[8] G. Scoles, ed., Atomic and Molecular Beam Methods, Vol. 1, Oxford, New York (1988).

[9] Y.-B. Cao, Ph.D. Thesis, California Institute of Technology (1994).

[10] G.-Y. Yan, K.-I. Fujii and A. L. Schawlow, *Optics Letters* **15**(2), 142 (1990). J. R. Nestor, *Applied Optics* **21**(22), 4154 (1982). B. Barbieri and N. Beverini, *Rev. Mod. Phys.* **62**(3), 603 (1990).

[11] S. Gerstenkorn and P. Luc, *Atlas du Spectre D'Absorption de la Molecule D'Iode*, Editions du Centre National de la Recherché Scientifique, Paris (1978).

[12] E. F. Worden in Line Spectra of the Elements, *CRC Handbook of Chemistry and Physics, 67th ed.*, R. C. Weast, ed., CRC Press, Boca Raton, 1986.

[13] D. R. Miller, "Free Jet Sources," in *Atomic and Molecular Beam Methods, vol. 1*, G. Scoles, ed., Oxford University Press, New York, 1988.

[14] R. D. Levine and R. B. Bernstein, *Molecular Reaction Dynamics and Chemical Reactivity*, Oxford University Press, New York, 1987.

[15] M. W. Chase, Jr., C. A. Davies, J. R. Downey, Jr., D. J. Frurip, JANAF Thermochemical Tables (3d ed.), *J. Phys. Chem. Ref. Data, Suppl. 1* **14**, 1 (1985). S. W. Benson, Thermochemical Kinetics, John Wiley, New York (1976).

[16] Y. F. Zhu, R. Shehadeh and E. R. Grant, *J. Chem. Phys.* **97**(2), 883 (1992).

[17] K. P. Huber and G. Herzberg, *Molecular Spectra and Molecular Structure IV. Constants of Diatomic Molecules*, Van Nostrand Reinhold, New York, 1979.

[18] H. Hönl and F. London, *Z. Physik* **90**, 712 (1925).

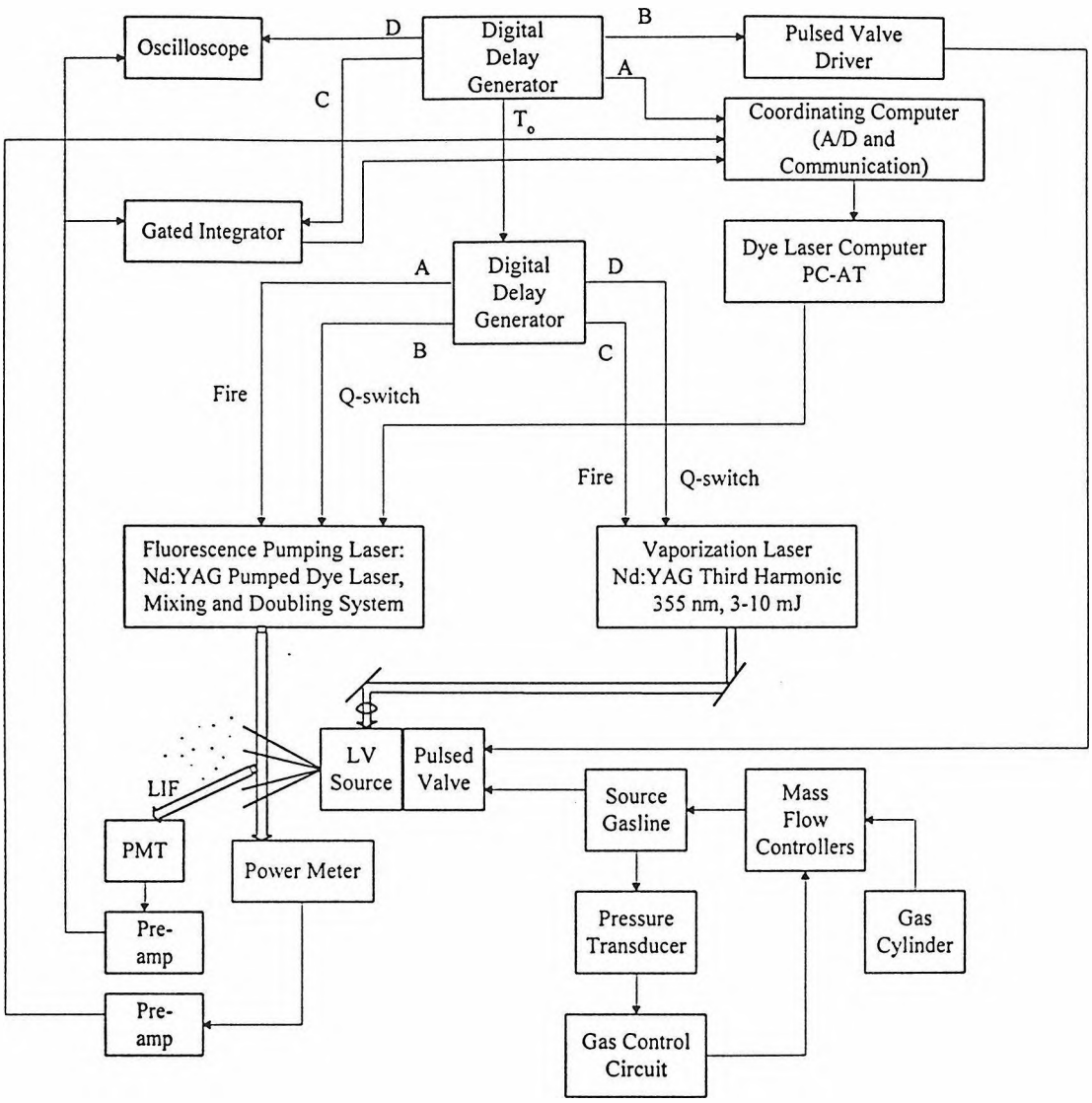

Figure 2.1 Schematic diagram of experimental apparatus.

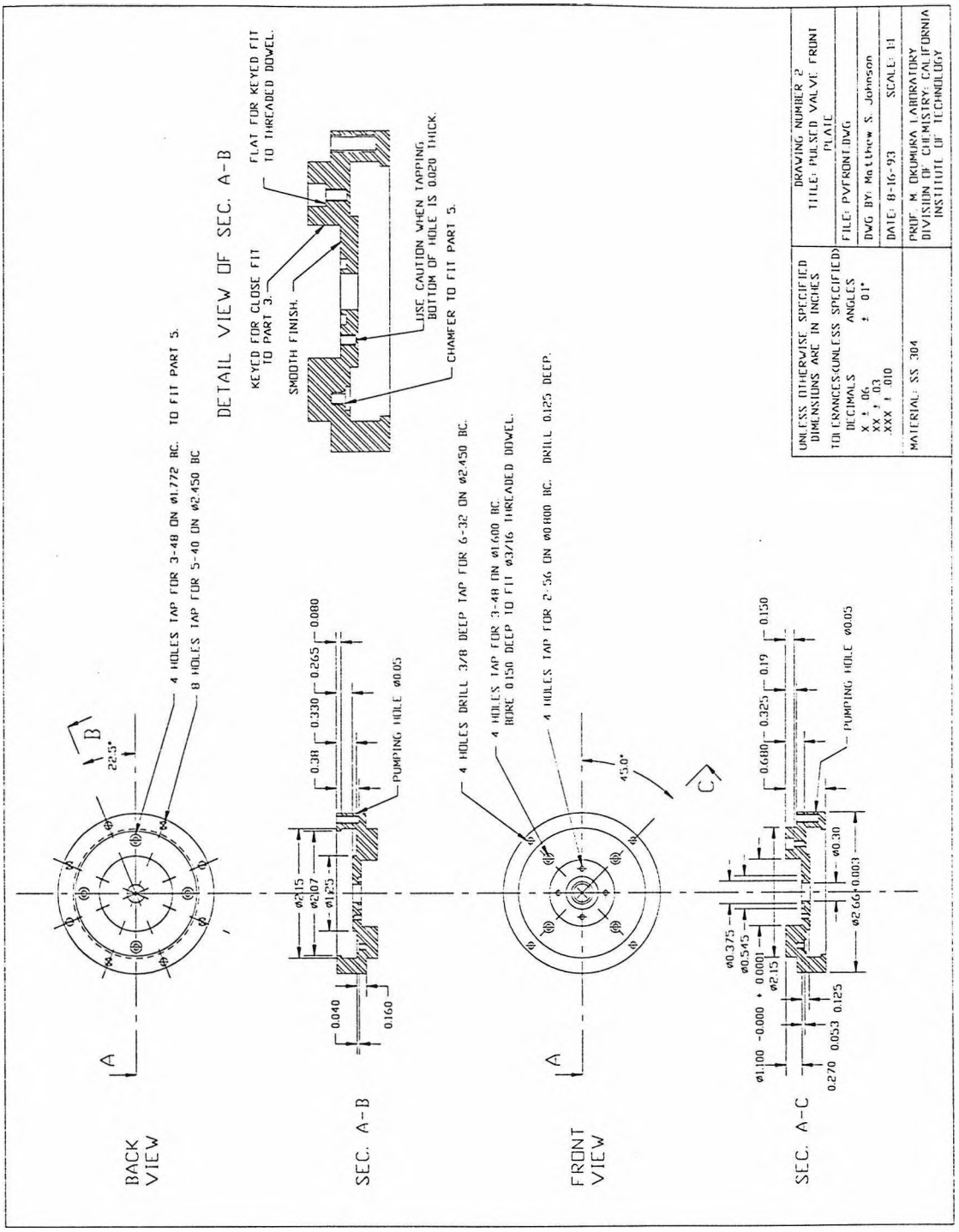

Figure 2.2 Drawing of modified front of piezoelectric valve.

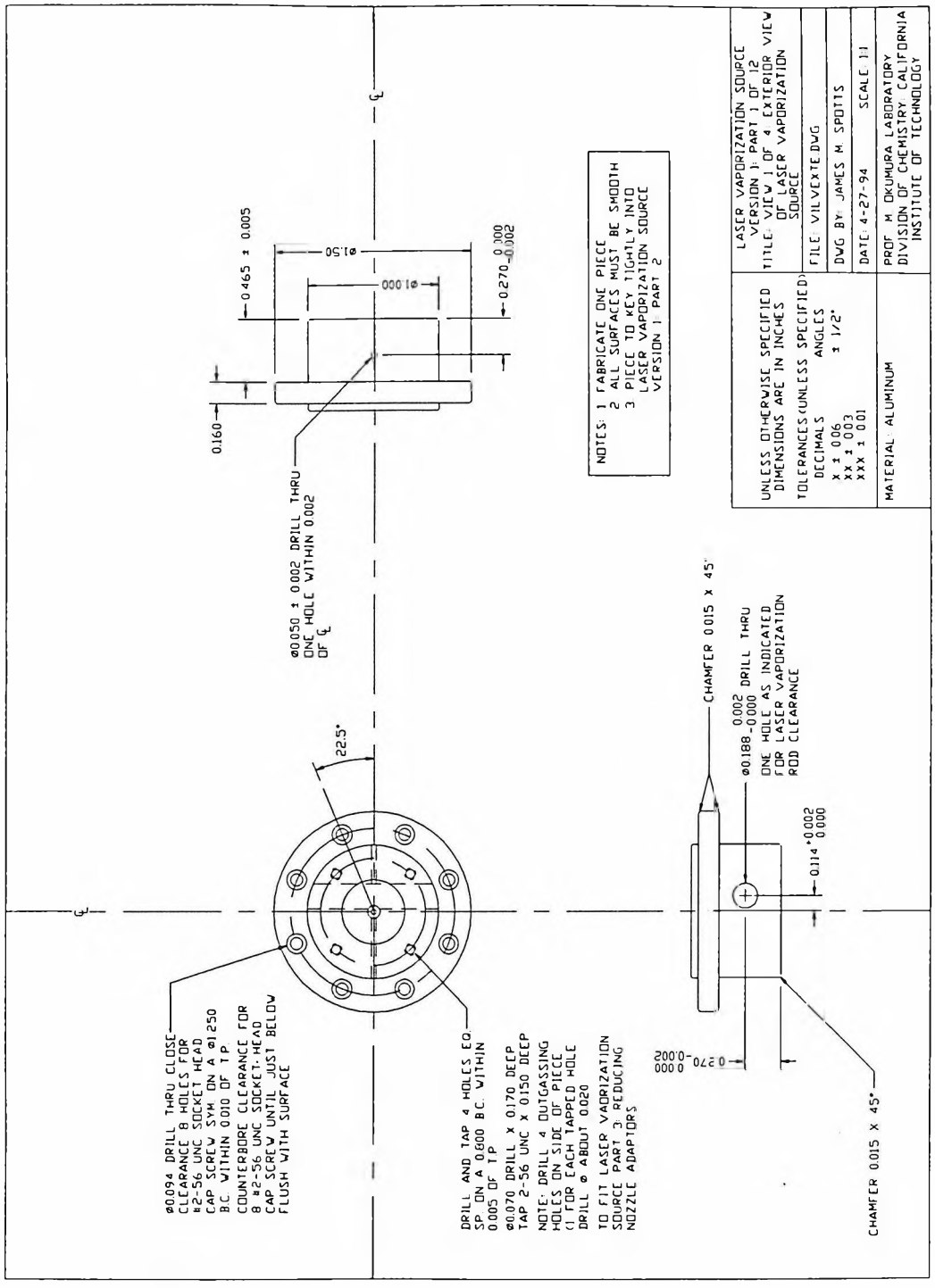

Figure 2.3 Exterior view of laser vaporization source.

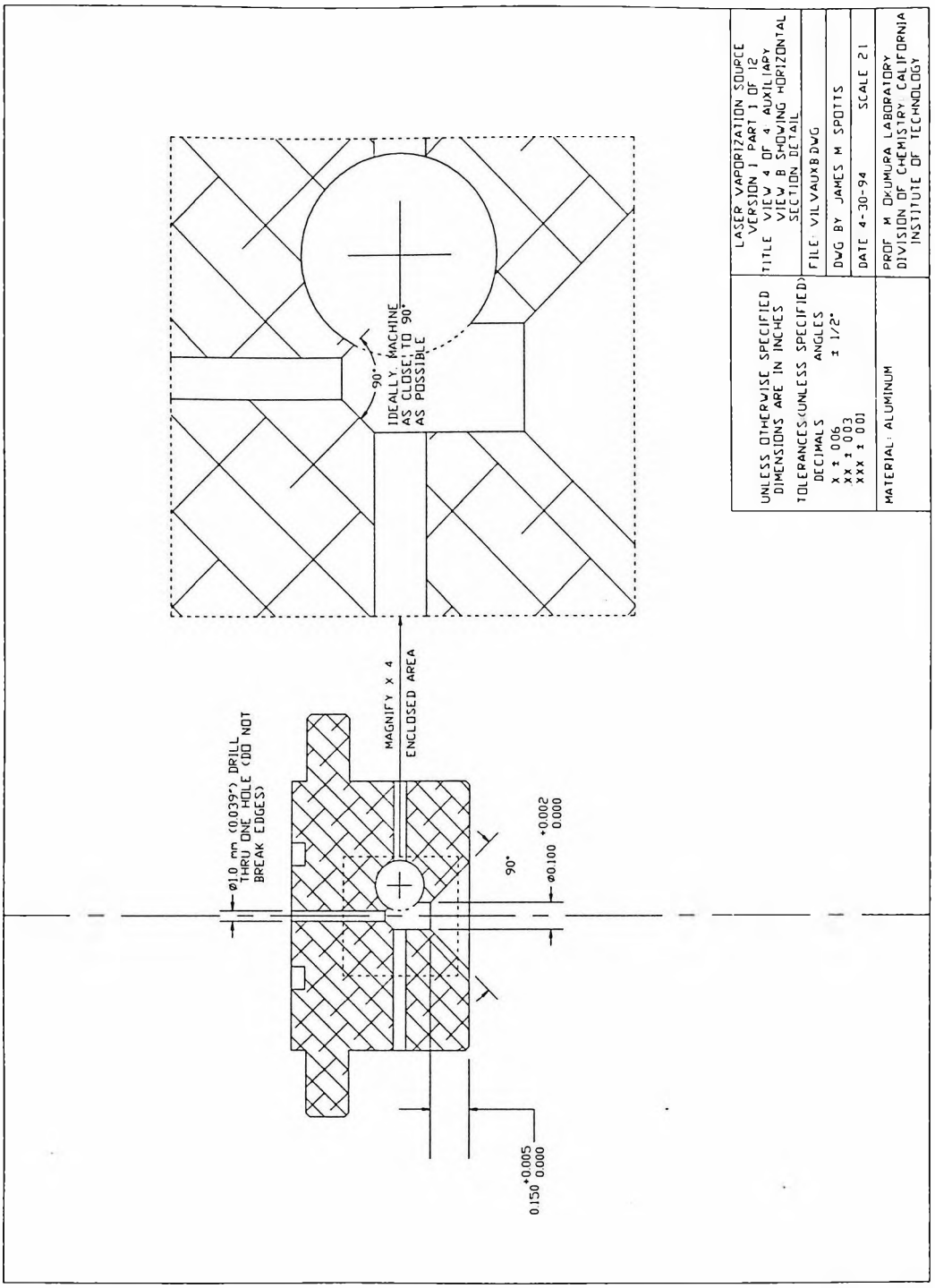

Figure 2.4 Horizontal section of laser vaporization source.

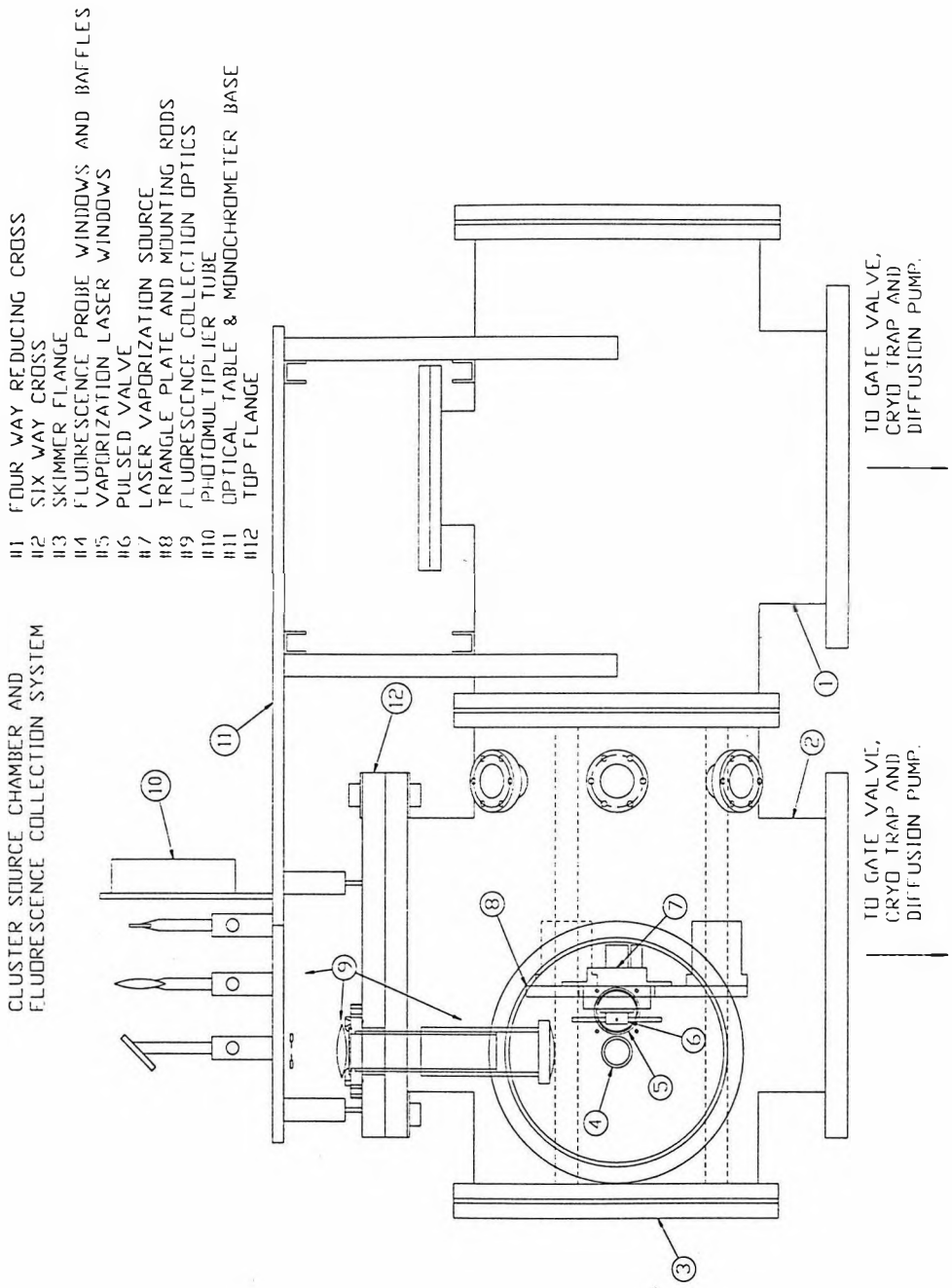

Figure 2.5 Side view of experimental apparatus.

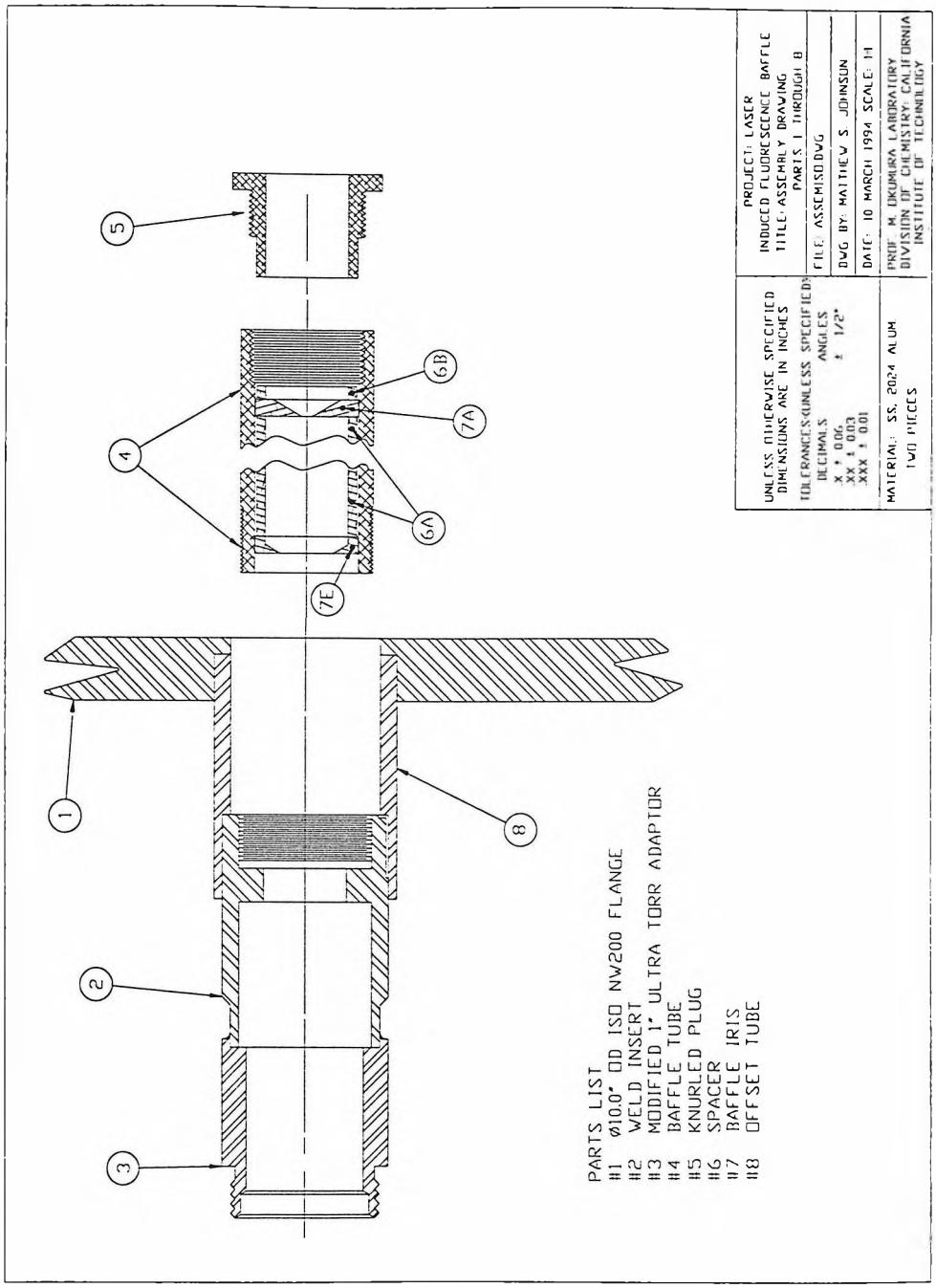

Figure 2.6 Assembly drawing of fluorescence baffles.

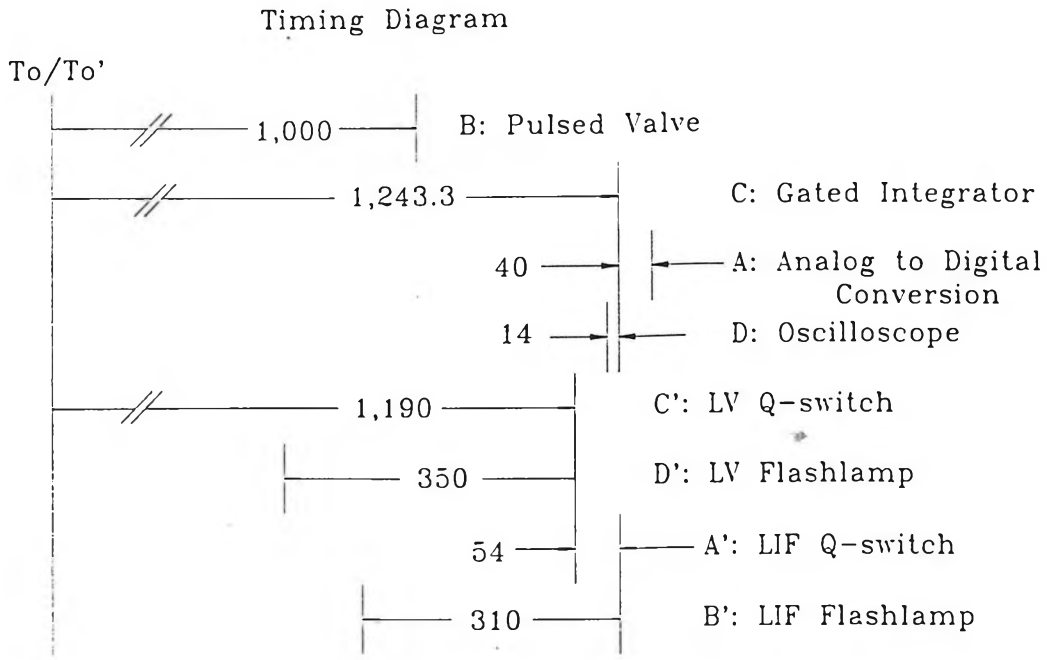

Figure 2.7 Illustration of timing delays used in triggering the experiment. T_0, A, B, C, and D are for delay generator one, and T_0', A', B', C', and D' are for delay generator two. Times are in units of μs. Laser induced fluorescence (LIF) Q-switch delay is for N2 carrier gas; He will give shorter times and Ar longer. Laser vaporization (LV) Q-switch delay is for 200 μs pulsed valve driver width.

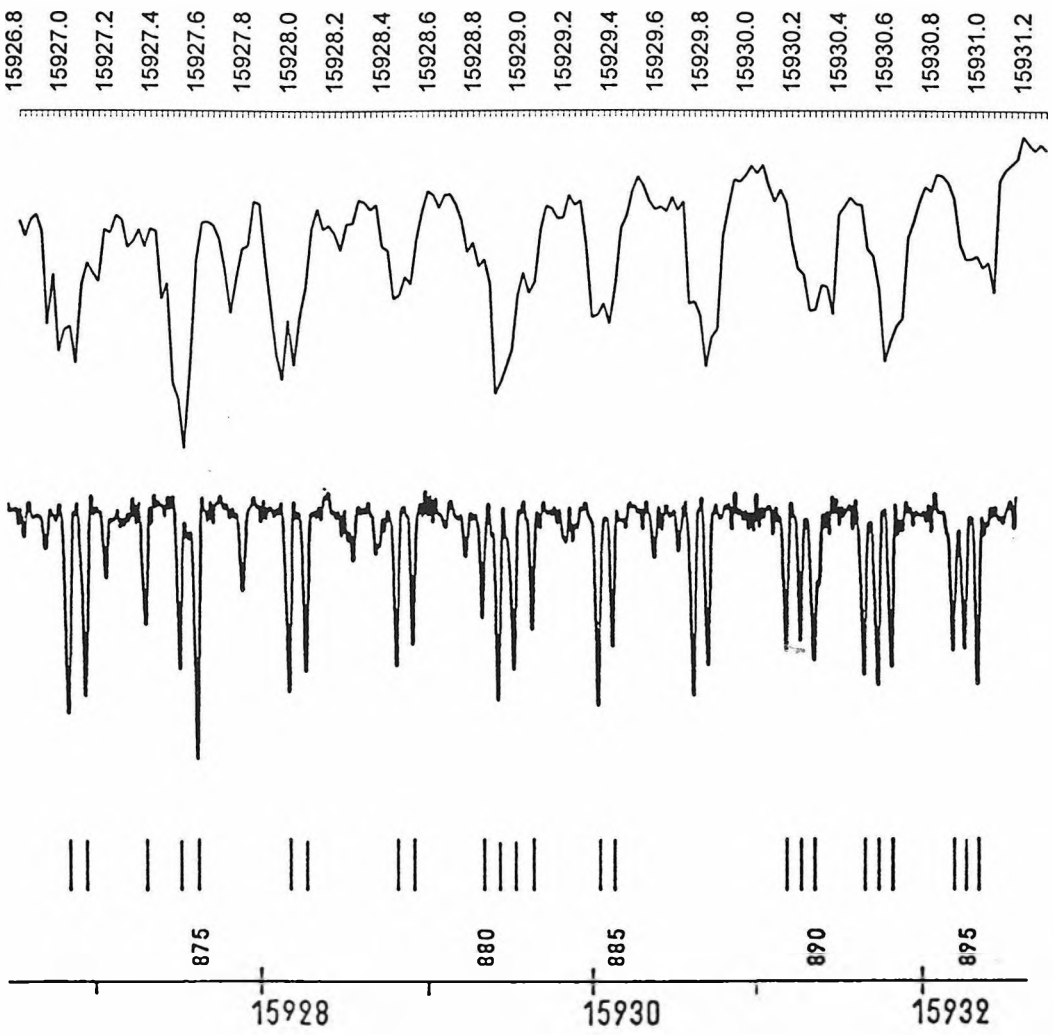

Figure 2.8 Calibration of the dye laser by comparing (a) LIF spectrum of I_2 excited by TDL-51 laser to (b), standard reference absorption spectrum of I_2.

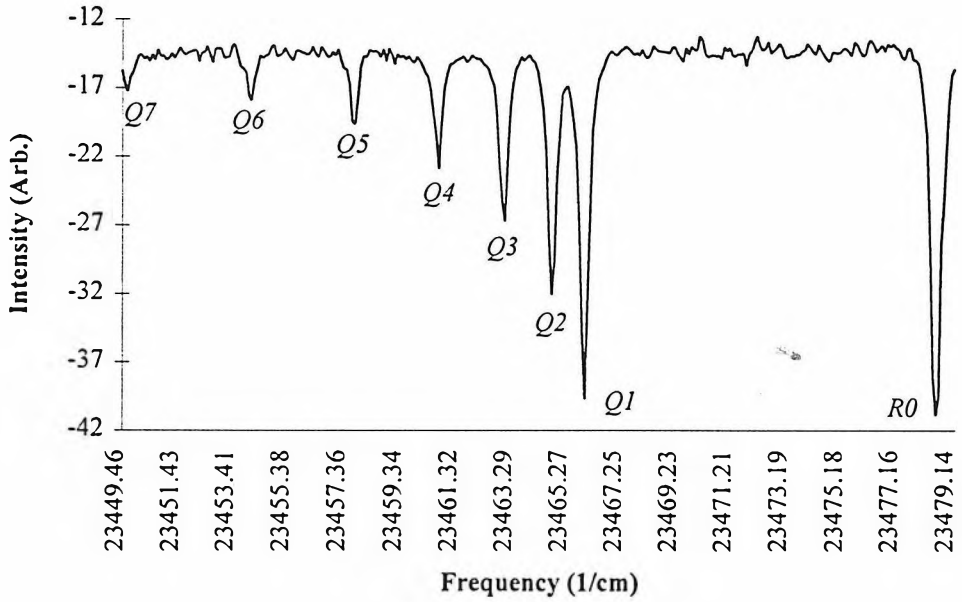

Figure 2.9 Rotationally resolved spectrum of $A \leftarrow X$ transition of AlH.

(*a*)

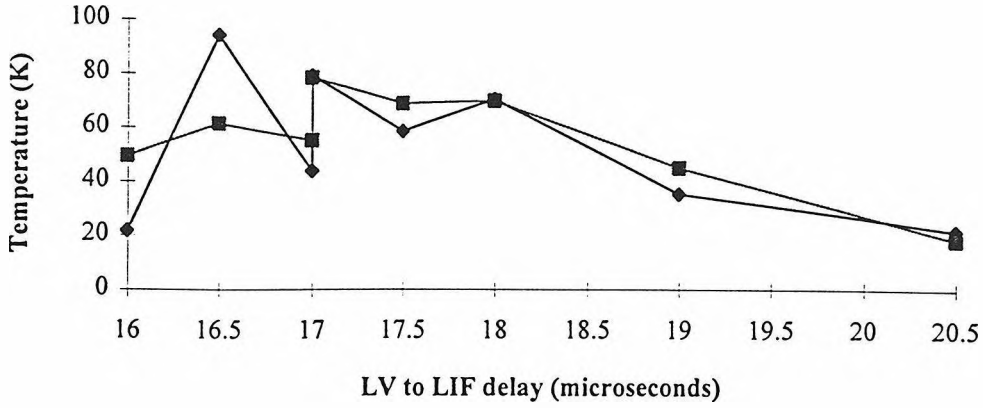

(*b*)

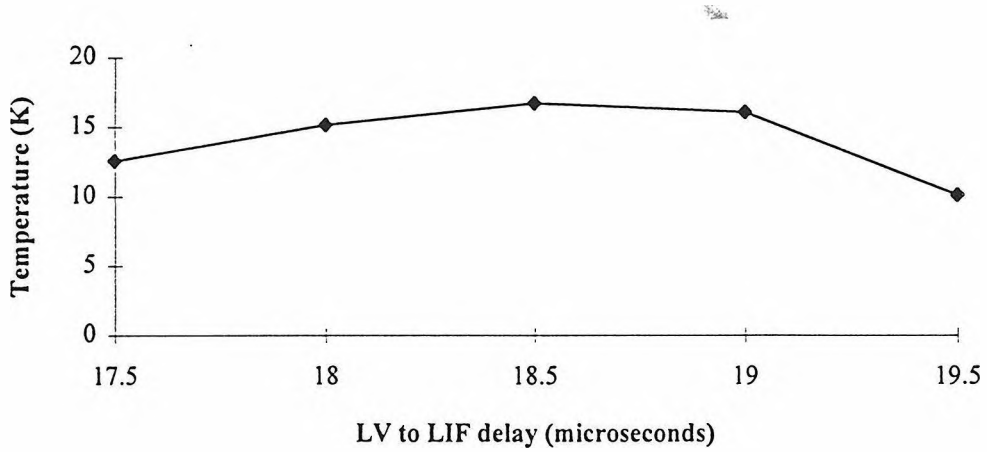

Figure 2.10 Diagrams showing the dependence of AlH rotational temperature on the delay time between vaporization and fluorescence laser triggers. (a) Low gas throughput. (b) High gas throughput.

Table 2.1. Polarizations of laser beams at various stages of frequency generation. (a) Surelite I Nd:YAG and HG-4B harmonic generation unit. (b) NY-61 Nd:YAG laser, TDL-51 dye laser, and UVX mixing and doubling system.

(a)	**Wavelength**	**Crystal**	**Power**	**Polarization**
	1.064 μm	Nd:YAG	430 mJ	Horizontal
	532 nm	KD*P Type II (o + e = e)	160 mJ	Horizontal[1]
	355 nm	KD*P Type I (o + o = e)	55 mJ	Vertical[1]
	266 nm	KD*P Type I	40 mJ	Vertical[1]

(b)	**Wavelength**	**Medium**	**Power**	**Polarization**
	1.064 μm	Nd:YAG osc. and amp	600 mJ[2]	Horizontal
	532 nm	KD*P Type I	320 mJ[2]	Vertical
	844 nm - 532 nm	Dye laser	60 mJ[3]	Vertical
	442 nm - 369 nm	Mixing/MCC2,[4]		
		position B, type II	1-5 mJ	Horizontal
	378 nm - 283 nm	Doubling/DCC2,[4]		
		position B, type I	1-5 mJ	Horizontal
	279 nm - 236 nm	Mixing after doubling:[5]		
		Doubler/DCC1&2,		
		position A, type I		
		Mixing/MCC2,		
		position B, type II	0.1-2 mJ	Horizontal

Notes:

[1] Assumes that HG-4B unit is oriented with Caltech property label on top.

[2] Seeder on. Subtract 10% for unseeded operation.

[3] For DCM dye at 640 nm. Power will vary for other dyes and wavelengths.

[4] Dye laser polarization rotation prism not used. If mixing or doubling is performed in position A instead of position B, the polarization rotation prism should be employed.

[5] Polarization rotation prism is necessary for mixing after doubling.

Table 2.2 Transitions of the aluminum atom. Dye laser frequency wavelengths are given based on mixing for the **S** ← **P** transitions and doubling for the **D** ← **P** transitions. Vacuum wavelengths were obtained from air wavelengths by the following formula: $\lambda(vac) = 0.00942 + 1.000261 * \lambda\ (air)$. Similarly, $\lambda(air) = -0.00942 + 0.999739 * \lambda(vac)$.

Transition	**λ(nm) air**	**λ(nm) laser air**	**ν(cm^{-1}) vacuum**
$4^2S_{1/2} \leftarrow 3^2P_{3/2}$	396.1520	631.2524	25235.65
$4^2S_{1/2} \leftarrow 3^2P_{1/2}$	394.4006	626.8171	25347.71
$3^2D_{3/2} \leftarrow 3^2P_{3/2}$	309.2839	618.5678	32323.33
$3^2D_{5/2} \leftarrow 3^2P_{3/2}$	309.2710	618.5420	32324.68
$3^2D_{3/2} \leftarrow 3^2P_{1/2}$	308.2153	616.4306	32435.40

Chapter 3:

The Aluminum-Water van der Waals Complex

3.1 Abstract

The first experimental results have been recorded from a novel pulsed laser ablation cluster source using an aluminum target. A system of new peaks arises from the addition of water vapor to the source carrier gas. Total laser excited fluorescence was monitored as a function of laser wavelength to obtain the spectra of species in the supersonic expansion. Three progressions were observed, with harmonic frequencies of 122.3 cm^{-1}, 117.7 cm^{-1}, and 106.6 cm^{-1}. These newly observed peaks are discussed in terms of rovibronic transitions of $Al(H_2O)$, HAlOH, and AlOH.

3.2 Introduction

Van der Waals complexes involving a neutral metal atom and a ligand are of considerable scientific interest. These systems serve as tractable models of complex bulk systems, allow direct observation of bond insertion reactions, and answer basic questions concerning solvation and surface reactivity. An investigation of the system involving the interaction of an aluminum atom with a water molecule exemplifies these issues.

A number of groups have studied the reaction of aluminum atoms with water for a variety of reasons. Aluminum grenades are used in the atmosphere in order to study winds, diffusion, temperature, and other phenomenon. Oblath and Gole assign the emission of these grenades to a chemiluminescent reaction due to a single collision of an aluminum atom with water.[1] They observed broad chemiluminescence from 16,700 cm^{-1} to 28,600 cm^{-1} and suggested that it was due to the formation of aluminum hydroxy hydride (HAlOH). Furthermore McClean *et al.* have performed additional gas phase measurements, studying the kinetics of the reaction $Al(^2P^0) + H_2O$ in a high temperature reactor.[2]

Matrix studies are unanimous in observing the insertion of aluminum atoms, generated in ovens or by laser ablation, into water molecules in a matrix host. Margrave and coworkers studied matrices resulting from the codeposition of water vapor with aluminum atoms produced in an oven.[3,4] The experiment did not reveal the perturbed ν_2 bend of H_2O and the authors concluded that no $Al(H_2O)$ adduct was formed at 15 K. Infrared absorptions due to aluminum monohydroxide (AlOH) and HAlOH were, however, observed. Through the reaction of laser-ablated Al atoms with H_2O in Ne and

Ar matrices at 4 K, Joly *et al.* were able to measure the ESR spectrum of HAlOH.[5] In similar work by Knight *et al.*, HAlOH was generated by passing water vapor over an aluminum surface that served as the target of a focused 5-10 mJ pulse of 532 nm radiation. The flow was co-condensed with the rare gas to form the matrix at 4 K.[6] In addition these workers have calculated the structure of HAlOH at the MP2/6-31G** level; the structures of *cis* and *trans* HAlOH are given in fig. 3.1.

Early theoretical work suggested that HAlOH formed from the reaction of Al with H_2O with no barrier, given an approach of the Al atom perpendicular to the OH bond.[7] In contrast to the matrix studies detailed above, and the early theoretical work, recent *ab initio* and experimental results indicate that there is a small but significant barrier towards the insertion of aluminum into the water molecule. Sakai has studied the direct insertion mechanism of Al into a number of X-H bonds (X = F, O, N, Cl, S, and P) theoretically, and has found that the mechanism involves first an electron transfer from Al into an OH σ^* orbital in H_2O.[8] In the second step the AlH bond is formed. Structures of the lowest energy geometries and transition state may be seen in fig. 3.2.

Study of these insertion reactions leads to the question of whether the Al(H_2O) adduct is stable, and if so, how large the barrier to insertion is. According to *ab initio* studies at the MP2/6-31G(d) level, the first step involves a barrier of 12 kcal/mol relative to separated Al and H_2O (21.3 kcal/mol relative to the Al(H_2O) adduct). The potential energy of the system drops by 51.8 kcal/mol for HAlOH relative to the transition state. Compared to the separated atom and molecule, the Al(H_2O) complex is bound by 9.3 kcal/mol and HAlOH is bound by 39.8 kcal/mol. The reactivity of Al with H_2O will

depend critically on the relative and internal energy available to the reactants, which in turn depends on the dynamics of the plasma generation and cooling in the supersonic expansion. The salient features of the potential energy surface are summarized in fig. 3.3.

Three groups have employed laser ablation sources similar to that employed in this work, involving laser ablation of aluminum rods in the presence of water vapor. The resonant two photon ionization spectrum of AlOH generated by such a source was measured by M. A. Duncan and coworkers.[9] In their work the Al atom and a water molecule undergo an elimination reaction to generate AlOH. Fuke and coworkers were able to prepare aluminum water clusters $Al(H_2O)_n$ for n = 1 to 10 by ablating an aluminum rod into an expansion of 10 atm of He seeded with water vapor.[10] In their study, single photon ionization and time-of-flight mass spectroscopy were used to characterize the source and study the photodissociation processes upon direct ionization of the clusters $Al^+(H_2O)_n$. *Ab initio* calculations were performed on the $Al(H_2O)_n$ and $Al^+(H_2O)_n$ clusters to aid in interpreting the spectra.[11] It is not clear whether $HAlOH(H_2O)_{n-1}$ or $Al(H_2O)_n$ was generated in their laser ablation cluster source. Finally, Cox *et al.* observed that water will chemisorb to small aluminum clusters produced by a laser vaporization beam source with no elimination.[12]

The reactions of other group 13 atoms with water molecules have been studied. Laser ablation of a boron rod and cocondensation with water vapor in an argon matrix resulted in the formation of HBO, BO, and BOB. [13] No evidence was found for the insertion product HBOH. In addition, the gas phase reaction B + H_2O has been found to

produce BO + H_2.[14] Infrared spectra of the clusters M(H_2O) (M = Ga, In, Tl) in argon matrices have also been recorded.[3] These atoms were found to form stable complexes with water, inserting into the water molecule only upon photoexcitation.

Experimentalists have also been interested in clusters involving aluminum atoms with ligands other than water. In work related to high-energy-density material, it is hoped that the weak van der Waals interactions may be exploited in order to stabilize the addition of energetic radicals into solid hydrogen matrices. Insight into the behavior of these systems will result from observation of the corresponding clusters. By doping light atoms into a solid hydrogen matrix, the specific impulse of the resulting material will make an ideal rocket fuel; H, Li, B, C, N, O, Mg, and Al show particular promise.[15] The specific impulse is proportional to the square root of the ratio of the heat of combustion to the mass of the fuel, and reflects the suitability of a given substance for use as a fuel. Currently launch costs and payload are limited by the bulk of the fuels involved. In order to better understand these fuels, a number of metal ligand systems have been studied, for example Al + H_2,[16] and Li + H_2.[17]

There is also interest in observing addition of metal atoms into covalent bonds, which has led to the study of the reactions Al + H_2 and Al + CH_4 in inert matrices[18] as well as *ab initio* calculations on the insertion of aluminum atoms into the XH bonds of HF, H_2O, NH_3, HCl, H_2S, PH_3, and CH_3OCH_3.[3]

This chapter will discuss some compelling laser-induced fluorescence results obtained due to the addition of water vapor to the laser vaporization cluster source. The observed peaks can be interpreted in terms of a number of polyatomic species involving

the reaction of water with aluminum, including AlOH, HAlOH, and $Al(H_2O)$. Further studies are needed in order to definitively assign the spectra.

3.3 Experimental

A detailed description of the apparatus has been given in chapter 2. The following section summarizes the key elements of the experiment. Aluminum atoms were created in a novel pulsed nozzle laser vaporization cluster source, and reacted with water vapor seeded into the carrier gas. Eight to ten atmospheres of carrier gas (N_2, D_2, He, Ar, or Ne) flowed past a reservoir of room temperature water (0.026 atm vapor pressure). The resulting mixture, containing ~0.25% H_2O vapor, was released by a piezoelectric pulsed valve into a short channel leading to vacuum. In the channel aluminum atoms were ablated into the trailing edge of the gas pulse by the focused output of a Nd:YAG laser (Continuum Surelite I, third harmonic 355 nm, 7-12 mJ, 19 Hz). The supersonic expansion was crossed 4.5 cm from the nozzle with the output of a frequency doubled dye laser (Rhodamine 640 dye from Exciton, Continuum TDL-51 dye laser with UVX-3/DCC-2 KD*P harmonic generator) pumped by a second Nd:YAG laser (532 nm, Continuum NY-61-20). The harmonic generation crystals provided tunable radiation in the range of 302 nm to 315 nm, at a power of ~1 mJ/pulse. Because molecular transitions are easily saturated even at low laser powers, and since noise due to scattered light is a linear function of pump power, it was found that decreased pump beam powers lead to greater signal to noise. In addition low pump powers minimize power broadening of the observed transitions. Consequently, the light was attenuated to

~100 μJ by turning the crystal away from the most efficient doubling angle. During the experiment the operator would actively adjust laser power. The power was determined by sampling a small amount of the UV output that was reflected by a pickoff optic onto a photodiode. The crystal angle was changed with a stepping motor to keep this value constant. The laser excited fluorescence from moieties in the beam was collected by a system of UV grade lenses and apertures and focused onto a PMT (R372, Hamamatsu). The signal was fed by a pre-amp (home-built, 14 dB) into a gated integrator (SRS SR 250) and transferred to a microcomputer with an A/D converter.

3.4 Results

For a van der Waals bond between an aluminum atom Al and a molecule M, the binding energy D_e is dependent on the different electronic states of the metal atom. If the excited state of the complex is more tightly and deeply bound than the ground state, the 0-0 vibronic transition will be red-shifted relative to the atomic transition, with subsequent vibronic transitions in the same Franck-Condon envelope progressing to the blue. In order to find fluorescence spectra of van der Waals complexes, it is thus prudent to search in the vicinity of the atomic transitions.

In this work we searched the region of the spectrum near the aluminum $3^2D_{(3/2,5/2)} \leftarrow 3^2P_{3/2}$ transition at 32,324 cm^{-1}(see table 2.2, chapter 2), and located peaks associated with the addition of water to the carrier gas in the source. A system consisting of three progressions was seen. The spectra are presented in figures 3.4*a* through 3.4*e*.

A summary of the source conditions and wavelength range is presented in table 3.1. The resolution of the instrument was measured to be 0.5 cm^{-1}, and the absolute peak positions are accurate to within ±1 cm^{-1}. The spectra were calibrated by recording the position of the aluminum atomic transitions by LIF. All of the observed peaks in a 500 cm^{-1} region containing the Al $D\ (3s)^2(3d)^1 \leftarrow P\ (3s)^2(3p)^1$ transition (32,327 to 32831 cm^{-1}) are presented in table 3.2. In addition, the region of the spectrum extending to 32,249 cm^{-1} was examined but no new peaks were found to arise after adding water to the laser vaporization cluster source.

Three progressions are apparent in an examination of the data presented in fig. 3.4 and summarized in table 3.2. The first is a series of four peaks, *a.2, b.2, d.1,* and *e.2.* Since there are no peaks appearing to the red which are dependent on the addition of water to the source, the *a.2* peak is assigned as the origin of the vibronic series. The spacings between the peaks are 120.0, 118.4, and 116.8 cm^{-1} respectively. The best fit to this data results in ω_e = 122.3 cm^{-1} and $\omega_e x_e$ = 0.9 cm^{-1}, with T_e = 32,341.5 cm^{-1}. The peaks in this series all have similar linewidths as shown in table 3.2.

The second series consists of three peaks, *b.4, d.3,* and *e.3.* The peaks are spaced by 114.9 cm^{-1} and 112.4 cm^{-1} respectively, leading to spectroscopic constants of ω_e = 117.7 cm^{-1}, $\omega_e x_e$ = 1.3 cm^{-1} (ω_e = 113.9 cm^{-1} if anharmonicity is ignored), and T_e = 32,474.4 cm^{-1}.

Finally there are two wide peaks, *d.2* and *e.1,* seen at 32,586.6 cm^{-1} and 32,693.2 cm^{-1} respectively. Each of these peaks is shaded to the blue and exhibit a linewidth that

is over twice as wide (3.2 and 3.0 cm^{-1}) as any other peak in the spectra. The width would suggest a common origin. The spacing between these peaks is 106.6 cm^{-1}.

Arguments concerning whether these peaks are due to fluorescence from AlOH, HAlOH, or $Al(H_2O)$ are presented in the discussion below. The three series of peaks are represented schematically in fig. 3.5.

An attempt was made to observe $Al(H_2)$ and $Al(D_2)$ with the laser vaporization cluster source. A series of peaks attributable to Rydberg transitions in the diatomics was observed, but no series due to the Al complex were found. No definitive peaks were seen in attempts to observe AlNe and $Al(N_2)$.

3.5 Discussion

Initially there are a number of candidates which would explain the system of observed peaks. Since it is known from LIF that the source produces Al atoms, and through the study of AlAr that the atoms form van der Waals complexes in the supersonic expansion (and from AlH that the beam is quite cold), it is reasonable that a cluster such as $Al(H_2O)$ could be formed. However, the issues of reactivity of translationally or even electronically hot Al with H_2O, fragmentation of H_2O in the plasma, and the formation of oxides and hydrides need to be addressed. The AlOH and HAlOH species will also be discussed in the context of assigning the observed peaks.

A number of reactions are possible in the laser vaporization cluster source:

$$Al(3^2P_{1/2}) + H_2O \rightarrow Al(H_2O) \qquad \Delta H_{rxn} = -9.3 \text{ kcal/mol}^3 \qquad (1)$$

$$\rightarrow HAlOH \qquad \Delta H_{rxn} = -39.8 \text{ kcal/mol}^3 \qquad (2)$$

$\rightarrow$ AlOH + H ΔH_{rxn} = -12 kcal/mol[19] (3)

$\rightarrow$ AlO + H_2 ΔH_{rxn} = -5 kcal/mol[19] (4)

Al + Al + M $\rightarrow$ Al_2 + M ΔH_{rxn} = -36 kcal/mol[20] (5)

Al + Ar + M $\rightarrow$ AlAr + M ΔH_{rxn} = -0.35 kcal/mol[21] (6)

A discussion concerning the assignment of the observed peaks in terms of these reaction products will be presented in the following section.

3.5.1 Diatomic Species

A number of the peaks which were observed in this experiment can be accounted for by laser excited fluorescence of AlAr. This spectrum has been measured by the method of resonant two-photon ionization and mass spectroscopic detection by M. D. Morse and coworkers.[21] Peaks due to transitions of the AlAr complex have been indicated in table 3.2. When the experiment described in section 3.3 was run with pure argon carrier gas, a series of peaks matching those of Morse were observed. The peaks are assigned to transitions from the $^2\Pi_{1/2}(3p)$ ($v'' = 0$) to the $^2\Delta(3d)$, $^2\Pi(4p)$, $^2\Pi(3d)$, and $^2\Sigma^+(3d)$ states as shown in fig. 3.7 (v' as indicated in figure). Because of the observation of these peaks it was easy to distinguish which peaks were due to AlAr, and which new peaks arose with the addition of water vapor.

The method of resonant two-photon ionization was also applied by Morse and coworkers to the diatomic Al_2.[22] Two systems of bands were found in the pertinent region of the spectrum. The *F'-X* and *F-X* systems consist of a series of red-shaded triplets (ΔE_{so} = 30 cm^{-1}) due to spin orbit splitting of atomic aluminum. This pattern is

clearly not consistent with the observed data, nor is the dependence of the peaks on the presence of water vapor in the system.

The spectroscopy of the diatomics AlH, AlO, and OH is well known.[20] Constants for these molecules are presented in table 3.3. Chemiluminescence from AlH($A\ ^1\Pi$) and AlO ($B\ ^2\Sigma^+$) are observed from the ablation of an aluminum target in the presence of 1.0 Torr of static, ambient water vapor.[23] In the case of AlH, the rotational constant of the excited electronic states is 6 cm^{-1}. The absence of rotational bands with spacings of 12 cm^{-1} excludes this molecule as the source of the spectra observed in this work. (A portion of the AlH LIF spectrum was reported in chapter 2.) In the case of AlO, the location of the electronic states would not lead to absorptions in the necessary region of the spectrum.[20] Finally, while the T_e value of the $A \leftarrow X$ transition of OH (32,684.1 cm^{-1}) makes it a good candidate for observation, evidence for the known rotational constant of 17.36 cm^{-1} has not been observed.

3.5.2 AlOH

The molecules HAlO and AlOH can be formed by the insertion of aluminum into the water molecule followed by dissociation. The isomer HAlO has been calculated to be 50 kcal/mol less stable than AlOH.[24] The $A \leftarrow X$ transition of AlOH was first observed by the codeposition of Al vapor and water in a krypton matrix. In this experiment the AlO-H stretch was observed at 3790 cm^{-1}, and the Al-OH stretch at 810 cm^{-1}. Although the bending vibration was not observed in AlOH, the bending modes of GaOH and InOH were observed at 424 cm^{-1} and 422 cm^{-1} respectively.[3,4,25] The resonant two photon

ionization spectrum of AlOH was measured by M. A. Duncan and coworkers[9] who employed a pulsed laser vaporization cluster source similar to that used in the present study. An extended progression in the Al-OH stretching and Al-O-H bending vibrational modes was observed, with a band origin at 40,073 cm^{-1}. The harmonic frequencies of the Al-OH stretch, AlOH bend, and AlO-H stretch are 895 cm^{-1}, 155 cm^{-1}, and 4313 cm^{-1} respectively in the X state and 825.1 cm^{-1}, 654.2 cm^{-1} and 3258.4 cm^{-1} respectively in the A state. It should be noted that although the upper state is predicted to be less strongly bound than the ground state, the vibrational frequency of the stretching mode only shifts from 895 cm^{-1} to 825.5 cm^{-1}. In addition, *ab initio* calculations by H. F. Schaeffer and coworkers[26] have determined harmonic vibrational frequencies of 4017 cm^{-1}, 845 cm^{-1}, and 155 cm^{-1} for the OH stretching, AlO stretching, and the bending motions (the bending frequency of HAlO is 440 cm^{-1}).

It is possible that the peaks described in this work are due to an electronic state which was not observed by Duncan and coworkers, since they only report scanning in the higher wavelength region. The bending mode experiences significant stiffening in going from the ground to the A state. The hypothetical state in AlOH will be termed A' to distinguish it from the observed A state. The A' state would have to entail a bending mode which is significantly more floppy than both Duncan's A state (654.2 cm^{-1}) and the ground state (155 cm^{-1}).

3.5.3 HAlOH

The insertion product HAlOH was observed in cryogenic matrices by Margrave *et al.* from the cocondensation of Al with water. An absorption due to the Al-H stretch was observed at 1743 cm^{-1}, in addition to an absorption due to the in-plane hydrogen bending mode at 605 cm^{-1}, the Al-OH mode at 818 cm^{-1}, and O-H stretch at 3743 cm^{-1}.[3] The SCF normal mode frequencies of this species have been determined by Sakai and Jordan using a 6-31G* basis set.[27] The authors determined scaled frequencies of 3679 cm^{-1}, 1694 cm^{-1}, 782 cm^{-1}, 674 cm^{-1}, 511 cm^{-1}, and 447 cm^{-1} for the *cis* isomer, and 3701 (3743) cm^{-1}, 1722 (1743) cm^{-1}, 776 (818) cm^{-1}, 674 (615) cm^{-1}, 544 cm^{-1}, and 432 cm^{-1} for the *trans* isomer. (The corresponding experimental frequencies due to Margrave and coworkers are given in parenthesis.) They found the *trans* isomer to be 1.1 kcal/mol lower in energy than the *cis*, with a 3.2 kcal/mol isomerization barrier. While none of these frequencies is low enough to account for the observed system of peaks, it is possible that in the excited electronic state the frequency of one or more of the vibrational modes would be reduced. This would result in a progression in the bending mode at a frequency of ~115 cm^{-1}. *Ab initio* calculations on the excited state vibrational frequencies would answer the question of whether this would be possible, and scans to higher energy may reveal bands resulting from simultaneous excitation of two or more vibrational modes.

3.5.4 Al(H_2O)

The synthesis of Al(H_2O) in the supersonic cluster source will rely on the barrier to insertion of Al into H_2O outlined in fig. 3.3.

The ground state of $Al(H_2O)$ has been calculated to correspond to $3p(\pi)$ in the atomic aluminum limit.[11] For C_{2v} $Al(H_2O)$ (see fig. 3.2), this means that the $3p$ orbital is out of the plane of the complex which has B symmetry. As calculated by Sakai, the C_{2v} and C_s complexes are only separated by ~1 kcal/mol. Since these geometries are so close in energy, it is probable that the complex has a floppy Al-OH_2 bending mode. In the excited state, the Al atom has an orbital occupation of $(3s)^2(3d)$. In C_{2v} symmetry there will be three states corresponding to m_l = 0, ±1, and ±2 or $3d(\sigma)$, $3d(\pi)$, and $3d(\delta)$ respectively. The $3d(\pi)$ and $3d(\delta)$ levels are split into B_1 and B_2 levels in the C_{2v} complex. For the ground $3p(\pi)$ state Λ = 1, and so three excitations are possible corresponding to $\Delta\Lambda$ = -1, 0, and +1 for the $3d(\sigma)$, $3d(\pi)$, and $3d(\delta)$ levels respectively. Energy levels of the Al atom and their correlation to likely states of the $Al(H_2O)$ complex are given in fig. 3.6.

Transitions with $\Delta\Lambda = \pm 1$ are perpendicular which means that the $3d(\sigma)$ and $3d(\delta)$ bands will exhibit a selection rule of $\Delta K_a = \pm 1$. Since nuclear spin states are not cooled in a supersonic expansion, *ortho* and *para* states of $Al(H_2O)$ will exist in a 3:1 ratio, corresponding to K = 0 and 1. Using the optimized geometry of S. Sakai, the rotational constants of $Al(H_2O)$ were determined to be A = 12.1 cm^{-1}, B = 0.298 cm^{-1} and C = 0.292 cm^{-1}, making the molecule a near prolate asymmetric top.[28] Therefore, a series of rovibronic peaks would be seen with a spacing of ~24 cm^{-1}. In the case of the $3d(\pi)$ transition, $\Delta K_a = 0$. For this transition the only splitting will be due to the difference in the splitting of the *ortho* and *para* nuclear spin states in the ground and excited electronic

states, that is, due to the difference between A' and A''. Figure 3.8 illustrates the symmetry of the states and transitions of $Al(H_2O)$.

The discussion of a similar complex will help to illustrate the effect of nuclear spin statistics on the rovibronic spectrum. In their study of $Hg(H_2O)$, Duval and Soep saw a series of bands due to parallel transitions of a rigid prolate symmetric top with hydrogen nuclear spin statistics in C_{2v} symmetry, and with a reduction of the A rotational constant in the excited state.[29] The change in geometry was caused by the $^3P_1 \leftarrow {}^1S_0$ atomic transition of the mercury atom. In the case of ground state $(6s)^2$ mercury the water molecule underwent virtually unhindered internal rotation. In the $(6s)^1(6p)^1$ excited state the binding energy increases from 300 cm^{-1} to 2750 cm^{-1}, and the complex assumes a rigid C_{2v} geometry. A series of doublets in the ratio of 3:1 are seen due to *ortho* and *para* states in the complex. (Peaks in the ratio of 1:2 are seen when D_2O was substituted for H_2O.) Spectroscopic constants for the X state are $\omega_e = 40$ cm^{-1}, $\omega_e x_e = 1$ cm^{-1}, $D_o = 300 \pm 30$ cm^{-1}, $B_e = 0.080$ cm^{-1} and $R_e = 3.57$ Å, while those for the A state are $\omega_e = 173 \pm 5$ cm^{-1}, $\omega_e x_e = 2.40 \pm 0.2$ cm^{-1}, $D_o = 2750 \pm 200$ cm^{-1}, $B_e = 0.176 \pm 0.004$ cm^{-1} and $R_e = 2.4 \pm 0.05$ Å. The dramatic change in the binding energy and geometry of the complex is due to the difference between the *6s* and *6p* states. In the case of $Al(H_2O)$ the $(3s)^2(3d(\pi)) \leftarrow (3s)^2(3p(\pi))$ transition may not induce as large of a structural change in that complex as the $(6s)^1(6p)^1 \leftarrow (6s)^2$ transition does in $Hg(H_2O)$. In this way the splitting seen in the parallel band for the mercury complex may not be present in the aluminum complex; the $\Delta K = 0$ transitions for $K = 0$ and $K = 1$ would overlap if $A' \approx A''$.

Modeling of the width of the rotational envelope of AlAr indicates that because of the narrow observed fluorescence linewidth the complex must be at a temperature of less than 5 K. At this temperature $Al(H_2O)$ would be expected to have a similarly small but slightly larger rotational envelope. To within the error of the measurement this is the case (see table 3.2).

As detailed in section 3.4, three series of peaks were observed. One interpretation of this data is that one of the series is due to the parallel transition $(3s)^2(3d(\pi)) \leftarrow (3s)^2(3p(\pi))$ in $Al(H_2O)$ with little geometrical change upon excitation. In this way the *ortho* and *para* transitions will be stacked on top of each other. The other two series could be due to the perpendicular transitions $(3s)^2(3d(\sigma)) \leftarrow (3s)^2(3p(\pi))$, and $(3s)^2(3d(\delta)) \leftarrow (3s)^2(3p(\pi))$. In this case the smaller peak in the expected doublet (spaced by *2A* and with an intensity ratio of 3:1) has not been observed; whether this is due to a problem in signal to noise or because the assignment is in error is an open question. Methods of addressing the question of the assignment of these peaks are presented in the following section.

3.6 Future Work

Assignments have been proposed for the observed peaks in terms of the AlOH, HAlOH, and $Al(H_2O)$ moieties. A number of experiments are possible which would allow the definitive assignment of these initial experimental results from the laser vaporization cluster spectroscopy apparatus. The peaks were observed in the region from 32,327 cm^{-1} to 32,831 cm^{-1}, and the region extending to 32,249 cm^{-1} has been

investigated. Further scans to the blue of 32,831 cm^{-1} would reveal combination bands. Depending on the frequency of the absorptions, assignment could be made to $Al(H_2O)$ in the case of high frequency perturbed water vibrations, or to AlOH or HAlOH if lower frequency modes are seen. To the best of our knowledge there are no *ab initio* studies of the ground state vibrational frequencies of $Al(H_2O)$. In addition to this information it would be extremely useful to perform calculations to determine the position and vibrational frequencies of the excited states of $Al(H_2O)$ and HAlOH. Further scans could also be conducted in the region of the Al $4s \leftarrow 3p$ transition. Features in the region of this transition may reveal evidence of a stable $Al(H_2O)$ complex.

Another option would be to substitute D_2O for H_2O and repeat the experiment. The substitution would lead to a change of the vibrational frequency of $Al(H_2O)$ from 122 cm^{-1} to 118 cm^{-1}, which would be immediately evident in the spectrum presented here. This substitution would lead to a change in the rotational constants of the complex to A = 6.15 cm^{-1}, B = 0.267 cm^{-1}, and C = 0.258 cm^{-1}. In the case of AlOD or DAlOD, the observed frequency of modes involving the substitution would also be affected.

One unresolved issue is the temperature in the source and the extent of reactivity of Al with water under these conditions. Since it is known that Al will react with H_2O in matrices at temperatures of 4 to 15 K, it is perhaps too optimistic to expect that the first interaction of Al with H_2O will take place in such a frigid environment (temperatures in laser ablation sources may reach 10,000 K before the expansion). A pickup source where aluminum atoms have first been thermalized and subsequently cooled in the beam before they interact with water vapor could prevent hot Al atoms from inserting into H_2O.

A time-of-flight mass spectrometer is currently being designed in order to allow resonance-enhanced multi-photon ionization spectroscopy of clusters. This modification will allow unambiguous assignment of spectra as arising from a specific cluster mass.

3.7 Conclusion

Studies with a new laser vaporization cluster source using laser induced fluorescence detection have yielded a promising series of peaks which arise from the presence of water in the gas pulse. Further studies are necessary to determine if these peaks are due to AlOH, HAlOH, $Al(H_2O)$ or another species.

3.7 References

[1] S. B. Oblath and J. L. Gole, *J. Chem. Phys.* **70**(1), 581 (1979).

[2] R. E. McClean, H. H. Nelson, and M. L. Campbell, *J. Phys. Chem.* **97**, 9673 (1993).

[3] R. H. Hauge, J. W. Kauffman, and J. L. Margrave, *J. Am. Chem. Soc.* **102**(19), 6005 (1980).

[4] M. A. Douglas, R. H. Hauge, and J. L. Margrave, ACS Symposium Series 179, 347, ACS Washington D. C. (1982).

[5] H. A. Joly, J. A. Howard, M. Tomietto, and J. S. Tse, *J. Chem. Soc. Faraday. Trans.* **90**(20), 3145 (1994).

[6] L. B. Knight, Jr., B. Gregory, J. Cleveland, and C. A. Arrington, *Chem. Phys. Lett.* **204**(1,2), 168 (1993).

[7] H. A. Kurtz and K. D. Jordan, *J. Am. Chem. Soc.* **102**(3), 1177 (1980).

[8] S. Sakai, *J. Phys. Chem.* **96**(21), 8369 (1992). S. Sakai, *J. Phys. Chem.* **97**(35), 8917 (1993).

[9] J. S. Pilgrim, D. L. Robbins and M. A. Duncan, *Chem. Phys. Lett.* **202**(3,4), 203 (1993).

[10] F. Misaizu, K. Tsukamoto, M. Sanekata, and K. Fuke, *Suppl. Z. Phys. D.* **26**(S), 177 (1993).

[11] H. Watanabe, M. Aoki, and S. Iwata, *Bull. Chem. Soc. Jpn.* **66**, 3245 (1993).

[12] D. M. Cox, D. J. Trevor, R. L. Whetten, and A. Kaldor, *J. Phys. Chem.* **92**, 421 (1988).

[13] L. Andrews and T. R. Burkholder, *J. Phys. Chem.* **95**(22), 8554 (1991).

[14] J. L. Gole and S. A. Pace, *J. Phys. Chem.* **85**, 2651 (1981). S. Sakai and K. D. Jordan, *J. Phys. Chem.* **87**(13), 2293 (1983).

[15] M. E. Fajardo, S. Tam, T. L. Thompson, and M. E. Cordonnier, *Chem. Phys.* **189**, 351 (1994).

[16] G. V. Chertihin and L. Andrews, *J. Phys. Chem.* **97**(40), 10295 (1993).

[17] D. D. Konowalow, Proceedings of 1993 HEDM meeting.

[18] J. M. Parnis and G. A. Ozin, *J. Phys. Chem.* **93**(4), 1204 (1989). J. M. Parnis and G. A. Ozin, *J. Phys. Chem.* **93**(4), 1215 (1989). J. M. Parnis and G. A. Ozin, *J. Phys. Chem.* **93**(4), 1220 (1989).

[19] M. W. Chase, Jr., C. A. Davies, J. R. Downey, Jr., D. J. Frurip, R. A. McDonald, and A. N. Syverud, Eds., *J. Phys. Chem. Ref. Data* **14** (Suppl. 1) (1985).

[20] K. P. Huber and G. Herzberg, *Molecular Spectra and Molecular Structure IV. Constants of Diatomic Molecules*, Van Nostrand Reinhold, New York (1979).

[21] S. A. Heidecke, Z. Fu, J. R. Colt and M. D. Morse, *J. Chem. Phys.* **97**(3), 1692 (1992).

[22] Z. Fu, G. W. Lemire, G. A. Bishea and M. D. Morse, *J. Chem. Phys.* **93**(12), 8420 (1990).

[23] E. Ishitani, S. Yoshimoto, H. Higashide, M. Kobayashi, H. Shinohara, and H. Sato, *Chem. Lett.*, 1203 (1993).

[24] G. Vacek, B. J. DeLeeuw, and H. F. Schaeffer III, *J. Chem. Phys.* **98**(11), 8704 (1993).

[25] S. E. Gransden, J. W. Kauffman, P. Meier, R. H. Hauge, and J. L. Margrave, "Matrix Isolation Studies of Metal Atom Reactions with Water, II: Magnesium, Aluminum, and Iron," *Proc. NBS Mater. Res. Symp.* (1978).

[26] Y. Yamaguchi, B. J. DeLeeuw, G. Vacek, C. A. Richards, and H. F. Schaeffer III, *J. Chem. Phys.* **101** (4), 3006 (1994).

[27] S. Sakai and K. D. Jordan, *Chem. Phys. Lett.* **130**(1,2), 103 (1986).

[28] The program Momint, written by M. Okumura, was used for this calculation.

[29] M. C. Duval and B. Soep, *J. Phys. Chem.* **95**, 9075 (1991).

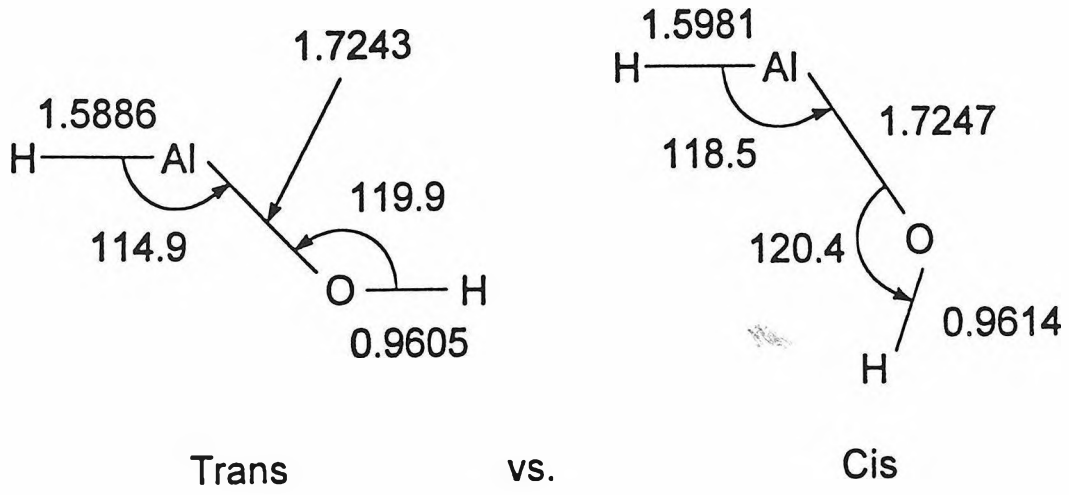

Figure 3.1 *Ab initio* calculation of the structure of the *cis* and *trans* isomers of HAlOH at the MP2/6-31G** level by Knight *et al.* (1993). The *trans* isomer is more stable by ~1 kcal/mol.

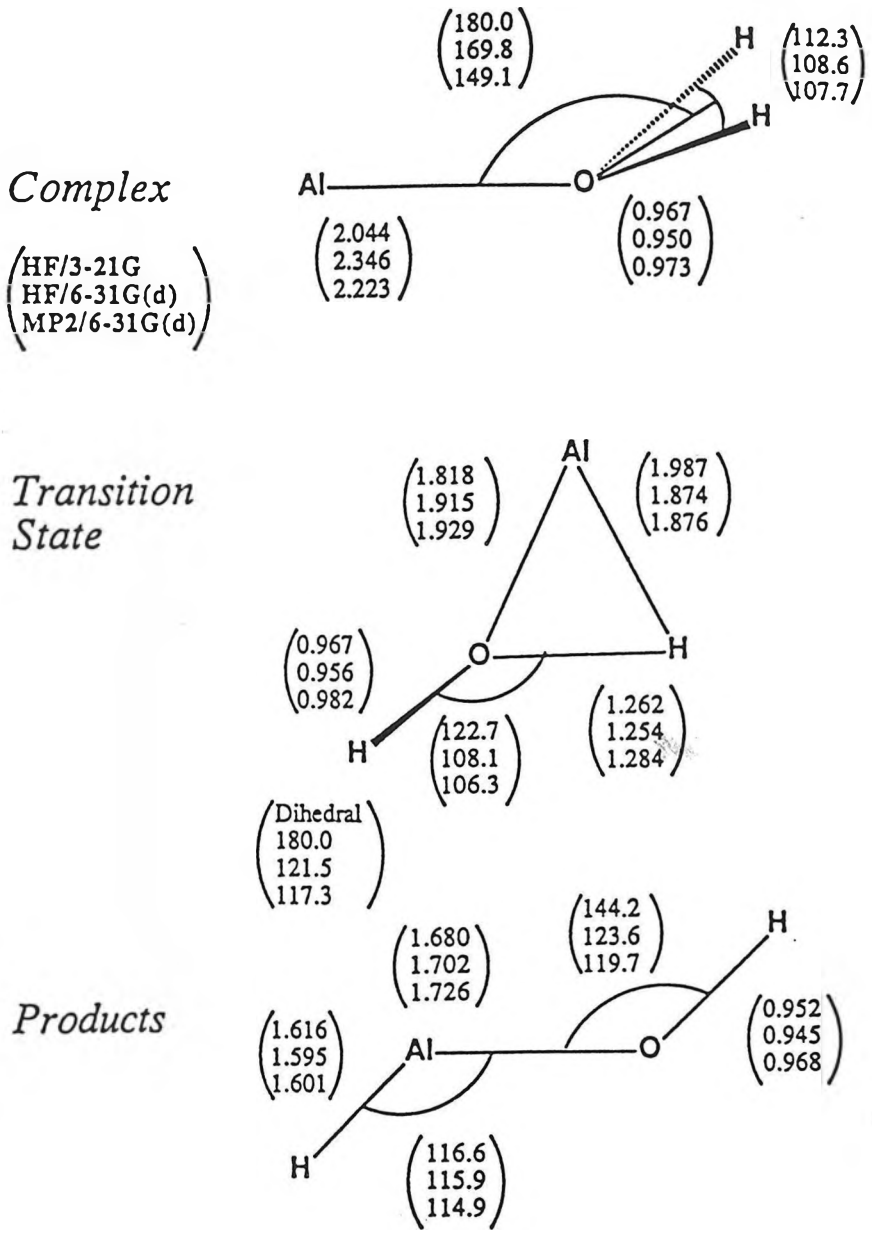

Figure 3.2 Geometry of the stationary points of the Al + H_2O reaction. The upper, middle and lower values were calculated at the HF/3-21G, HF/6-31G(d), and MP2/6-31G(d) levels respectively. Bond lengths are in Ångstroms, and angles are in degrees. The angles Φ are dihedral angles. Calculations are due to S. Sakai (1993).

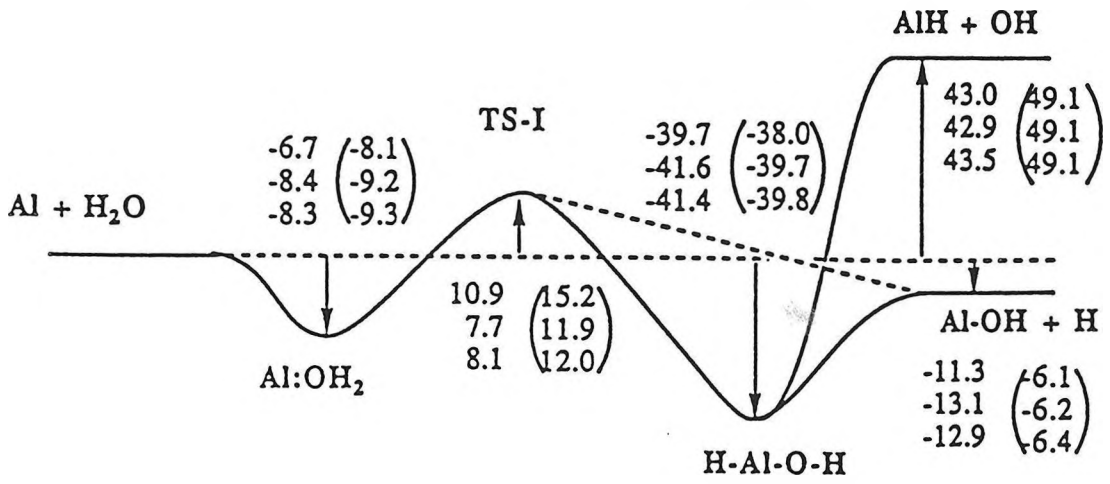

Figure 3.3 Potential energy surface for the Al + H_2O reaction. Values in parenthesis do not include corrections for zero point vibrational energies. From top to bottom, the calculations were performed with the HF/3-21G, HF/6-31G(d), and MP2/6-31G(d) geometries (S. Sakai (1993)).

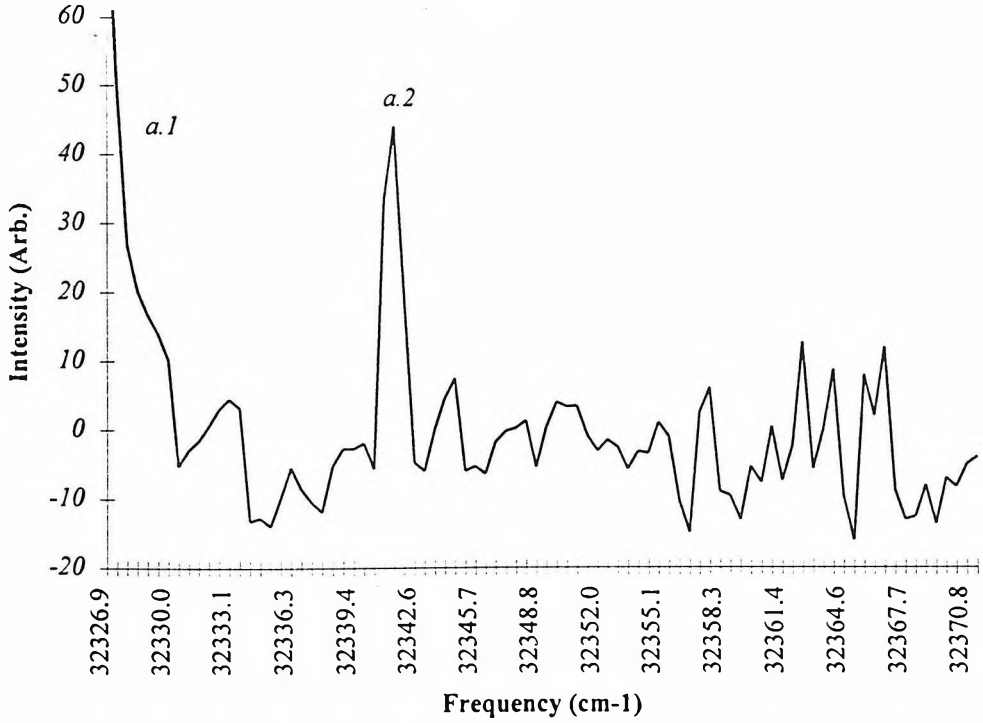

Figure 3.4*a*: 1300 shots/point.

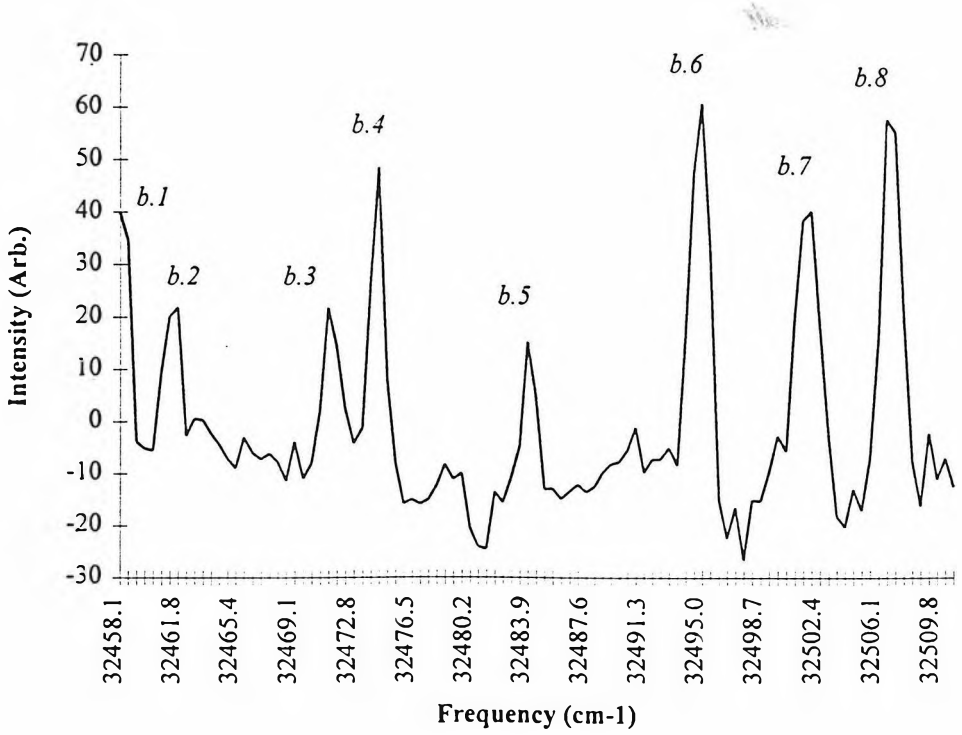

Figure 3.4*b*: 3000 shots/point.

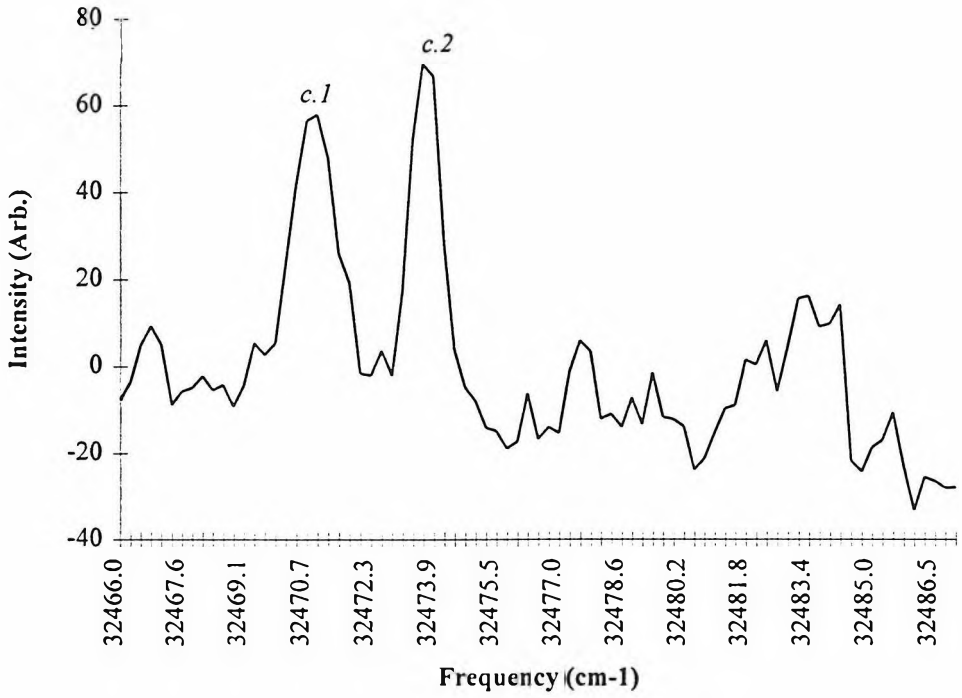

Figure 3.4*c*: 1000 shots/point.

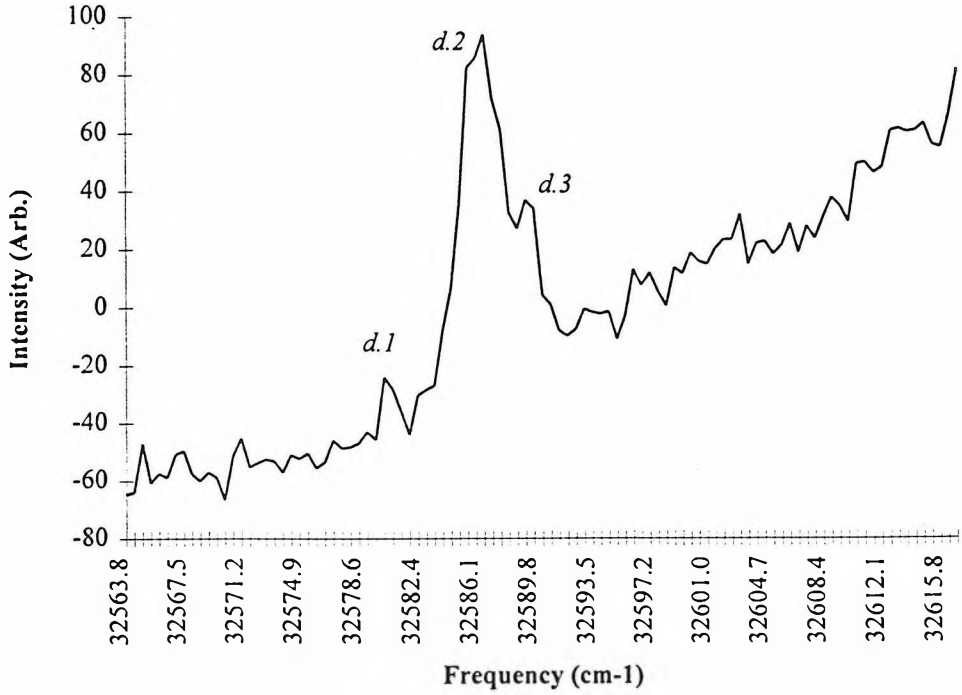

Figure 3.4*d*: 1700 shots/point.

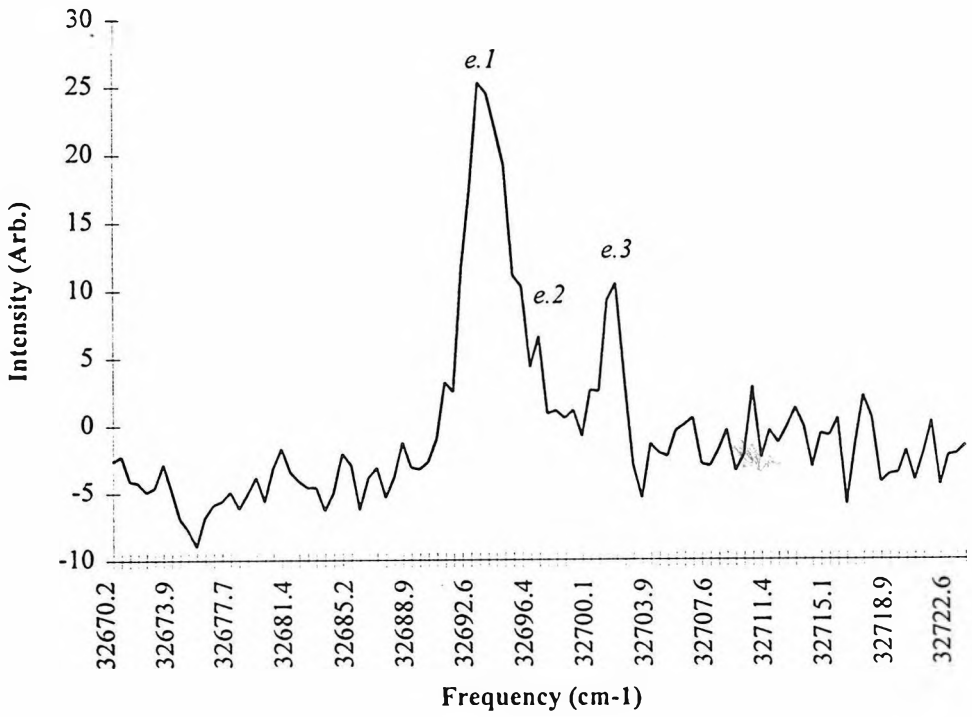

Figure 3.4*e*: 1600 shots/point.

Figure 3.4: Laser-Induced fluorescence spectra measured using the laser vaporization cluster source. The data files and source gas conditions used in compiling the data are given in Table 3.1.

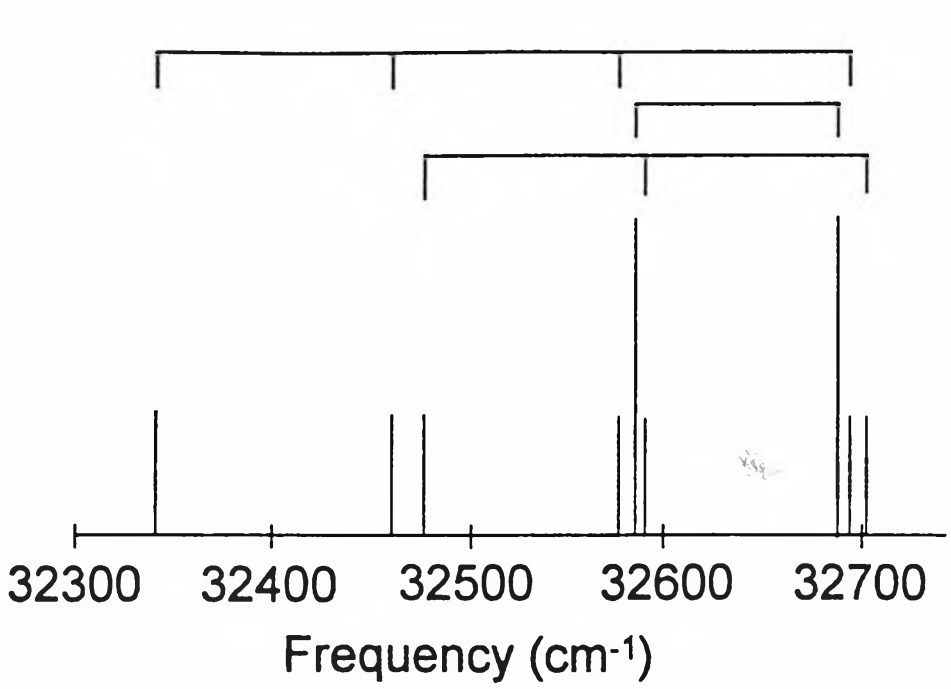

Figure 3.5 Drawing showing the position of the peaks in the three series.

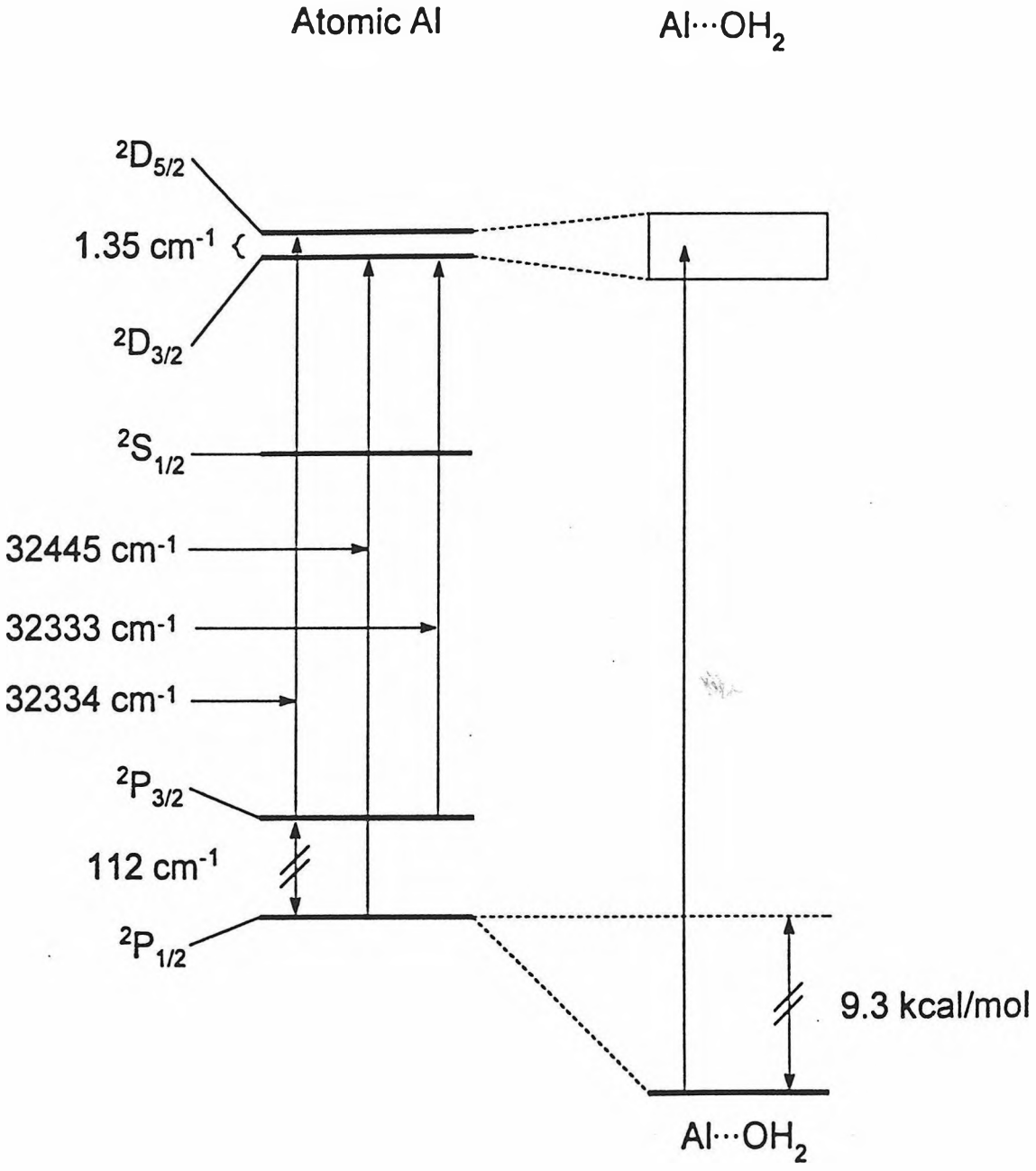

Figure 3.6 Illustration of the relation between the $Al(H_2O)$ vibronic bands and the Al atomic transitions.

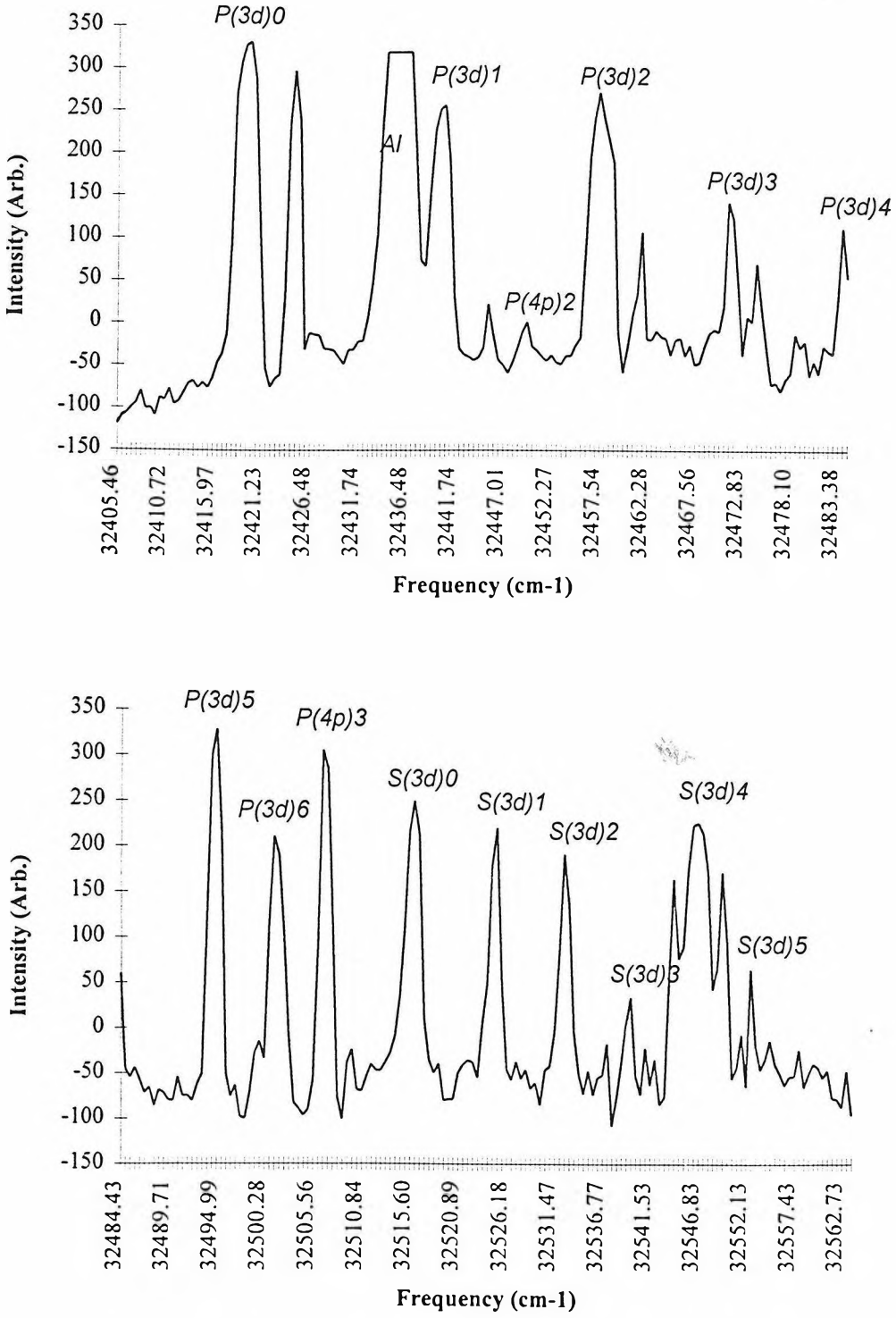

Figure 3.7 Spectra of AlAr observed by LIF of the molecular beam emitted by the laser vaporization cluster source. Peak labeling may be understood by the following examples. *P(3D)5* represents the transition $^2\Pi(3d)$ (v' = 5) ← $^2\Pi_{1/2}(3p)$ (v'' = 0), while *S(3d)4* represents the transition $^2\Sigma^+(3d)(v' = 4) \leftarrow {}^2\Pi_{1/2}(3p)$ (v'' = 0).

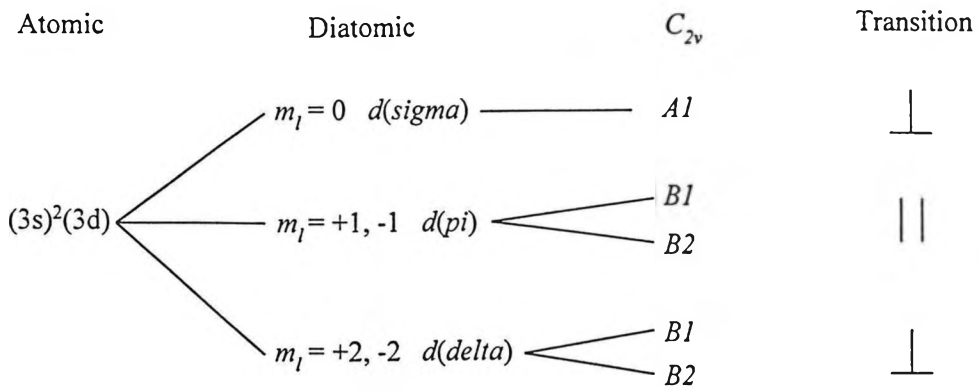

Figure 3.8 Illustration of the orbital symmetry of the different geometries of the Al(H_2O) complex, and the different transitions (perpendicular or parallel) which these electronic states will result from.

Table 3.1: Experimental conditions for the spectra presented in Fig. 3.4 *a* to *e*. An asterisk (*) means that the data files were used in compiling the spectra in Fig. 3.4.

	Frequency Range (cm^{-1})	Files, notebook page, source gas		Largest Peak(s)
a	32326.9 - 32371.4	5403R(22..27), 28	Ar	Not seen
		5406R(16..20), 45	Ar/H_2O	Not seen
		5413R(32..36), 69	*Ar/H_2O	Small, two
		5511N(4..6), 132	N_2	Not seen
		5511D(15..18), 136	D_2	Small
		5515W(27..29), 156	*Ar/H_2O	Two
		5516W(2..6), 157	*Ar/H_2O	Strong

	Frequency Range (cm^{-1})	Files, notebook page, source gas		Largest Peak(s)
b	32458.1 - 32510.8	5218R(7,9), 296	Ar	Not seen
		5402R(11..15), 22	Ar	Not seen
		5406R(32..36), 48	*Ar/H_2O	Strong
		5412R(7..16), 60	*Ar/H_2O	Strong
		5425E(7..11), 79	He/H_2O	Medium
		5425E(15..19), 84	He/H_2O	Small
		5426N(3..12), 85	*N_2/H_2O	Sharp
		5427N(5..9), 90	N_2	Not seen
		5428L(1..5), 94	Ne/H_2O	Weak
		5428H(1..10), 97	*H_2/H_2O	Medium
		5428H(21..25), 97	*H_2/H_2O	Medium
		5429R(23..30), 107	*Ar	Medium
		5505W(17..19), 124	Ar/H_2O	Weak
		5510N(4..8), 131	N_2	Weak
		5511D(2..4), 137	D_2	Weak
c	32466.0 - 32487.1	5513W(2..9), 142	*Ar/H_2O	Medium
		5513W(24,25), 145	*Ar/H_2O	Medium
d	32563.8 - 32616.9	5403R(45..49), 31	*Ar	Strong, two
		5404R(1..5), 31	*Ar	Baseline
		5413R(1..5), 63	Ar/H_2O	Weak
		5426N(28..32), 87	N_2/H_2O	Not seen
		5430R(21..24), 109	*Ar	Two
		5505W(23,24), 125	*Ar/H_2O	Two
		5506W(1..3), 125	*Ar/H_2O	Two
		5515W(9..11), 150	Ar/H_2O	Weak, low gas load
		5515W(6..8), 150	*Ar/H_2O	Strong, two
e	32670.2 - 32723.7	5404R(16..20), 37	*Ar/H_2O	First of two
		5404R(21..25), 38	*Ar/H_2O	Second of two
		5414R(6..15), 73	Ar/H_2O	Weak
		5430R(35..42), 111	*Ar	Small, two
		5506W(7..9), 125	*Ar/H_2O	Two, good S/N
		5515W(15..23), 153	*Ar/H_2O	Medium

Table 3.2: Peak positions and linewidths for labeled peaks of Fig. 3.4. Positions are accurate to within 2 cm^{-1}. Experimental resolution is 0.5 cm^{-1}.

Peak label	Position (cm^{-1})	$\Delta\nu$ (cm^{-1})	Comments
a.1	32324.7	-	Shoulder of Al line
a.2	32341.5	1.2	
b.1	32458.1	-	AlAr $^2\Pi$(3d) (0-2)
b.2	32461.8	1.2	
b.3	32471.2	1.1	AlAr $^2\Pi$(3d) (0-3)
b.4	32474.4	0.9	
b.5	32483.9	0.6	AlAr $^2\Pi$(3d) (0-4)
b.6	32495.0	1.4	AlAr $^2\Pi$(3d) (0-5)
b.7	32501.9	1.5	AlAr $^2\Pi$(3d) (0-6)
b.8	32506.6	1.3	AlAr $^2\Pi$(4p) (0-3)
c.1	32471.0	1.2	AlAr $^2\Pi$(3d) (0-3)
c.2	32473.6	0.9	
d.1	32580.2	1.1	
d.2	32586.6	3.2	
d.3	32589.3	1.0	
e.1	32693.2	3.0	
e.2	32697.0	1.0	
e.3	32701.7	1.2	

Table 3.3: Spectroscopic constants of AlH, AlO and OH. R_e is in Å, all other units are cm^{-1}.

State	T_e	ω_e	$\omega_e x_e$	B_e	R_e	ν_{00}
AlH						
$A\,^1\Pi$	-	1082.76	-	6.3869	1.648	23470.93
$X\,^1\Sigma^+$	0	1682.56	29.09	6.3907	1.6478	-
AlO						
$C\,^2\Pi$	33079	856	6	-	-	33018
$B\,^2\Sigma^+$	20688.95	870.05	3.52	0.60408	1.6670	20635.22
$A\,^2\Pi$	5341.7	728.5	4.15	0.5333	1.7708	5217
$X\,^2\Sigma^+$	0	979.23	6.97	0.64136	1.6179	-
OH						
$A\,^2\Sigma^+$	32684.1	3178.86	92.917	17.358	1.0121	32402.39
$X\,^2\Pi$	0	3737.761	84.881	18.911	0.96966	-

Chapter 4:

Time-of-Flight Infrared Predissociation Spectrometer

4.1 Abstract

A novel apparatus has been built to measure the infrared predissociation spectra of positive and negative cluster ions. These systems are of fundamental importance to physical chemistry, involving long-standing questions about the nature of solvation. A description of the machine is given, including the tunable infrared light source, pulsed valve and ionic cluster generation, time-of-flight spectrometry, and the computer and electronics system employed to control the instrument.

4.2 Introduction

The study of solute-solvent interactions of ionic species has long been a central problem in chemical physics. Given recent advances in non-linear optical technology,[1] molecular beam sources,[2] electronics,[3] and particle detection, methods are available which are capable of revealing the quantum mechanical structure of these fundamental systems. Solvation,[4] metal-ligand chemistry,[5] ion-solvent interactions,[6] and intracluster chemistry[7] are all the focus of a great deal of experimental and computational effort. Cluster spectroscopy seeks to bridge the gap between ion spectroscopy on the one hand and the spectroscopy of bulk samples on the other.

The technique of infrared vibrational predissociation spectroscopy and multiphoton spectroscopy was applied to ionic clusters by Lee and coworkers. Using an ion-trapping tandem mass spectrometer, they were able to obtain mass-selective spectra for ionic clusters such as $H_3^+(H_2)_n$ (n = 1 to 3),[8] the solvated hydronium ion $H_3O^+(H_2O)_n$ (n = 1 to 3),[9] and $NH_4^+(NH_3)_n$ (n = 1 to 10).[10] In related studies, Lisy and coworkers have examined the infrared spectra of systems such as $Na^+(NH_3)_n$ (n = 6 to 12),[11] and $Na^+(MeOH)_n$ (n = 3 to 25)[12] in a continuous beam quadrupole mass selective instrument. The machine described in this chapter also determines the spectra of cluster ions, but uses pulsed time-of-flight methods based on the ion photodissociation spectrometer developed by Johnson and Lineberger.[13] A similar instrument operating at visible wavelengths has been described by Duncan and coworkers.[14]

In order to illustrate the versatility of time-of-flight cluster ion spectroscopy, a few representative experiments will be mentioned. Lineberger and coworkers have

recorded the photodissociation and recombination dynamics of $I_2^-(CO_2)_n$ cluster ions in a tandem time-of-flight instrument.[15] Brucat and coworkers have investigated solvated metal systems such as $V^+(H_2O)$.[16] In addition, Duncan and coworkers have used visible electronic spectroscopy to examine systems such as $Mg^+(H_2O)$[17] and $Mg^-(N_2)$.[18]

This chapter discusses a novel instrument which combines the high power and resolution of a tunable optical parametric oscillator (OPO) infrared laser with a reflectron time-of-flight instrument for mass selection and a variety of novel ion cluster sources. The result has been a versatile instrument which has been applied by the Okumura group at Caltech to study systems such as SiH_7^+,[19] $H^+(HNO_3)(H_2O)_n$ (n = 0 to 4),[7] $NO^+(H_2O)_n$ (n = 1 to 5)[20] and $HClONO_2^+$.[21]

4.3 Experimental

The time-of-flight infrared predissociation spectrometer has been described previously.[21,22] The reader is referred to these excellent accounts for more in-depth information. The current section seeks first to provide information consisting of descriptions and drawings of components which are not documented in other locations. Second, this chapter will give a brief description of the apparatus, and in addition will attempt to provide operating instructions for new users. An overview of the machine is given in fig. 4.1.

4.3.1 Pulsed Valve and Ion Cluster Formation

The heart of the ion cluster source is a piezoelectric pulsed valve based on the design of Proch and Trikl.[23] Gas was supplied to the valve by a stainless steel inlet manifold pumped by a 2" diffusion pump. The diffusion pump was crucial to the experiment as the presence of trace amounts of halogens or especially water could have a profound impact on the ion distribution of the source. An electronically controlled pair of mass flow controllers (MKS 1100 series) can be used to prepare precise mixtures of source gases. Alternatively if a single carrier gas is to be seeded with vapor from a liquid sample, a regulator may be placed on the gas cylinder. The gas then flows through a bubbler containing the liquid. The control circuit used a novel pulse generator, with the length and voltage of the control pulse proportional to the error signal generated between the pressure transducer and a set point. A diagram of the circuit is given in fig. 4.2.

Two methods were used to ionize the gas pulse. The first produced colder clusters and is based on a high pressure glow discharge between two electrodes in a flow channel attached to the pulsed valve face. A diagram of the geometry of the source is given in fig. 4.3. The discharge was driven by a high voltage pulse from a thyratron. Conduction in the thyratron tube is based on a plasma discharge, meaning that it is much more forgiving than solid state components, should the output be shorted, give inductive feedback, or otherwise cause the circuit to malfunction. The tube was provided by a Russian manufacturer (contacted through General Electric). A diagram for this circuit is given in fig. 4.4. Sources employing this circuit successfully produced water clusters,[24] SiH_7^+ [19], and $H^+(HNO_3)(H_2O)_n$ (n = 0 to 4).[7] A mechanical drawing of the plasma

chamber used in the water cluster experiment is given in fig. 4.5. An addition to this source was made to allow a second valve (solenoid actuated, Ford fuel injector valve, Pep Boys) to inject gas into the gas channel of the source. The valve was driven by a home-made high current driver circuit.[3] By seeding water into the piezo valve and methanol into the solenoid valve, mixed protonated methanol/water clusters were created.

In addition, a number of versions of an electron gun were built in order to ionize the gas pulse. In the first version the cathode ray tube of an oscilloscope was cut open with a diamond wheel. When it was turned on *in vacuo* it was discovered that the gun provided a much lower electron current than that required for the experiment. A second version based on the design of Erdman and Zipf[25] did not provide a sufficiently small angular divergence. A third version was built, based again on the design of Zipf, after extensive modeling of the electron beam behavior. The modeling was conducted using the program Simion, a program which will solve ion trajectories in a series of electrostatic lenses.[26] The addition of a modular filament mount was critical to the utility of the final design. The mount could be removed as a unit from the gun allowing filaments to be easily changed. Thoriated iridium filaments with platinum tabs were purchased from Electron Tech Inc. (Model 201-998-8100, 0.002" x 0.0027" x 3"), and were cut and spot welded onto the terminals of the mount.

4.3.2 Tandem Time-of-flight Spectrometer and Electronics

The instrument chamber consists of three regions of differential pumping. The main gas load from the pulsed valve is evacuated in the source chamber. This chamber is 50 x 50 x 75 cm^3 and is pumped by a freon-baffled 10" diffusion pump (CVC PVMS-1000, 5000 *l*/s). The electron gun, discharge ionization source and pulsed valve are housed in this region. The pressure in the source chamber varied from 5 x 10^{-4} to 3 x 10^{-5} Torr when the valve was in operation. A homemade skimmer (fig. 4.6) collimates the beam before it goes into the time-of-flight extraction chamber.

The second region of the machine serves as a time-of-flight tube, and houses the extraction optics for a three stage Wiley-McLaren type time-of-flight mass spectrometer.[27] The ions were extracted at an angle of 3° from a line formed by the pulsed valve and beam skimmer. In this near-parallel configuration more ions are gathered in each mass packet as compared to perpendicular extraction. The drawback of this configuration is decreased mass resolution. The resolution was improved, however, by using a three stage ion acceleration stack (Kimball Physics eV system) which was calculated to result in both first and second-order spatial focusing. The first pulsed acceleration region was 4.4 cm long, and the two consecutive acceleration regions were 3.0 and 4.8 cm. Home made high voltage pulse generators were used, based on the design of Baker and Johnson for positive ions[28] and of Horowitz and Hill[3] for negative ions.

Two sets of parallel plate deflectors were used to steer the beam. Each set consisted of two pairs of plates, one pair for vertical control and one pair for horizontal control. One plate in each pair was grounded while the other was set to a voltage in the

range of ±110 V. Two einzel lenses were used to focus the beam. A simulation of the focusing effect of a retarding einzel lens at 350 V on a beam of 900 eV ions is shown in fig. 4.7. The program Simion[26] was used to model the performance of the lenses, the ion extraction optics and the reflectron. The ion optics and time-of-flight tube were pumped by a freon baffled 6" diffusion pump (CVC PVMS-100, 2500 *l*/s) in addition to a freon baffled 4" diffusion pump (CVC PMC-721, 700 *l*/s).

The third vacuum region served as a laser interaction region and particle detection chamber. It consisted of a 35 cm high, 70 cm dia. cylindrical stainless steel vessel. The curved top could be removed to allow access to the mass gate, reflectron and microchannel plate ion detector. The chamber was pumped by an Airco turbomolecular pump (Model 514, 500 *l*/s), resulting in an oil-free environment for the detector. The flight path of the ions passes through the mass gate and enters the reflectron. The reflectron is a linear repulsive electric field at an angle of 4° relative to the ion flight path. The reflectron helps to spatially focus the ions since ions with a slightly higher energy will penetrate farther into the field. This results in a longer flight time for faster ions and allows them to converge with lower energy particles at the detector. After a near-reversal of direction in the reflectron, the ions strike a microchannel plate detector (Galileo Electro-Optic, Model FTD 2003, dual chevron detector, typical operating conditions 800 V/plate).

Since each ion travels at a velocity of $(2V_{TOF}\, e \,/\, m_{ion})^{1/2}$, when the ions reach the laser interaction region they will have separated into spatially discrete mass packets. The mass gate acts to allow only the packet of interest to pass into the laser interaction region.

The mass gate is essentially a horizontal deflector. A timing circuit pulses the deflector voltage to zero when the mass packet of interest passes through. In this way noise due to background counts is reduced, and interpretation of the data is simplified. Next, the infrared laser (described in section *4.3.3*) irradiates a single mass packet. If the ion absorbs the photon and undergoes predissociation, a fragment ion results with the same velocity as the parent, but a different mass. When the reflectron is set to a voltage equal to the voltage used for the parent times the ratio of the fragment mass to the parent mass, the fragment will follow the same path though the reflectron to the detector as the undissociated parent would have at the old reflectron voltage setting. In this way the arrival time of the photofragment may be determined for subsequent observation on the oscilloscope or integration by the ion signal detection electronics.

The ion signal is amplified by a homemade pre-amp (26 dB) shown in Appendix A, before being recorded by a transient digitizer and signal averager (LeCroy 8818/6010). The averaged signal was transferred *via* a GPIB interface to an IBM-AT computer for display and analysis using the program TOFVIEW2.[21]

4.3.3 Optical Parametric Oscillator

Infrared radiation was generated using an angle-tuned $LiNbO_3$ optical parametric oscillator (OPO) based on the design of Brosnan and Byer.[29,30] The OPO is a device for splitting the pump photon into two output photons each at a lower frequency. $LiNbO_3$ (Inrad, 10 x 10 x 50 mm, AR coated for 1.06 μm) is a noncentrosymmetric crystal possessing a nonlinear polarizability.[31] Because of the crystal properties, the oscillating

electric field of a pumping laser (Quanta Ray GCR-12 Nd:YAG, 10 Hz, typical pulse energies of 100 to 200 mJ) induces an oscillation in the crystal at two frequencies which sum to the pumping frequency. $LiNbO_3$ is a type I crystal, meaning that the input beam is an extraordinary (*e*) wave, while the output beams are both ordinary (*o*) waves. The pump photon, and the two resultant photons (termed signal and idler) are subject to the following frequency and phase (or wave-vector) conditions:

$$\omega_p = \omega_i + \omega_s \text{ where } (\omega_i \leq \omega_s) \quad (1)$$

$$k_p = k_i + k_s \quad (2)$$

For a pump beam at 1.064 μm or 9400 cm^{-1}, the idler frequency ω_i can range from 2600 cm^{-1} to 4700 cm^{-1}, while the signal frequency ω_s can range from 4700 cm^{-1} to 6800 cm^{-1}. The idler frequency thus covers many features of interest to physical chemists, such as vibrations of H_2O (ν_s = 3654 cm^{-1}, ν_a = 3756 cm^{-1}), CH (ν_s ~ 3000 cm^{-1}), and NH (ν_s ~ 3300 cm^{-1}). In order for the OPO to divide one photon into two, the phase-matching condition (2) must be met. If the angle of the pumping beam is moved off the axis of the resonant cavity, condition (2) is no longer strictly valid. However, signal and idler beams are still generated in the non-collinear arrangement. The advantage to pumping the crystal at an angle to the cavity axis, as pictured in the bottom of fig. 4.8, is that the signal, idler, and pump beams leave the OPO at different angles. It is therefore possible to separate the beams spatially instead of by using expensive broadband infrared reflectors or filters.

The resonant cavity of the OPO consisted of a diffraction grating (Scientific Measurement Systems, 1.3 μm blaze, 295 groove/mm, 58 x 58 x 10 mm) and an output

coupler (CVI, 1" dia. infrasil, 3' wedge, R = 60% at 2 μm, no coating on back surface), giving an optical path length of 20 cm. In the cavity are two beam expanding prisms (Janos, ZnSe, hypotenuses 2.5 cm and 4.5 cm, longer normal face AR coated at 1.55 μm with ThF_4) which increase the number of lines of the grating utilized in the resonant cavity, thus improving the resolution of the output beam (~1.5 cm^{-1}). In addition to the beam expanding prisms and the $LiNbO_3$ crystal, the cavity contains an input coupler (CVI, 1" dia., 45°, 1.064 μm) which reflects the Nd:YAG beam through the crystal. A diagram of the OPO is given in fig. 4.8.

Preventing damage to the OPO crystal was a major concern, and several steps were taken to avoid or minimize damage. It was found that if the crystal was mounted using 0.006" Teflon shims, rather than by being in direct contact with the brass support block, that damage due to mechanical stress and chipping could be reduced. In addition, the pump beam spot size, profile, and power were monitored closely to prevent hot spots in the beam. Burn patterns of the pump beam were taken regularly to prevent damage to optics earlier in the beam path from propagating into the crystal. Finally and most importantly, the surfaces of the crystal were inspected and cleaned regularly to prevent surface damage from spreading into the interior of the crystal.

Two methods were used to calibrate the OPO. A rough calibration of the signal wavelength over the whole operating range of the OPO was obtained by directing the beam through a 0.5 m Jarrell-Ash monochromator (Thermo Jarrell Ash, interferometrically ruled at 295.27 grooves/mm, 1.3 μm blaze) with an infrared diffraction grating onto a power meter (Newport).

A highly accurate calibration was possible using the method of photoacoustic spectroscopy.[32] The signal or idler beam was directed through a cylindrical aluminum cell containing 10 to 50 Torr of a calibration gas sample. The cell has CaF_2 windows and a miniature hearing aid microphone (Knowles Electronics, (708) 250-5100, model EK3031) to record the photoacoustic excitation. Examples of the photoacoustic spectra of methane and hydrogen chloride are shown in fig. 4.9. By employing one of the gases HCl, C_2H_2, HBr, and CH_4 in the cell, almost all of the range of the OPO output may be reliably calibrated using standardized tables.[33]

An empirical crystal tuning curve was created by measuring the crystal position as a function of grating position. The crystal and grating angles are controlled by stepping motors, the integral positions of which were recorded. This data was fit to a fourth degree polynomial which was used by the program OPODATA to compute crystal positions for a given grating position.[21] Values of the coefficients of the function

$$N_{cryst} = a + b(N_{grat}) + c(N_{grat})^2 + d(N_{grat})^3 \qquad (3)$$

were determined to be $a = 1.4477 \times 10^4$, $b = 4.2693 \times 10^{-1}$, $c = -4.1392 \times 10^{-7}$, and $d = -2.2447 \times 10^{-10}$. These values were observed to change if the crystal was changed. The grating position was also used by the computer to derive the wavenumber of the output beam. The program employed a cubic spline function to interpolate between the empirically measured calibration points.

One problem encountered was that a water impurity in $LiNbO_3$ crystals in the region of 3495 cm^{-1} caused a drop in the output power of the OPO. Different $LiNbO_3$ crystals were found to have different amounts of absorption due to this impurity. A

measurement of the signal power at a pumping energy of 120 mJ/pulse as a function of wavelength for one crystal (Inrad) is shown in fig. 4.10.

A significant amount of crosstalk was found between adjacent input channels on the A/D converter used to record the data. It was determined that if channels 0, 2, and 4 were used instead of the adjacent channels 0, 1, and 2, crosstalk was no longer a problem. A similar problem was encountered with a more advanced version of the Keithley-Metrabyte DAS-1600 board used in the experiments detailed in chapters 2 and 3.

4.3.4 Operation of the Machine

A brief overview of the components of the time-of-flight infrared predissociation spectrometer has been given in the previous sections. In this section directions are given for operating the machine, with special attention to setting the timing and configuring the computers.

Warm up the laser at least 30 minutes before permitting the beam to pass through the OPO. The OPO should be aligned, and the idler aligned through the machine before beginning the following procedure.

A mass spectrum of the desired species should first be realized which shows a strong (hollow center) peak on the oscilloscope belonging to the ion of interest. This involves first setting up the source gas line, possibly using a bubbler to seed a molecule into the carrier gas. Either the electron gun or the discharge source may be used to produce the clusters. The extraction pulse and ion optics should be initially set to values recorded in the lab notebook, and after a mass spectrum is observed, these settings may

be modified to optimize peak intensity and mass resolution. Next the mass gate should be turned on, and the width and delay of the gate modified so that only the mass packet of interest reaches the detector.

A scan should now be recorded using the computer 'TOFU' with a bin time of 10 ns, and with the integration cursors set up (using baseline subtraction) to integrate the parent ion peak. Next, change the reflectron voltage to be equal to the old reflectron voltage (typically 1000 V) times the ratio of the mass of the fragment to that of the parent ion. The fragment ions will now arrive at the detector at a time corresponding to the previously set integration markers. The detector voltage can be turned up at this point to increase sensitivity, but be sure that the parent ion signal is not larger than $\pm$ 0.5 V so it does not damage the transient digitizer. The arrival time of the parent ion to the laser interaction region may now be calculated using menu option Alt-C of the program TOFVIEW2.

Next, the laser and SRS delay generator should both be set for external triggering. The EG&G pulse generator will now trigger the SRS pulse generator in addition to the flashlamp and Q-switch of the Nd:YAG laser. Check the burn pattern (front and back) and power of the pump beam before allowing it to pass through the OPO. Change the Q-switch delay using the EG&G pulse generator (channel B) to achieve the desired pump power. Next, use a reverse biased silicon diode to check the timing of the 1.064 μm pulse relative to the mass peak appearing on the oscilloscope (the mass peak will reach the laser interaction region before it reaches the detector). The most direct method is to use the oscilloscope to measure the delay between the time-of-flight extraction trigger

and the Nd:YAG pulse, and to set this value to the arrival time indicated by the program TOFVIEW2 (menu option Alt-C). Remove the beam stop and allow the Nd:YAG beam to pass through the OPO. Take more burn spots at the output of the OPO to make sure that the beam is not clipping. The idler beam should be aligned through the chamber, and the power measured at the far side of the machine. The measurement should be in the range of 3 to 4 mJ. The machine is now ready to record frequency scans, provided that the timing and wavelength of the OPO pulse are correct.

The most difficult step in the procedure is determining the correct value for the OPO delay time when the frequency of the ion absorption is not known. The most direct method is to use a signal averaging digital oscilloscope, and alternately change the OPO wavelength and timing in an effort to directly observe a photofragment peak on the oscilloscope. The photofragment peak is typically 100 ns FWHM, whereas the parent ion peak may be 1 μs FWHM. It was found that the arrival time of the mass packet can vary by up to 2 μs from the time indicated by the timing calculation.

During the scan the operator should monitor beam walk, beam clipping, and output power. The crystal angle should be actively monitored during the scan to ensure maximum power. Scan conditions may be set for a large step size (typically 5 cm^{-1}) for a survey scan, or a smaller size (typically 1.5 cm^{-1}) for final (low-resolution) data.

Next, the computer TOFU should be configured to communicate the proper data to the computer LASER. The menu option Alt-V, set laser parameters, will allow foreground (photodissociation (PD) + metastable (M) integral, *i.e.*, raw data), background (M), or difference (PD - M) integrals to be communicated. The computer

TOFU communicates with the SRS digital delay generator *via* a GPIB interface, allowing it to change the timing so that the laser will miss the ion packet. In this way the background signal due to metastable ion decay may be measured. In order to record a scan, press Alt-L on TOFU and Alt-S on LASER (laser must be set to ionspec mode). Check to be sure that the communication interface is working correctly, and then monitor the OPO and mass spectra as the data is being collected.

4.4 Conclusion

A description has been given for a novel and powerful time-of-flight infrared predissociation ion spectrometer. The machine uses a novel ion cluster source to generate positive or negative cluster ions. Through the technique of time-of-flight infrared predissociation spectroscopy the action spectra of these clusters is recorded. The spectra of a number of fundamental systems have been recorded using the instrument.

4.5 References

[1] A. Yariv, *Optical Electronics*, Saunders College Publishing, Philadelphia (1991).

[2] G. Scoles, Ed., *Atomic and Molecular Beam Methods*, Oxford University Press, Oxford (1988).

[3] P. Horowitz and W. Hill, *The Art of Electronics*, Cambridge University Press, Cambridge (1989).

[4] P. Kebarle, *Ann. Rev. Phys. Chem.* **28**, 445 (1977).

[5] M. T. Bowers, Ed., *Gas Phase Ion Chemistry*, New York (1979).

[6] J. P. Maier, Ed., *Ion and Cluster Ion Spectroscopy and Structure*, Elsevier, Amsterdam (1989). T. D. Märk and A. W. Castleman, Jr., *Adv. in Atomic and Mol. Phys.* **20**, 65 (1985).

[7] Y.-B. Cao, J.-H. Choi, B.-M. Haas, M. S. Johnson, and M. Okumura, *J. Chem. Phys.* **99**(11), 9307 (1993). Y.-B. Cao, J.-H. Choi, B.-M. Haas, and M. Okumura, *J. Phys. Chem.* **98**(47), 12176 (1994).

[8] M. Okumura, L. I. Yeh, and Y. T. Lee, *J. Chem. Phys.* **88**(1), 79 (1988).

[9] L. I. Yeh, M. Okumura, J. D. Myers, J. M. Price, and Y. T. Lee, *J. Chem. Phys.* **91**(12), 7319 (1989).

[10] J. M. Price, M. W. Crofton, and Y. T. Lee, *J. Phys. Chem.* **95**(6), 2182 (1991).

[11] T. J. Selegue and J. M. Lisy, *J. Phys. Chem.* **96**(11), 4143 (1992).

[12] T. J. Selegue, N. Moe, J. A. Praves, and J. M. Lisy, *J. Chem. Phys.* **96**(10), 7268 (1992).

[13] M. A. Johnson and W. C. Lineberger in *Techniques for the Study of Ion-Molecule Reactions;* Farrar, J. M., Saunders Jr., W. H., Eds.; Wiley-Interscience, New York (1988) p. 591.

[14] D. S. Cornett, M. Peschke, K. Laihing, P. Y. Cheng, K. F. Willey, and M. A. Duncan, *Rev. Sci. Inst.* **63**(4), 2177 (1992).

[15] J. M. Papanikolas, V. Vorsa, M. E. Nedal, P. J. Campagnola, H. K. Buchenau, and W. C. Lineberger, *J. Chem. Phys.* **99**(11), 8733 (1993).

[16] D. E. Lessen, R. L. Asher, and P. J. Brucat, *J. Chem. Phys.* **93**(8), 6102 (1990).

[17] K. F. Willey, C. S. Yeh, D. L. Robbins, J. S. Pilgrim, and M. A. Duncan, *J. Chem. Phys.* **97**(12), 8886 (1992).

[18] D. L. Robbins, L. R. Brock, J. S. Pilgrim, and M. A. Duncan, *J. Chem. Phys.* **102**(4), 1481 (1995).

[19] Y.-B. Cao, J.-H. Choi, B.-M. Haas, M. S. Johnson, and M. Okumura, *J. Phys. Chem.* **97**(20), 5215 (1993).

[20] J.-H. Choi, K. T. Kuwata, B.-M. Haas, Y.-B. Cao, M. S. Johnson, and M. Okumura, *J. Chem. Phys.* **100**(10), 7153 (1994).

[21] Y.-B. Cao, Ph.D. Thesis, California Institute of Technology (1994).

[22] J.-H. Choi, Ph.D. Thesis, California Institute of Technology (1995).

[23] D. Proch and T. Trikl, *Rev. Sci. Instrum.* **60**(4), 713 (1989).

[24] C. M. Nelson and M. Okumura, *J. Phys. Chem.* **96**(15), 6112 (1992).

[25] P. W. Erdman and E. C. Zipf, *Rev. Sci. Instrum.* **53**, 225 (1982).

[26] D. A. Dahl and J. E. Delmore, Simion Version 4.0, Idaho National Engineering Laboratory, U. S. Department of Energy (1988).

[27] W. C. Wiley and I. H. McLaren, *Rev. Sci. Instrum.* **26**, 1150 (1955).

[28] R. J. Baker and B. P. Johnson, *Rev. Sci. Instrum.* **63**(12), 5799 (1992). R. J. Baker and B. P. Johnson, *Rev. Sci. Instrum.* **64**(6), 1655 (1993).

[29] S. J. Brosnan and R. L. Byer, *IEEE J. Quant. Elect.* **QE-15**(6), 415 (1979).

[30] T. K. Minton, S. A. Reid, H. L. Kim, and J. D. McDonald, *Optics Comm.* **69**(3,4), 289 (1989).

[31] A. Yariv, *Quantum Electronics* 3rd. Ed., John Wiley and Sons, New York (1989).

[32] G. A. West, J. J. Barrett, D. R. Siebert, and K. V. Reddy, *Rev. Sci. Instrum.* **54**, 797 (1983).

[33] *Tables of Wavenumbers for the Calibration of Infrared Spectrometers*, The IUPAC Commission on Molecular Structure and Spectroscopy, Butterworth, Washington D. C. (1961).

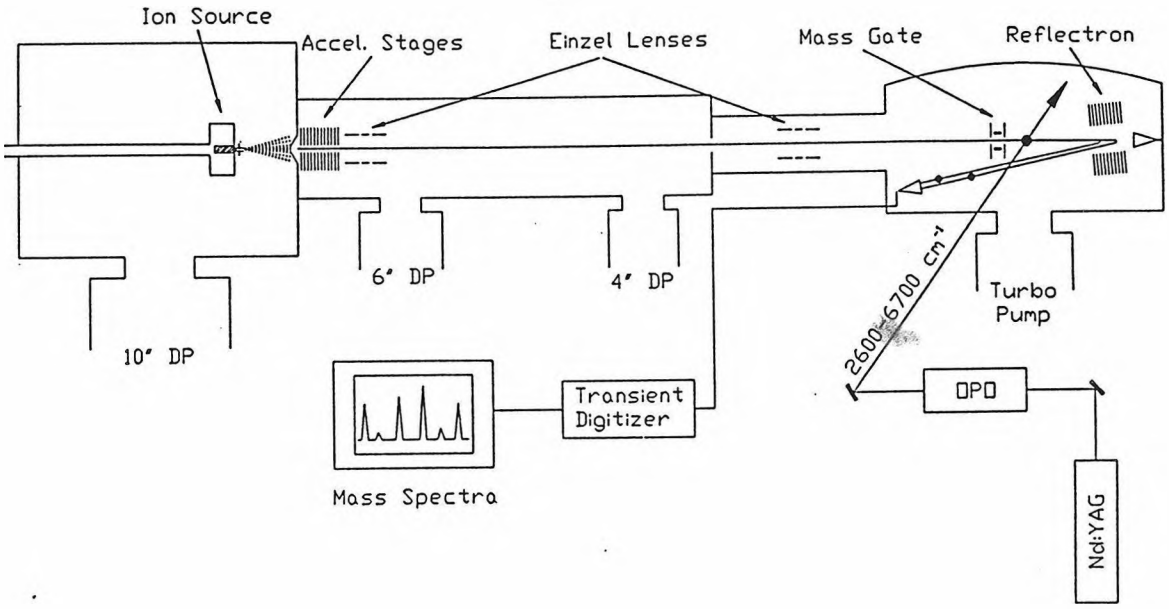

Figure 4.1 Schematic diagram of the time-of-flight infrared predissociation spectrometer. Three separate vacuum regions are shown, in addition to the optical parametric oscillator infrared source, and data collection system.

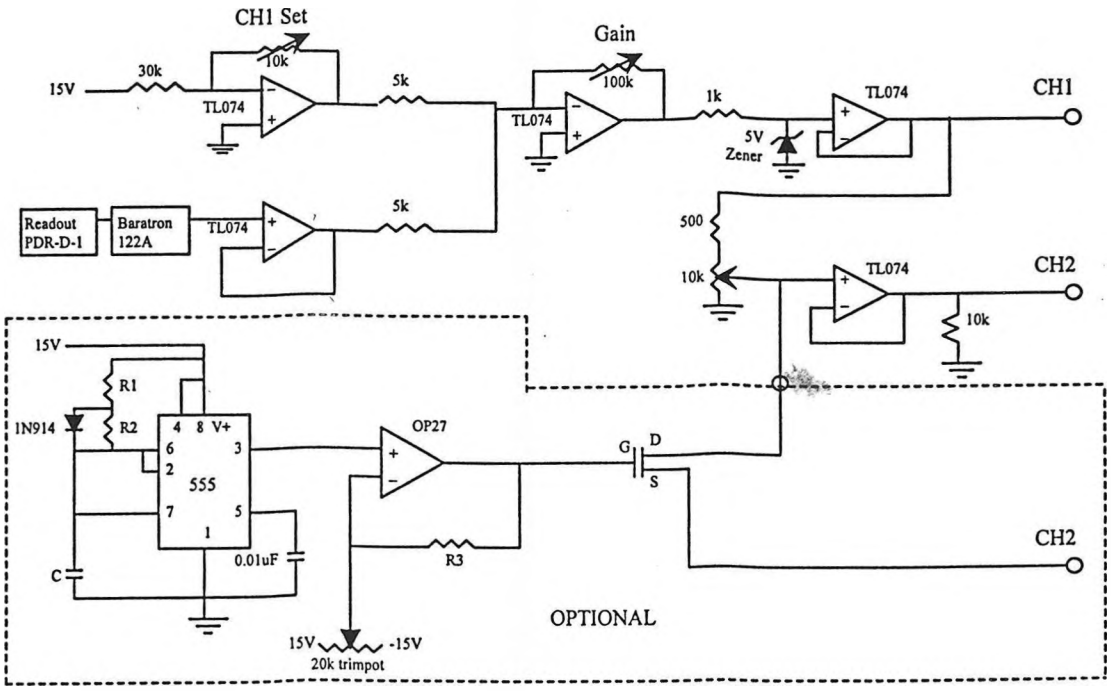

Figure 4.2 Diagram of the pulsed circuit which drives the mass flow controllers (MFC). The user may set a frequency for the 555 timer chip, which controls duty cycle for MFC 2. In this manner gas mixtures at very small concentrations may be made; the system effectively regulates below the minimum flow listed for the flow transducer.

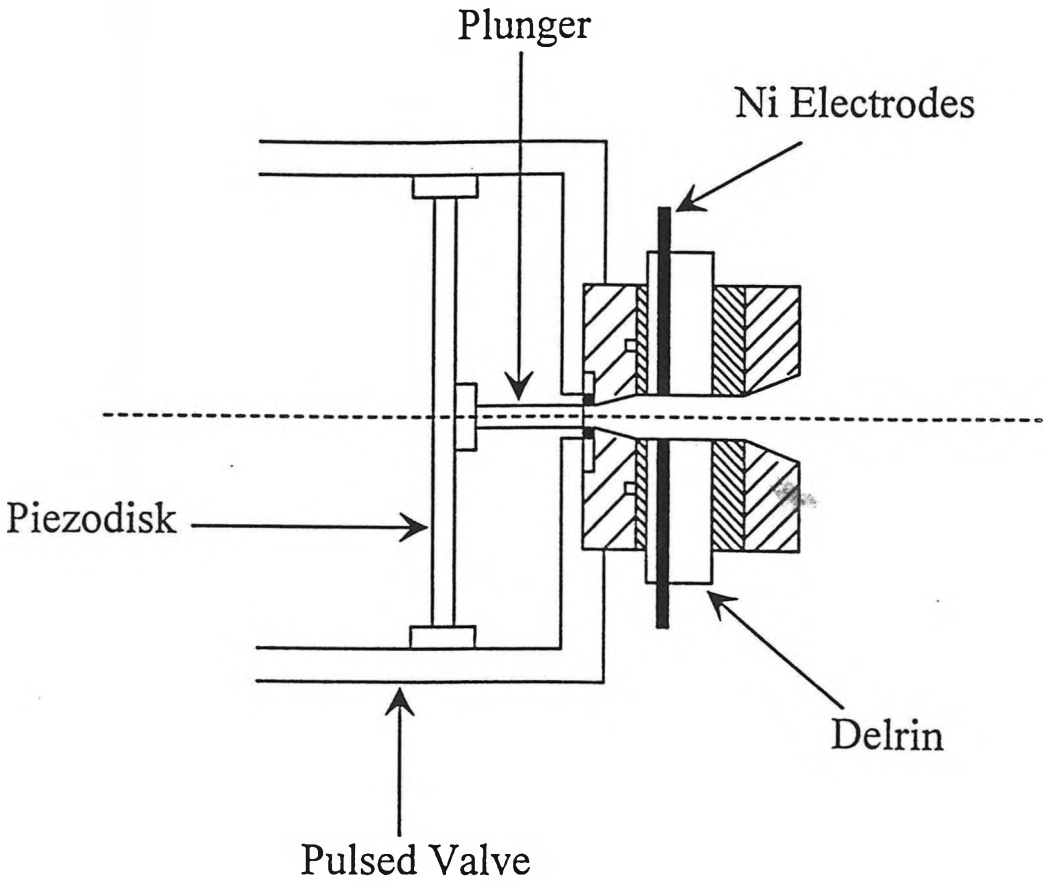

Figure 4.3 This diagram illustrates the configuration used for the pulsed glow discharge cluster ion source. Two electrodes create a plasma in the gas flow channel between the piezoelectric pulsed valve and the expansion nozzle. The voltage to the electrodes is pulsed by the thyratron circuit pictured in fig. 4.4.

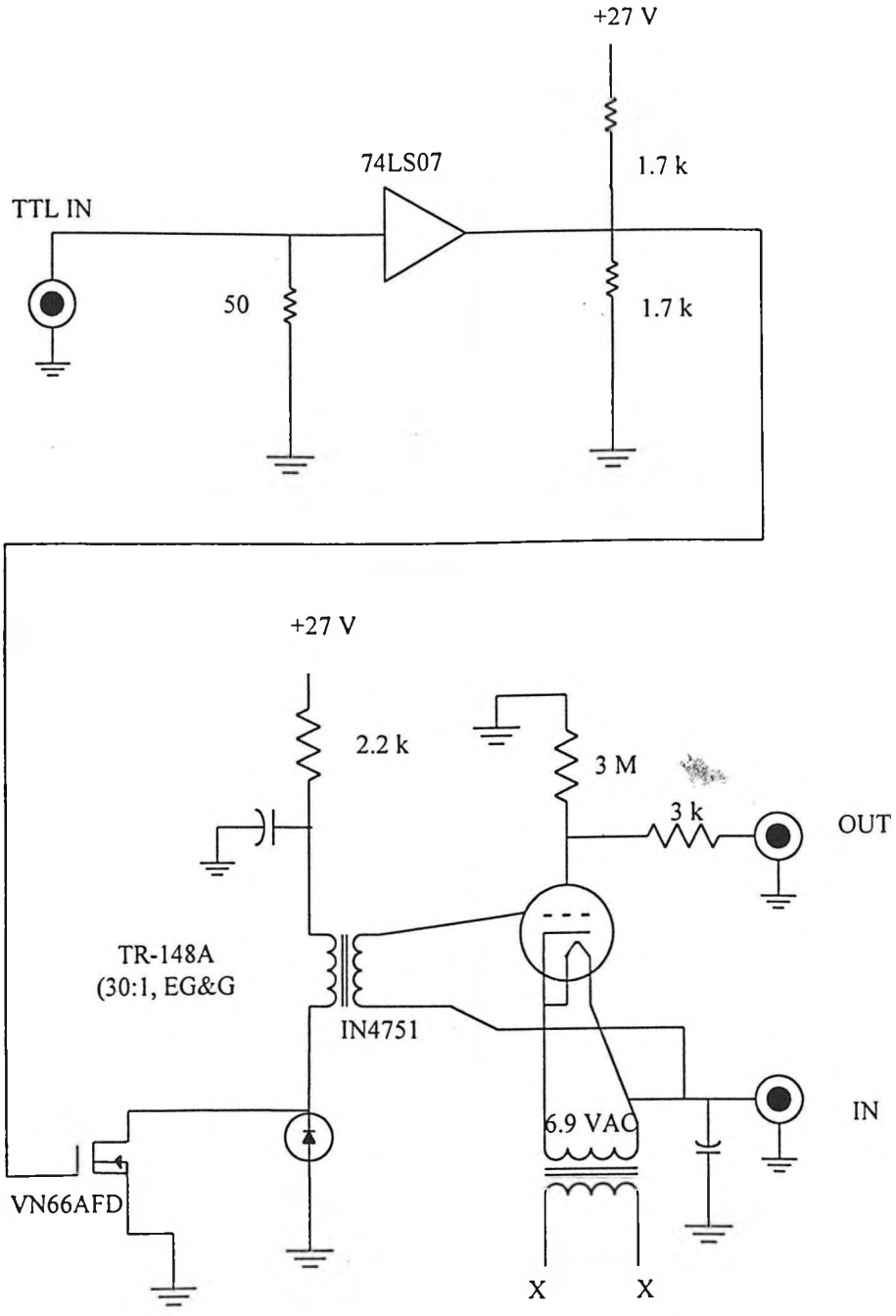

Figure 4.4 Robust circuit for applying a high voltage pulse to the glow discharge ion source. The circuit uses a trigger transformer to switch a thyratron. The thyratron uses a gas discharge to conduct electricity, and is thus resistant to a wide variety of conditions at the output of the circuit including inductive feedback and a dead short to ground.

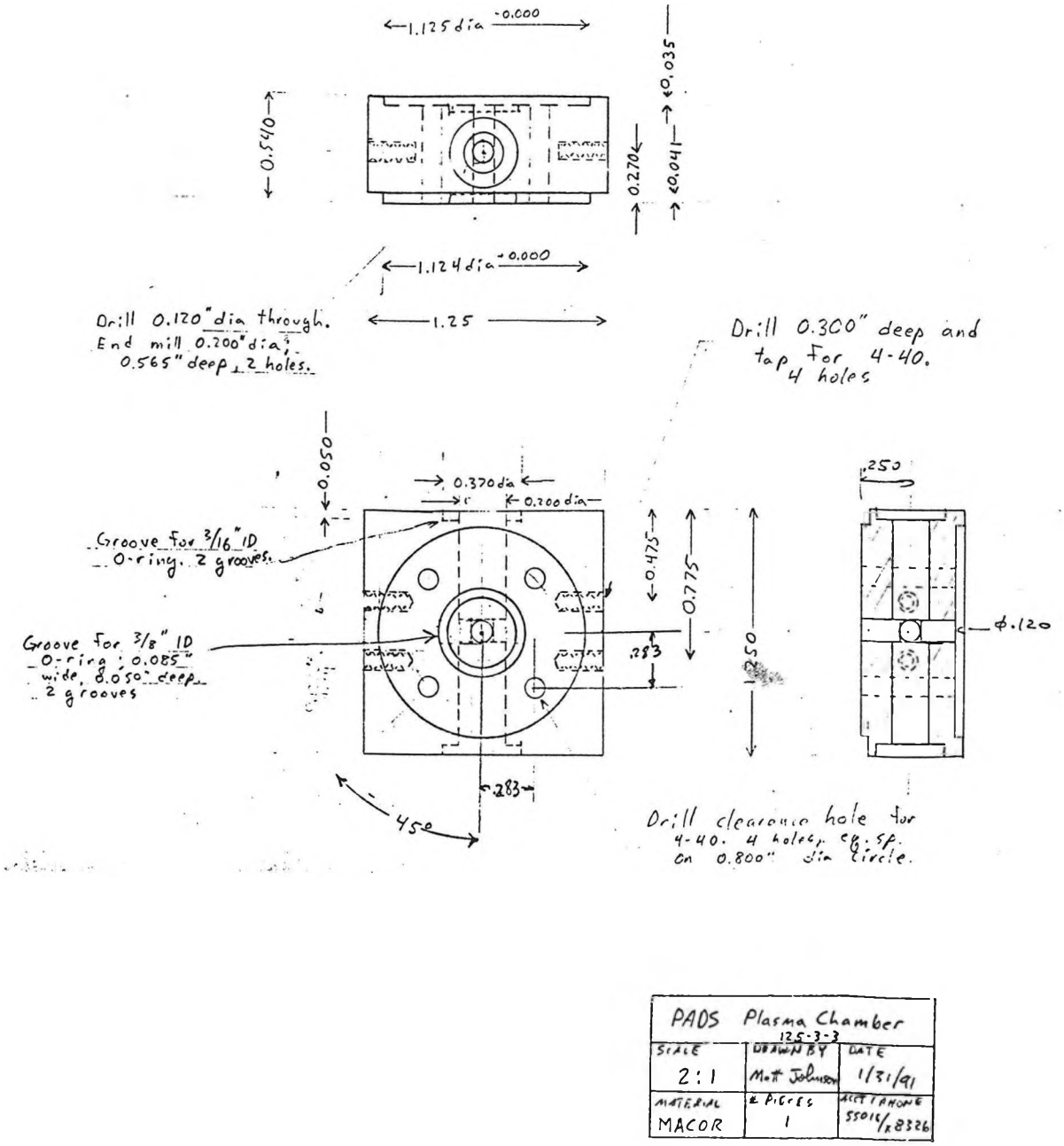

Figure 4.5 Drawing of plasma chamber used in conjunction with the thyratron pulse generator and two sharpened electrodes to reliably generate the ionic clusters used in a number of experiments. Drawings of the complete source are available, and include an adapter for a solenoid valve used as a pickup source, and a variety of flow nozzles and channel lengths and diameters.

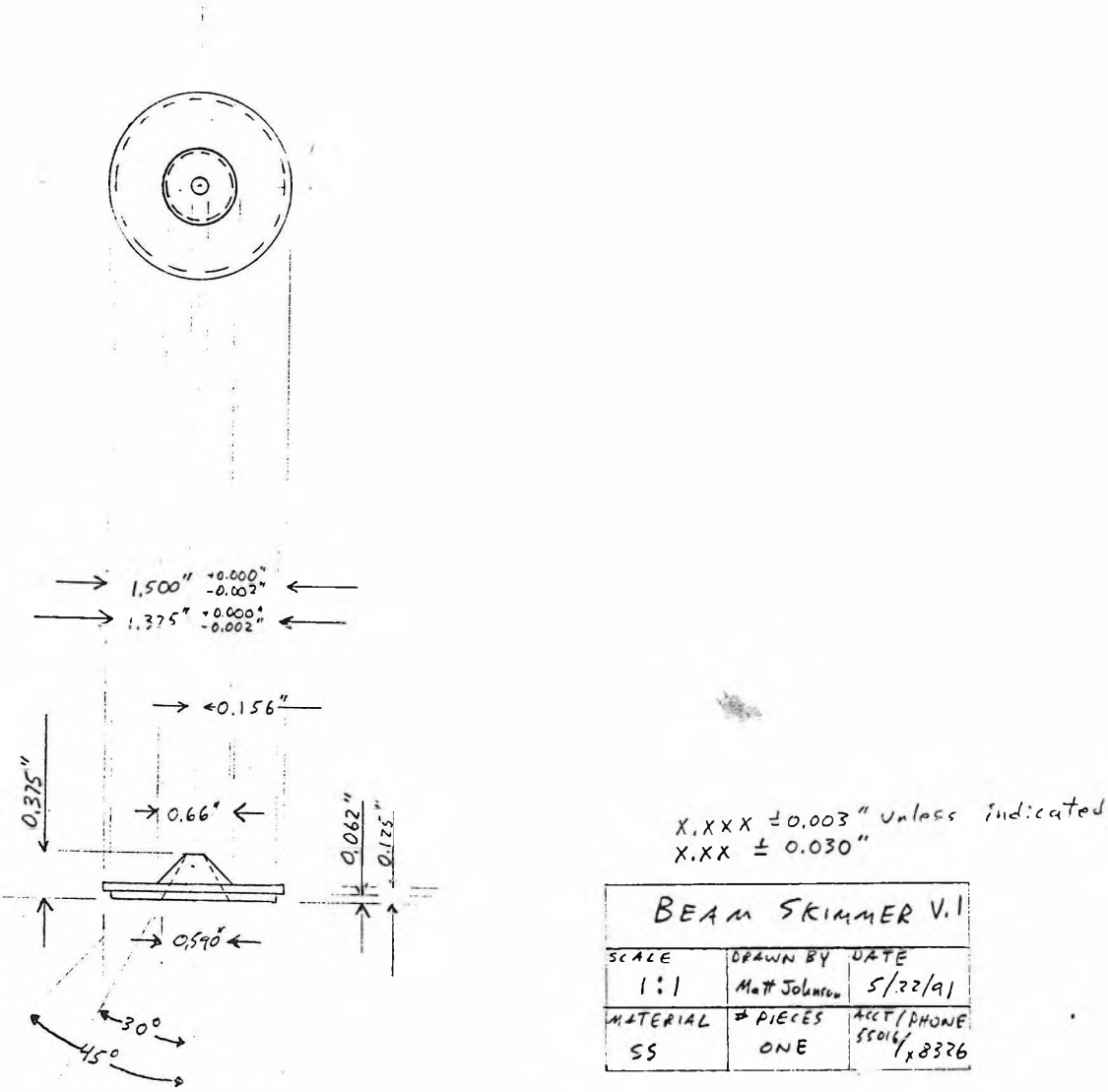

Figure 4.6 Diagram of 45° skimmer machined in the instrument shop of the Department of Chemistry at the California Institute of Technology. This robust skimmer has been in continuous use for four years.

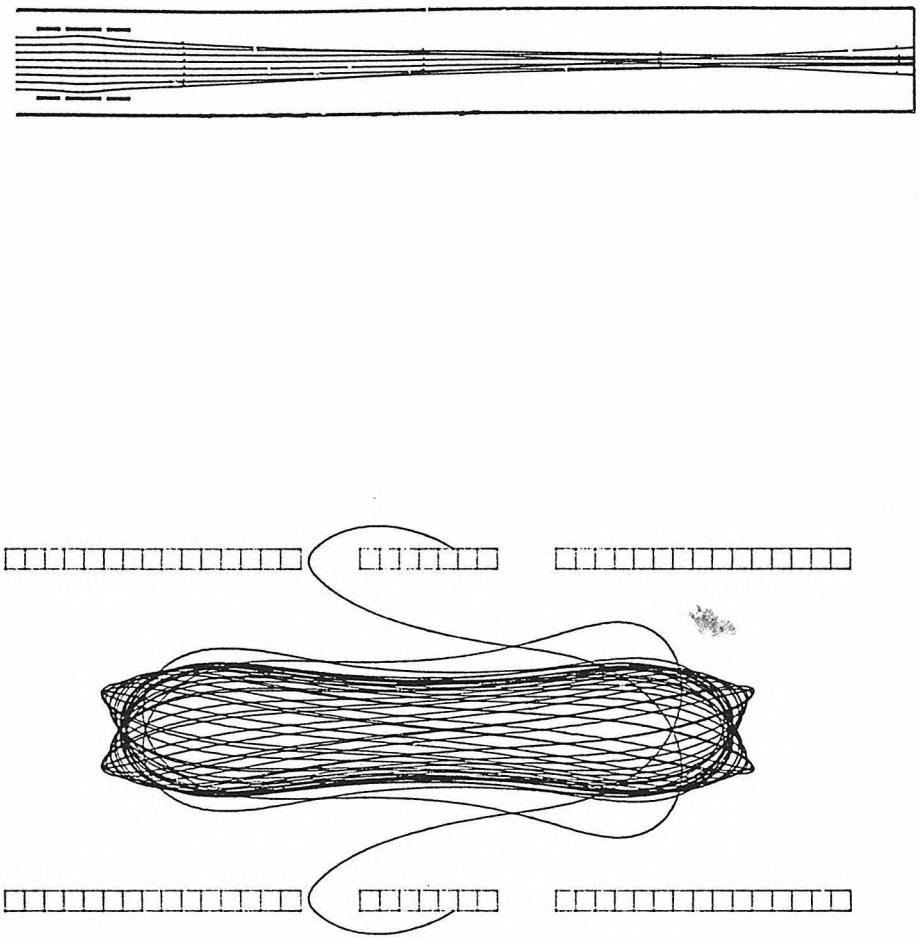

Figure 4.7 (*a*) Drawing of the focusing effect of a 350 V retarding einzel lens on a 900 eV ion beam. (*b*) Drawing showing how a low energy ion may become trapped in the field of the einzel lens. Modeling performed using the program Simion from INEL.

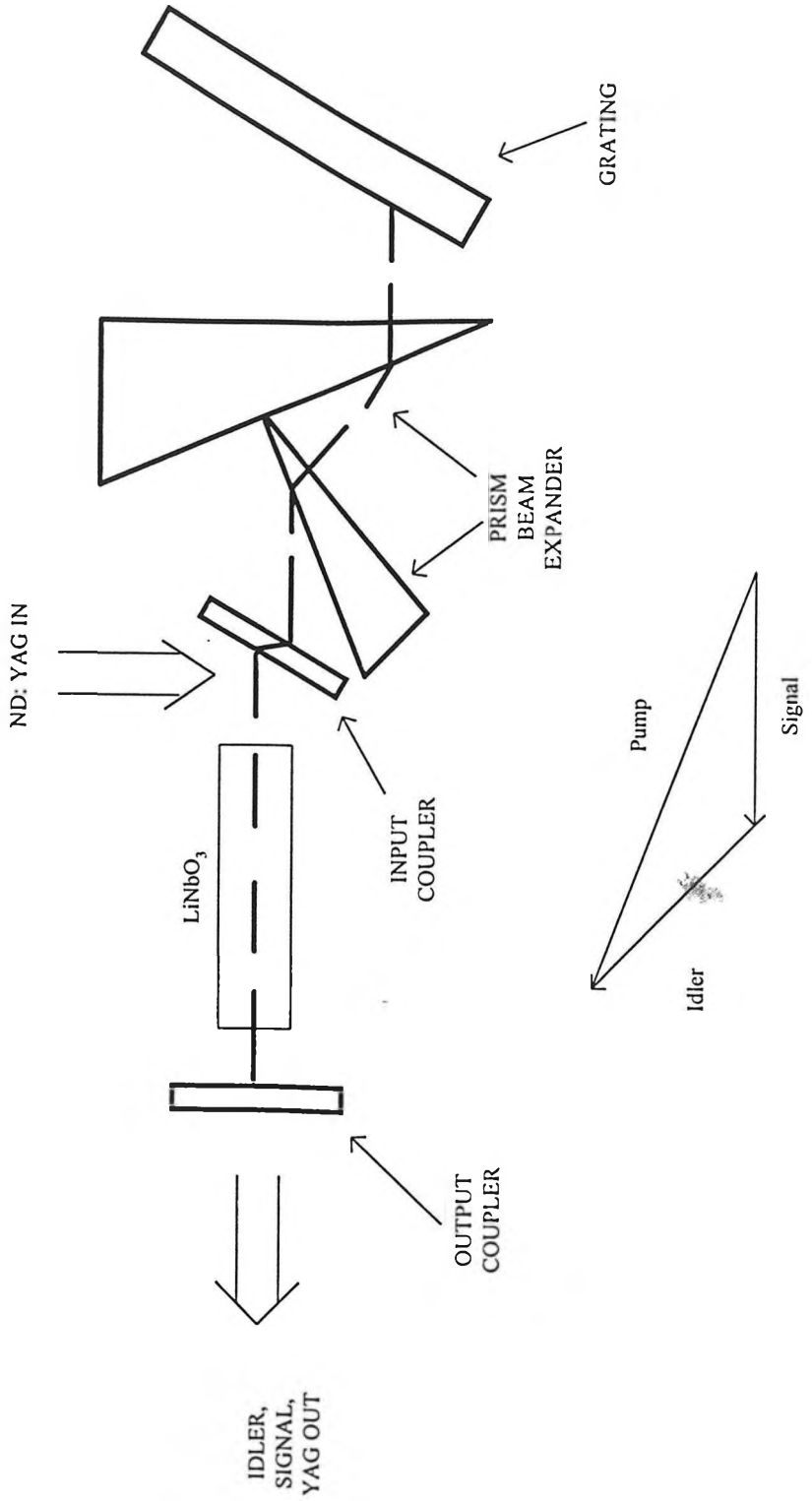

Figure 4.8 Schematic diagram of the optical parametric oscillator cavity, showing the input coupler, $LiNbO_3$ crystal, beam expanding prisms, grating and output coupler. The vector diagram at the bottom of the figure illustrates how the k vectors of the pump, signal, and idler beams are related. This feature is used to spatially separate the beams after they exit the OPO.

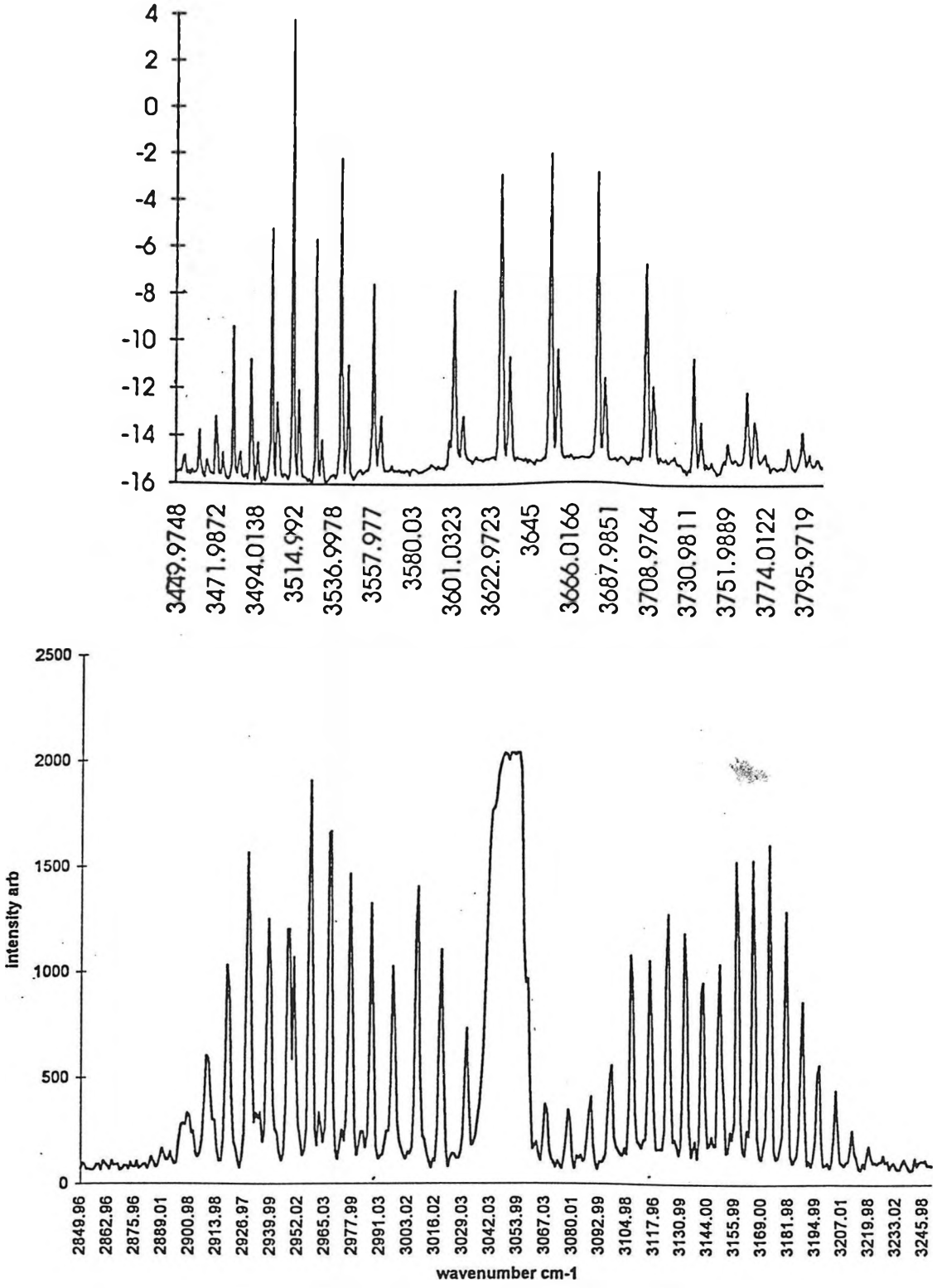

Figure 4.9 Photoacoustic spectra taken using the OPO. (*a*) Overtone spectra of hydrogen chloride, using the signal beam. (*b*) Spectra of fundamental vibration of methane, using the idler beam. Note that the program OPODATA records spectra in terms of the idler wavenumber, whether or not the idler beam is being used.

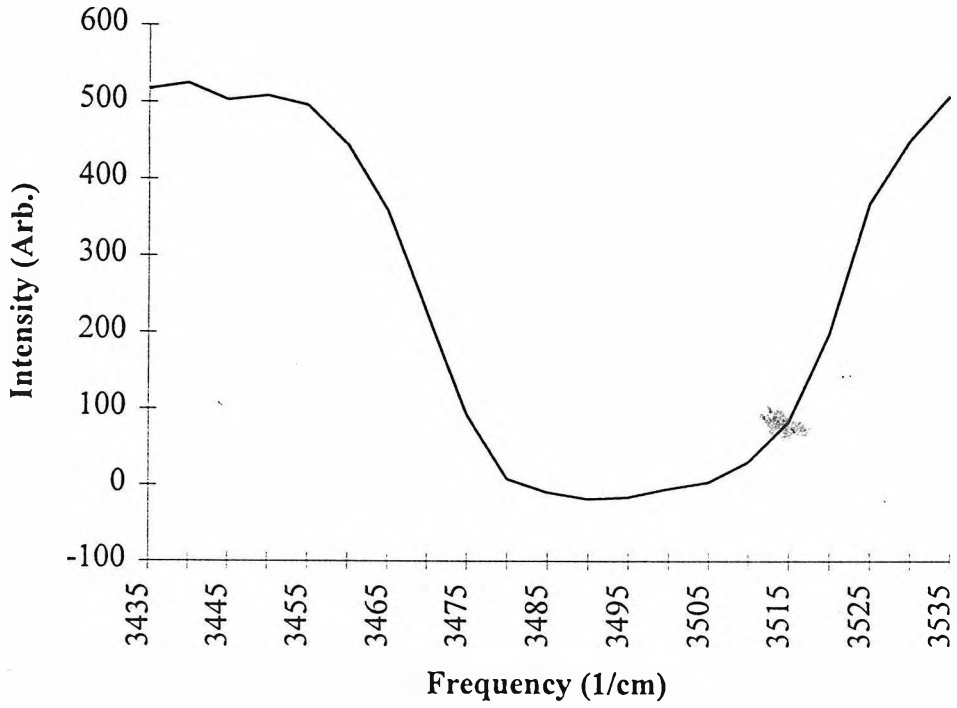

Figure 4.10 Power spectrum showing the dip in signal power as the grating is tuned through an absorption in the $LiNbO_3$ crystal due to a water impurity.

Chapter 5:

Vibrational Spectroscopy of $I^-(H_2O)$ and $I^-(H_2O)_2$

5.1 Abstract

The infrared predissociation spectra of the iodide-water clusters $I^-(H_2O)_n$ for n = 1 and 2 have been recorded for the first time. A reflectron time of flight mass spectrometer was used in conjunction with a pulsed cluster source and a tunable infrared laser to record the action spectra of these fundamental solvated anions. Absorptions were seen at 3294 cm^{-1}, 3417 cm^{-1}, and 3710 cm^{-1} in the $I^-(H_2O)$ cluster and are assigned to a combination band, bonded O-H stretch, and a free O-H stretch respectively. Absorptions in the iodide water dimer cluster at 3360 cm^{-1}, 3448 cm^{-1}, and 3696 cm^{-1} are assigned to a symmetric and an antisymmetric bonded O-H stretch, and a free O-H stretch respectively. *Ab initio* calculations at the MP2fc/6-311++G(d,p) level were used for the $I^-(H_2O)$ cluster to aid in spectral assignment and for geometrical information.

5.2 Introduction

Ion-solvent interactions are among the most basic interactions which are studied in physical chemistry, and have received considerable theoretical and experimental attention for most of this century. The hydrated halide clusters are model systems of solvation, and complement knowledge about systems involving cation solvation. These anions are isoelectronic with the noble gas atoms, and as one progresses through the halides the relative effects of covalent and electrostatic bonding on solvation (including the effects of polarizability and hydrogen bonding) are made evident. In this study vibrational spectra of the iodide anion water and water dimer clusters have been determined for the first time.

The method of pulsed electron beam high pressure mass spectrometry was applied by Kebarle and coworkers,[1] and later by Hiraoka and coworkers,[2] to the systems $X^-(H_2O)_n$ for X = F, Cl, Br, and I, where n ranges upward from 1 to a value of 5 to 10. Values for the stepwise enthalpy of hydration $\Delta H^\circ_{n-1,\,n}$ as measured by these groups are summarized in fig. 5.1. The value of $\Delta H^\circ_{n-1,\,n}$ for $F^-(H_2O)_n$ is seen to have a high initial value and falls off rapidly with increasing n. This is attributed to the formation of a semicovalent bond in $F^-(H_2O)$, that is, the partial formation of an adduct of the form $F^- \cdots H^+ \cdots OH^-$. Modeling performed by Hiraoka and coworkers at the SCF level, using a 3-21G+p basis set, shows a steady progression from a near linear X-H-OH for X = F to a C_{2v} structure for X = I, as shown in fig. 5.2. An analogous trend is seen in the halide water dimer clusters, in which $F^-(H_2O)_2$ and $Cl^-(H_2O)_2$ possess C_2 symmetry, while $Br^-(H_2O)_2$ and $I^-(H_2O)_2$ exhibit D_2 symmetry.

It is not obvious that small hydrated halide clusters $X^-(H_2O)_n$ for $n \sim 1$ to 20 will accurately reproduce bulk solvation structure around a central ion. Hydrated cation clusters appear to reproduce the classical structure in which a primary solvation shell of highly perturbed ligands is surrounded by weakly perturbed solvent molecules which can be accurately modeled as a dielectric continuum.[3] In the case of hydrated anions, however, there is the issue of the formation of surface states in finite sized clusters. In the surface state, the halide anion and a solvation shell of three to five water molecules reside on the periphery of a hydrogen-bonded network of water molecules. At 300 K it is believed that internal states are exclusively populated due to vibrational entropy.[4] However, in the cold clusters produced by a supersonic expansion, it is possible that the surface state isomers are dominant.

The question of surface versus interior states for the hydrated halide clusters $X^-(H_2O)_n$ has been raised by the work of Chesnovsky and coworkers.[5,6] The authors measured the vertical electron binding energies of the clusters $Cl^-(H_2O)_n$ for $n = 1$ to 7, $Br^-(H_2O)_n$ for $n = 1$ to 16, and $I^-(H_2O)_n$ for $n = 1$ to 60 using photoelectron spectroscopy. The photoelectron energy is directly influenced by the ion-solvent interaction potential, including solvent distance and orientation. For the iodide clusters, an abrupt decrease in E_{stab}, the stabilization energy or increase in ionization potential due to the addition of a single water molecule, is seen at $n = 7$. In the case of $n = 1$ to 6, E_{stab} averages 0.35 eV, while for $n \geq 7$, $E_{stab} < 0.07$ eV. The authors take this as an indication that the primary solvation shell of the anion comprises six ligands, but they note that the PES results for

Cl^- and Br^- (see fig. 5.3), as well as molecular dynamics simulations on I^-, do not necessarily support this theory.

Most molecular dynamics, *ab initio,* and Monte Carlo calculations which reproduce Chesnovsky and coworkers' values of E_{stab} indicate that the lowest energy configuration consists of surface solvated anions with coordination numbers of three to four. The work of Perera and Berkowitz indicates that unlike cations, anions are surface solvated in water clusters.[7] Monte Carlo calculations by Jorgenson and Severance concur, but indicate a coordination number of four to six instead of Perera and Berkowitz's three to four.[8] However, molecular dynamics simulations by Dang and Garrett on $I^-(H_2O)_n$ clusters for n = 1 to 15 do not reproduce Chesnovsky's break in E_{stab} at n = 6.[9] *Ab initio* calculations by Jortner and coworkers,[10] in addition to those of Caldwell and Kollman,[11] predict surface bound states for $X^-(H_2O)_n$ clusters for small values of n, with a transition to an interior structure at n = 4 or 5 for X = F, and at n = 6 for X = I. Despite considerable calculational effort, final conclusions regarding cluster structures are lacking. Models are found to be relatively insensitive to the specific location of I^- within the cluster, yet the surface solvated structures tend to reproduce the experimental results more frequently.

Vibrational predissociation spectroscopic studies have been performed by J.-H. Choi on the hydrated chloride anion clusters for n = 1 to 5.[12] In this work it was concluded that the anion tends to be located outside of a network of hydrogen bonded water molecules. It is important to note that the clusters possess sufficient vibrational energy to explore a significant portion of configuration space. Because these systems

involve many local minima, any of a number of structures, all within a few kcal/mol of the minimum energy, probably contribute to the observed spectrum.

Infrared predissociation spectroscopy of mass-selected cluster ions is a powerful technique for determining the structure of gas phase systems. Our group has applied this method to the systems SiH_7^+,[13] $NO_2^+(H_2O)_n$,[14] $NO^+(H_2O)_n$,[15] and $NO_2^+(HOX)$ (X = H, D, ^{35}Cl, ^{37}Cl).[12] The experiment detailed in the following section represents the first step towards directly addressing the question of the structure of the hydrated iodide anion clusters.

5.3 Experimental

The instrument has been described in chapter 4. A brief description will be given here which gives details specific to this experiment, in addition to a brief overview for reference. The iodide water clusters were generated by seeding methane carrier gas (99.9%, Matheson) with the vapor of both water (deionized water) and iodomethane (99%, Aldrich). Water (18 Torr vapor pressure) was placed in a glass bubbler, while iodomethane (350 Torr vapor pressure) was placed in a second opaque bubbler, both to avoid photodecomposition and because iodomethane is immiscible with water. The gas mixture at a stagnation pressure of 1600 Torr was expanded from a piezoelectric pulsed valve (nozzle dia 0.5 mm),[16] and ionized by a homemade electron gun with a beam energy of 750 eV.[17] The piezoelectric disk was coated with halocarbon grease (DuPont) to prevent chemical damage to the crystal element. The filament of the electron gun was

set to an emission current of 2 mA, of which ~170 μA typically reached the Faraday cup at the far side of the nozzle.

The high voltage extraction pulse of the time of flight mass spectrometer caused the clusters to separate into spatially discrete mass packets at the far end of the time-of-flight region. Precise electronic triggering (digital delay generators by EG&G PAR model 9650, and SRS model DG535 were used) resulted in the irradiation of one of these mass packets with infrared radiation (1 to 4 mJ/pulse). The radiation was produced by a Nd:YAG pumped lithium niobate optical parametric oscillator (OPO), tunable in the range 2600 to 6800 cm^{-1} with a resolution of 1.5 cm^{-1}.[18] The radiation excited vibrations of the water ligands in the clusters, causing the loss of one water molecule from the cluster through vibrational predissociation. After irradiation the clusters and cluster fragments entered a reflectron before reaching the microchannel plate detector. Spectra were recorded by measuring the photodissociation signal as a function of OPO wavelength. The OPO was calibrated using a monochromator and a photoacoustic cell, as detailed in chapter 4. The error in the OPO calibration is 10 cm^{-1} at most; relative peak spacings are limited by the resolution of the instrument, 1.5 cm^{-1}.

5.4 Results and Discussion

A typical mass spectrum of the hydrated anionic clusters $I^-(H_2O)_n$ can be seen in fig. 5.4. The conditions of the source could be changed to maximize large or small clusters, presumably by affecting the temperature of the beam. By maximizing gas throughput and by aligning the electron gun to intersect the expansion ~2 mm from the

nozzle, production of large clusters was optimized. These conditions were maintained for the duration of the experiment. Only one photodissociation channel was seen for each of the clusters studied, that being the loss of one water molecule upon absorption of the infrared photon.

Ab initio calculations were performed at the MP2fc/6-311++6(d,p) level on the $I^-(H_2O)$ molecule.[19] A summary of the geometry and energy of the lowest energy C_s configuration as well as the C_{2v} transition state is given in fig. 5.5. In fig. 5.6 the original and scaled harmonic vibrational frequencies, as well as drawings of the normal modes of the complex, are presented.

5.4.1 The Infrared Predissociation Spectrum of $I^-(H_2O)$

Figure 5.7 shows the raw and power normalized infrared predissociation spectra of the $I^-(H_2O)$ adduct. The spectrum was recorded from 3170 cm^{-1} to 3800 cm^{-1}. Starting with the red end of the spectrum, a small peak is observed at 3294 cm^{-1}. The analogous peak in the $Cl^-(H_2O)$ spectrum lies at 3290 cm^{-1}. The peak is tentatively assigned to a combination band arising from a complex excited in the H_2O rocking mode (predicted to be 174 cm^{-1}), going to a complex excited in the bound OH mode. *Ab initio* vibrational frequencies are given in fig. 5.6. A broad, intense peak is observed at 3417 cm^{-1}, and is assigned as the bonded OH stretch of the C_s structure. The symmetric and antisymmetric bending frequencies of free water are 3657 cm^{-1} and 3756 cm^{-1} respectively, and this hydrogen bonded mode may be considered to be a perturbed combination of the modes of the free molecule. Theory predicts this vibration to lie at 3524 cm^{-1} (scaled). A third

weaker peak is observed at 3710 cm^{-1} and is assigned as the free OH stretch of the H_2O ligand. The scaled *ab initio* frequency of this vibration is 3702 cm^{-1}. As detailed in fig. 5.6, this mode is expected to be roughly 10% as intense as the bound OH stretch. The relative intensities of these peaks are preserved in the spectrum we recorded. It is interesting to note that the analogous vibration in $Cl^-(H_2O)$ was not observed. This was explained by *ab initio* calculations which predict an absorption intensity only 3% as large as that of the bound OH stretch. All of the absorptions lead to the $I^- + H_2O$ product channel, suggesting that the species is an ion-molecule complex with strong hydrogen bonding. The scaled vibrational frequencies for the symmetric and antisymmetric stretching modes of the C_{2v} complex are 3615 cm^{-1} and 3669 cm^{-1} respectively (fig. 5.6). Because no bands were observed in this region, the case for a C_s complex, rather than a C_{2v} complex, is strengthened.

To sum, the infrared predissociation spectrum of the $I^-(H_2O)$ spectrum is consistent with the C_s structure calculated by *ab initio* methods and presented in fig. 5.5. The asymmetric complex has one hydrogen at a distance of 2.8 Ångstroms from the iodide anion, and the other at a distance of 3.5 Ångstroms. There is predicted to be a small (0.4 kcal/mol at 0 K) barrier to interconversion of free and bound hydrogens due to rotation of the water molecule. Given the temperature of the complex, it is therefore expected that the full range of possible geometries will be explored.

5.4.1 The Infrared Predissociation Spectrum of $I^-(H_2O)_2$

The spectra which were obtained for the iodide anion water dimer complex are presented in fig. 5.8. Both raw and power normalized data are presented. The bonded OH stretch for $I^-(H_2O)$ was seen at 3417 cm^{-1}. When a second water molecule is added to the complex, the two bonded OH stretches form symmetric and antisymmetric combinations. The presence of two absorptions in this region of the spectrum is strong evidence that the dimer cluster contains two hydrogen bonded water ligands. The lower frequency vibration, observed at 3360 cm^{-1}, is the symmetric vibration, while the higher frequency peak at 3448 cm^{-1} is the antisymmetric mode. In addition a peak due to the free OH stretch is seen at 3696 cm^{-1}. The same mode is observed for the cluster $Cl^-(H_2O)_2$ at a frequency of 3698 cm^{-1}. In addition, a possible fourth band is observed at 3630 cm^{-1} which may be due to the formation of a hydrogen bond between the two water molecules.

The motion of the two water ligands is expected to be floppy, in analogy to both the $Cl^-(H_2O)_n$ complexes and the $I^-(H_2O)$ complex. In this way the geometry pictured in fig. 5.2 (Hiraoka *et al.* 1988) is consistent with the observed peaks, with the caveat that due to the flat nature of the potential, it is possible that both water molecules will be on the same side of the iodide anion and will form a hydrogen bond.

5.5 Conclusion

The first observation of the infrared predissociation spectra of the iodide water and water dimer spectra has been made. The spectra indicate that both clusters have free

and hydrogen-bound OH stretches, implying an asymmetric geometry for the water ligand. In addition there is weak evidence of the formation of a hydrogen bond between the two water ligands in the dimer cluster. Further studies are planned to increase the signal to noise ratio of the spectra presented here, and to extend the study to larger cluster sizes.

5.6 References

[1] M. Arshadi, R. Yamdagni, and P. Kebarle, *J. Phys. Chem.* **74**(7), 1475 (1970).

[2] K. Hiraoka, S. Mizuse, and S. Yamabe, *J. Phys. Chem.* **92**(13), 3943 (1988).

[3] J. Bockris and A. K. N. Reddy, *Modern Electrochemistry*, Plenum, New York (1970).

[4] T. Asada, K. Nishimoto, and K. Kitaura, *J. Phys. Chem.* **97**(29), 7724 (1993).

[5] G. Markovich, S. Pollack, R. Giniger, and O. Chesnovsky, *J. Chem. Phys.* **101**(11), 9344 (1994).

[6] G. Markivich, S. Pollack, R. Giniger, and O. Chesnovsky, *Reaction Dynamics in Clusters and Condensed Phases*, Ed. by J. Jortner, R. D. Levine, and B. Pullman, Kluwer Academic, Dortrecht (1994).

[7] L. Perera and M. L. Berkowitz, *J. Chem. Phys.* **96**, 8288 (1992).

[8] W. L. Jorgensen and D. L. Severance, *J. Chem. Phys.* **99**, 4233 (1993).

[9] L. X. Dang and B. C. Garrett, *J. Chem. Phys.* **99**, 2972 (1993).

[10] J. E. Combariza, N. R. Kestner, and J. Jortner, *Chem. Phys. Lett.* **203**, 423 (1993). J. E. Combariza, N. R. Kestner, and J. Jortner, *J. Chem. Phys.* **100**, 2851 (1994). J. E. Combariza, N. R. Kestner, and J. Jortner, *Chem. Phys. Lett.* **221**, 156 (1994).

[11] J. W. Caldwell and P. A. Kollman, *J. Phys. Chem.* **96**, 8249 (1992).

[12] J.-H. Choi, Ph.D. Thesis, California Institute of Technology (1995).

[13] Y.-B. Cao, J.-H. Choi, B.-M. Haas, M. S. Johnson, and M. Okumura, *J. Phys. Chem.* **97**, 5215 (1993).

[14] Y.-B. Cao, J.-H. Choi, B.-M. Haas, M. S. Johnson, and M. Okumura, *J. Chem. Phys.* **99**, 9307 (1993). Y.-B. Cao, J.-H. Choi, B.-M. Haas, and M. Okumura, *J. Phys. Chem.* **98**, 12176 (1994).

[15] J.-H. Choi, K. T. Kuwata, B.-M. Haas, Y.-B. Cao, M. S. Johnson, and M. Okumura, *J. Chem. Phys.* **100**, 7153 (1994).

[16] D. Proch and T. Trikl, *Rev. Sci. Instrum.* **60**(4), 713 (1989).

[17] P. W. Erdman and E. C. Zipf, *Rev. Sci. Instrum.* **53**, 225 (1982).

[18] T. K. Minton, S. A. Reid, H. L. Kim, and J. D. McDonald, *Optics Comm.* **69**, 289 (1989). S. J. Brosnan and R. L. Byer, *IEEE J. Quant. Elect.* **15**, 415 (1979).

[19] Gaussian 92, Revision D.2, M. J. Frisch, G. W. Trucks, M. Head-Gordon, P. M. W. Gill, M. W. Wong, J. B. Foresman, B. G. Johnson, H. B. Schlegel, M. A. Robb, E. S. Replogle, R. Gomperts, J. L. Andres, K. Raghavachari, J. S. Binkley, C. Gonzalez, R. L. Martin, D. J. Fox, D. J. Defrees, J. Baker, J. J. P. Stewart, and J. A. Pople, Gaussian, Inc., Pittsburgh, PA (1992).

(*a*)

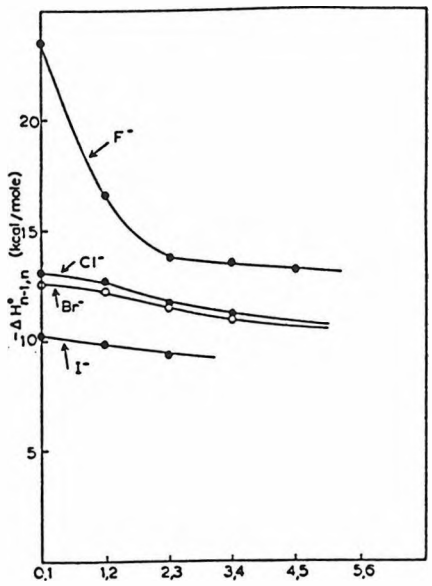

(*b*)

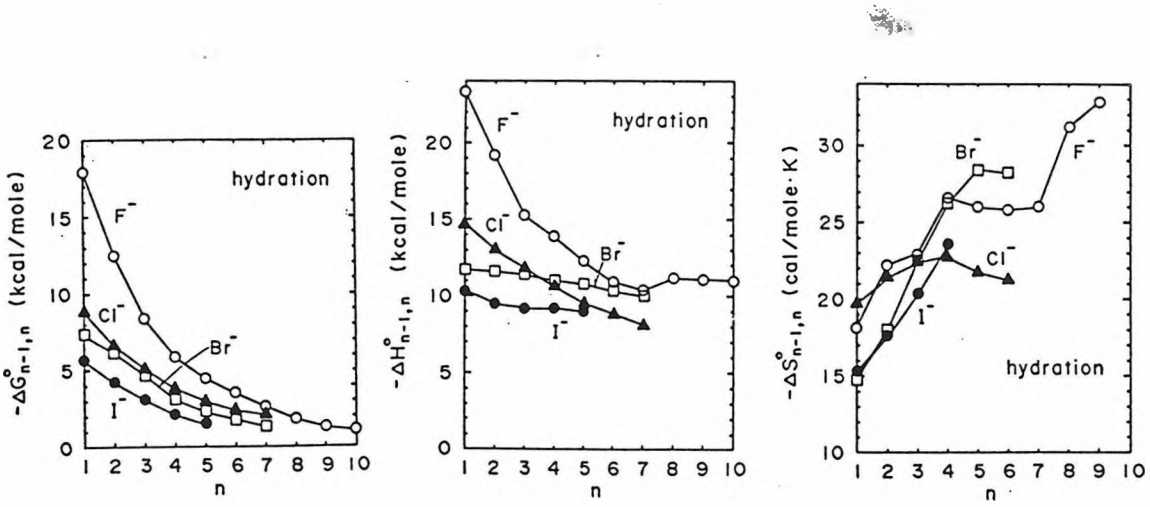

Figure 5.1 (*a*) The *n* dependence of $-\Delta G^{\circ}_{n-1,n}$, $-\Delta H^{\circ}_{n-1,n}$, and $-\Delta S^{\circ}_{n-1,n}$ of the halide hydration reactions $X^-(H_2O)_{n-1} + H_2O \Leftrightarrow X^-(H_2O)_n$ for X = F, Cl, Br, and I. Hiraoka *et al.* (1988). (*b*) $-\Delta H^{\circ}_{n-1,n}$ for halide ion hydration. Kebarle and coworkers (1970).

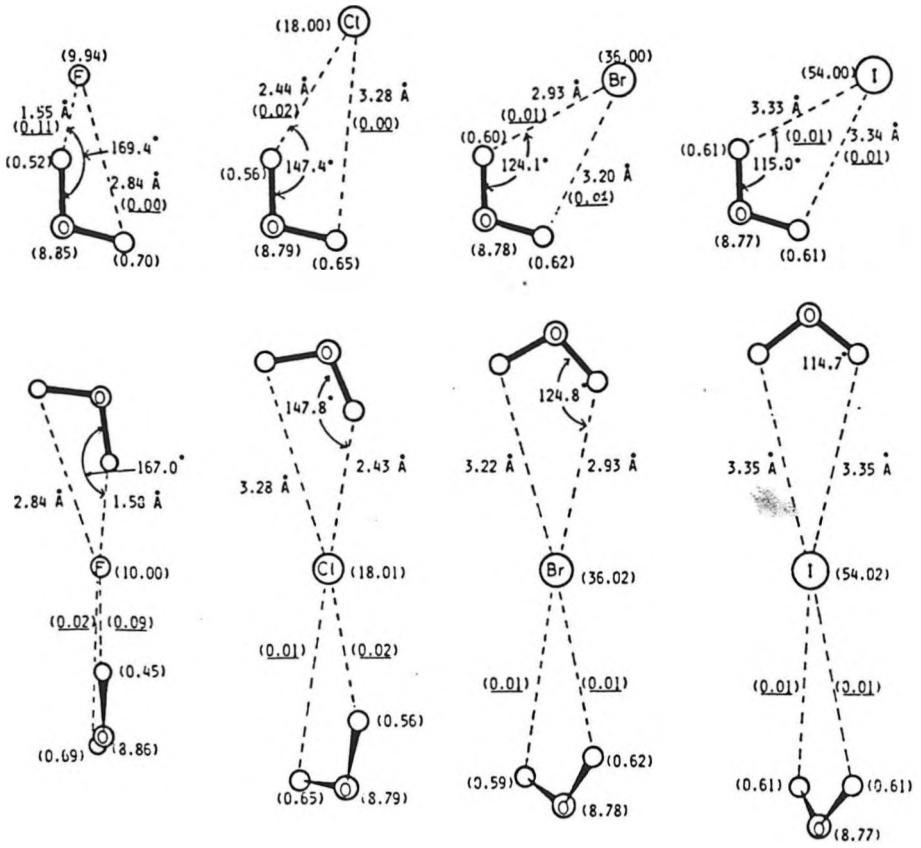

Figure 5.2 SCF geometries (3-21G+p) of $X^-(H_2O)$ and $X^-(H_2O)_2$ for X = F, Cl, Br, and I. The values in parenthesis are Mullikan atom populations, with underlined values representing atom-atom bonding populations. Hiraoka *et al.* (1988).

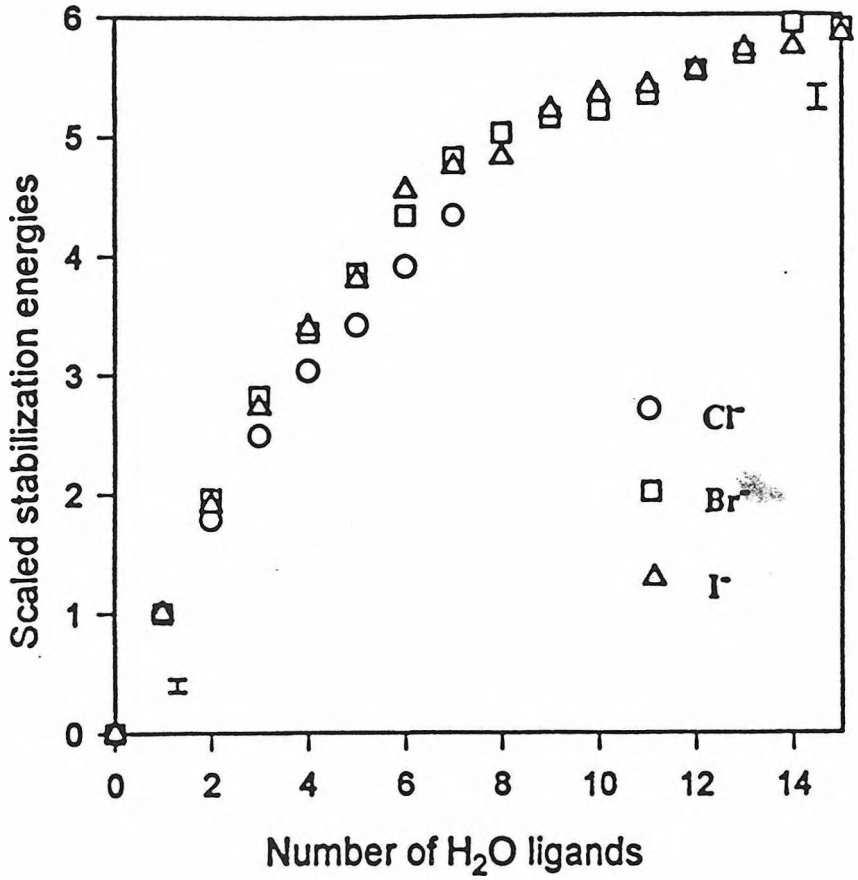

Figure 5.3 Stabilization energies for the hydrated halide ion clusters $X^-(H_2O)_n$ for X = Cl, Br, and I, normalized to the anion-single water molecule stabilization energy, $[BE_v(n) - EA]/[BE_v(1) - EA]$. Error bars for the n = 1 and n = 15 clusters are given. Photoelectron spectroscopy results due to Chesnovsky and coworkers (1994).

(*a*)

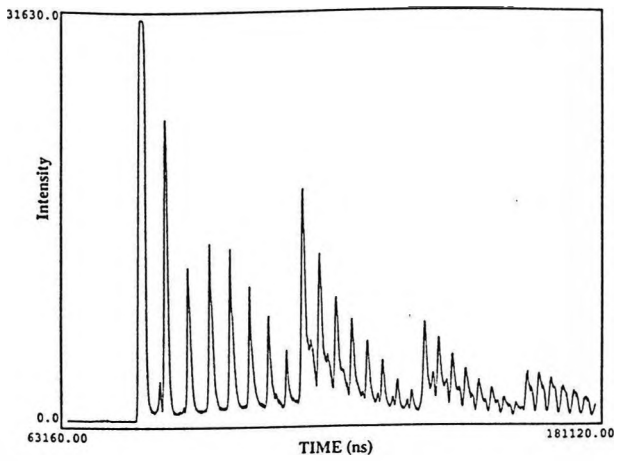

(*b*)

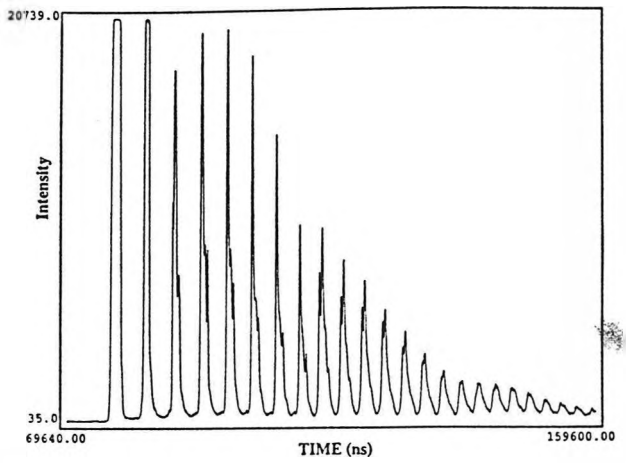

(*c*)

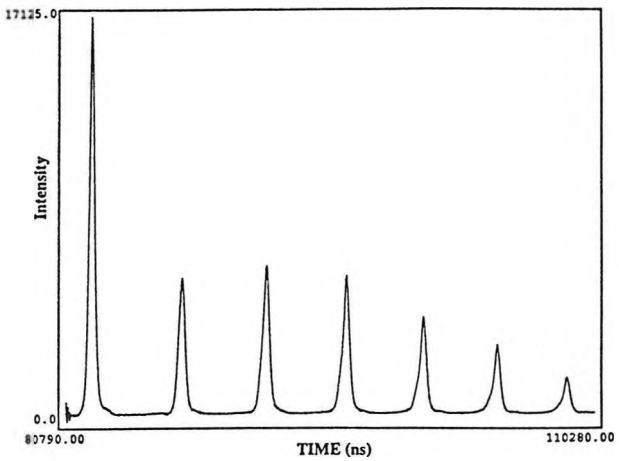

Figure 5.4 Mass spectra of the ion distribution produced by the source used in this experiment. CH_3I and H_2O vapor were seeded into CH_4 carrier gas, pulsed through a piezoelectric valve and 0.5 mm nozzle, and ionized by a 750 eV electron beam before entering the time-of-flight mass spectrometer. Experimental conditions were optimized for the production of large clusters. (*a*) Distribution showing $I_m^-(H_2O)_n$ clusters for m = 1 to 4 and n = 1 to ~7. (*b*) Distribution showing $I^-(H_2O)_n$ clusters for n = 1 to 22. (*c*) $I^-(H_2O)_n$ clusters are shown with a peak intensity for $I^-(H_2O)_2$.

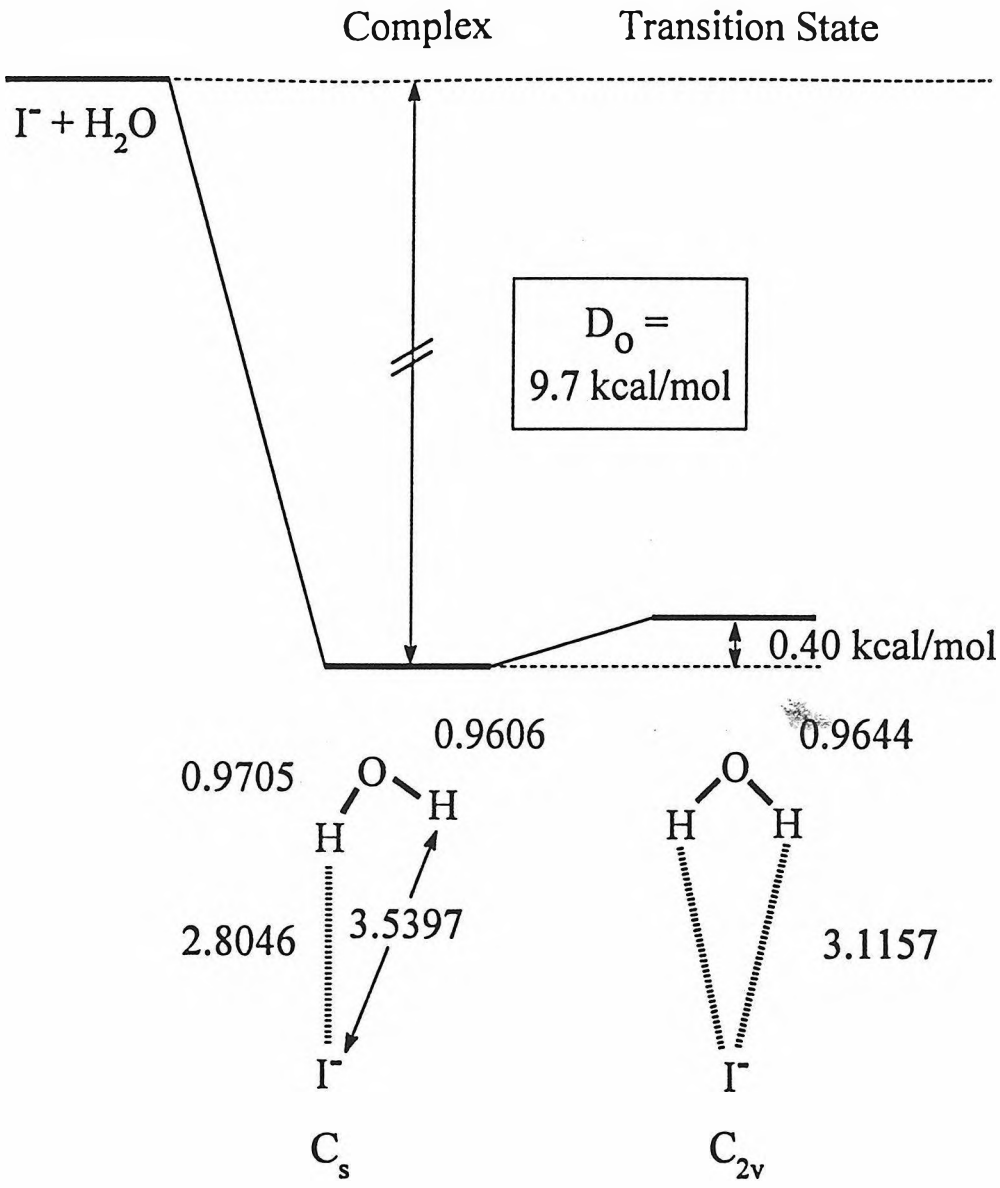

Figure 5.5 *Ab initio* structures and energies of the C_s and C_{2v} (transition state) complexes of I- with H_2O. Calculations were performed at the MP2fc/6-311++G(d,p) level.

	Vibration Number	Unscaled Frequency (cm^{-1})	Scaled Frequency (cm^{-1})	IR Intensity (km/mol)
C_s	ν_1	111	---	3
	ν_2	174	---	78
	ν_3	561	---	113
	ν_4	1694	---	192
	ν_5	3749	3524	358
	ν_6	3938	3702	42
C_{2v}	ν_5	3846	---	94
	ν_6	3903	---	33

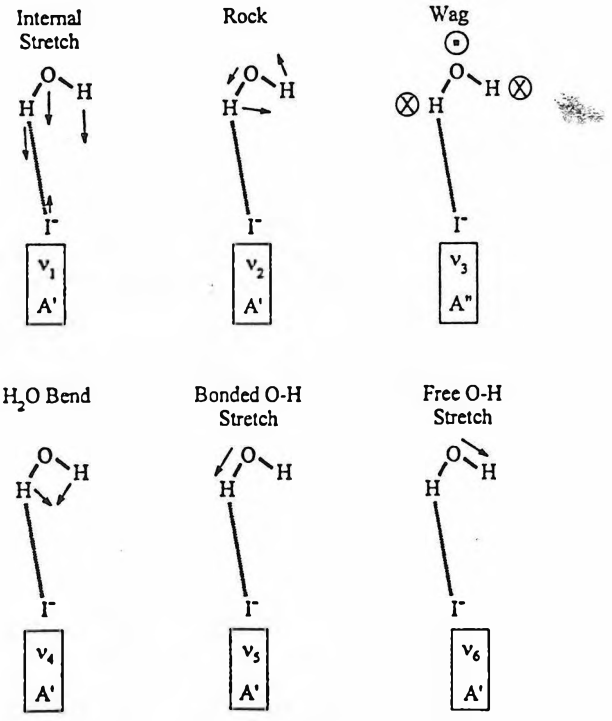

Figure 5.6 Vibrational frequencies for the I-(H2O) complex as determined by *ab initio* calculations at the MP2fc/6-311++G(d,p) level. A scaling factor of 0.94 was employed. Normal modes of the C_s structure are indicated.

(*a*) Infrared spectra of $I^-(H_2O)$. Raw data, 3170 cm^{-1} to 3460 cm^{-1}.

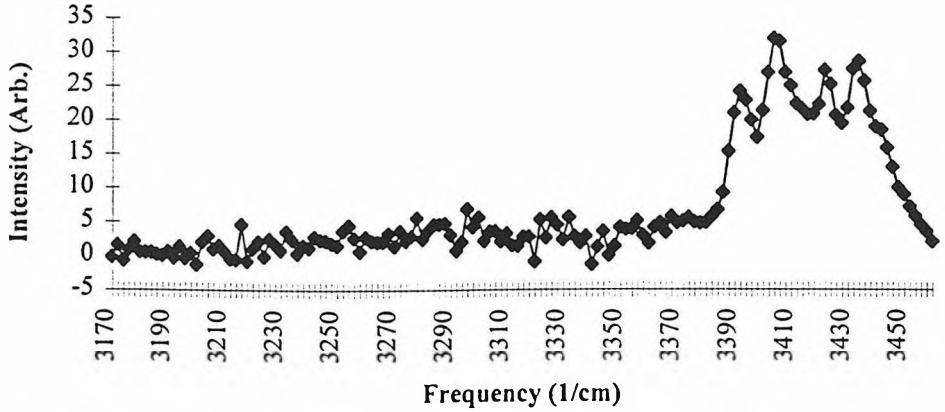

(*b*) Infrared spectra of $I^-(H_2O)$. Raw data, 3530 cm^{-1} to 3800 cm^{-1}.

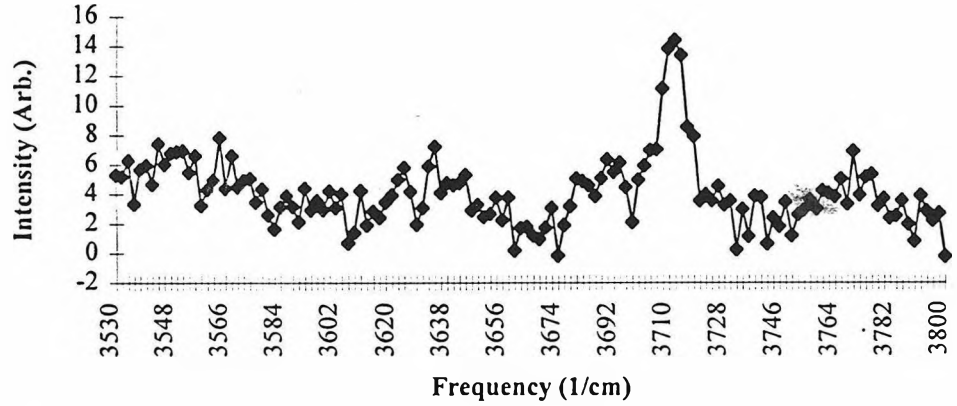

(*c*) Infrared spectra of $I^-(H_2O)$. Raw data, 3170 cm^{-1} to 3800 cm^{-1}.

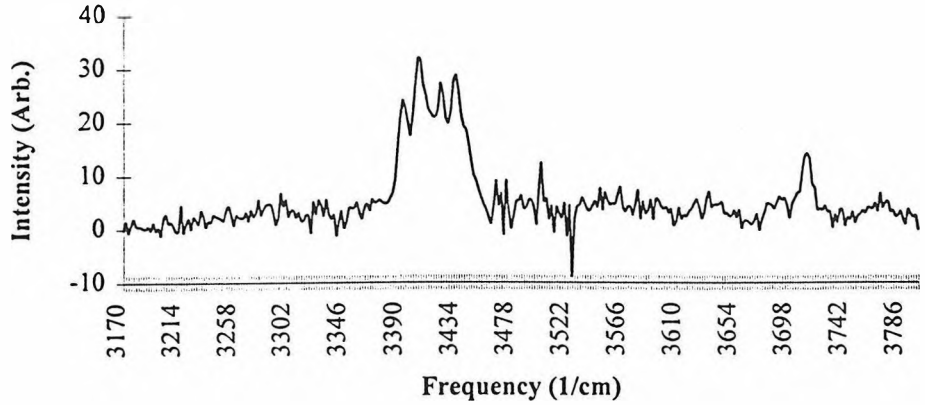

(*d*) Infrared spectra of $I^-(H_2O)$. Power normalized data, 3170 cm^{-1} to 3460 cm^{-1}.

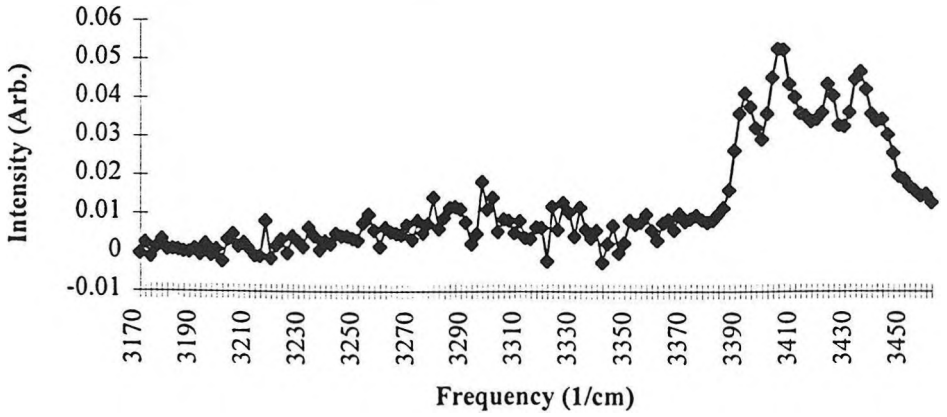

(*e*) Infrared spectra of $I^-(H_2O)$. Power normalized data, 3530 cm^{-1} to 3800 cm^{-1}.

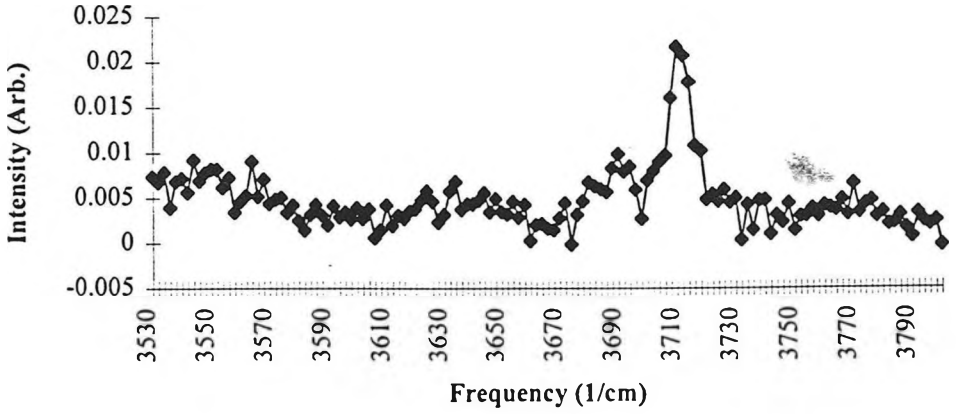

(*f*) Infrared spectra of $I^-(H_2O)$. Power normalized data, 3170 cm^{-1} to 3800 cm^{-1}.

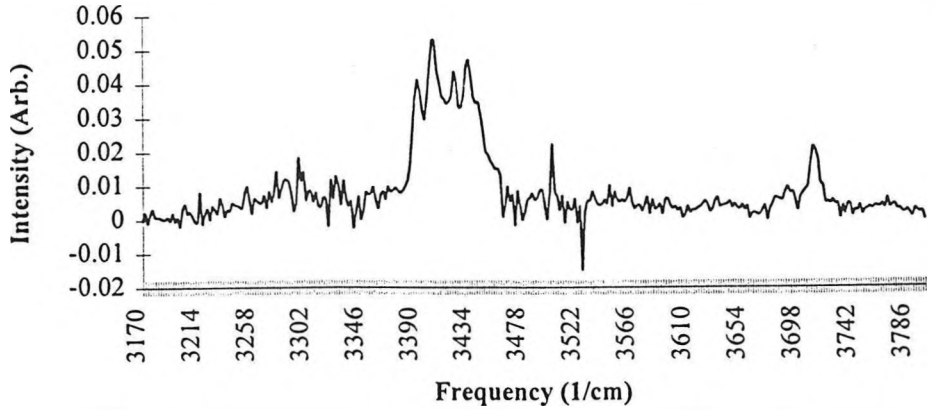

Figure 5.7 Infrared vibrational predissociation spectra of the $I^-(H_2O)$ complex.

(*a*) Infrared spectra of $I^-(H_2O)_2$. Raw data, 3100 cm^{-1} to 3470 cm^{-1}.

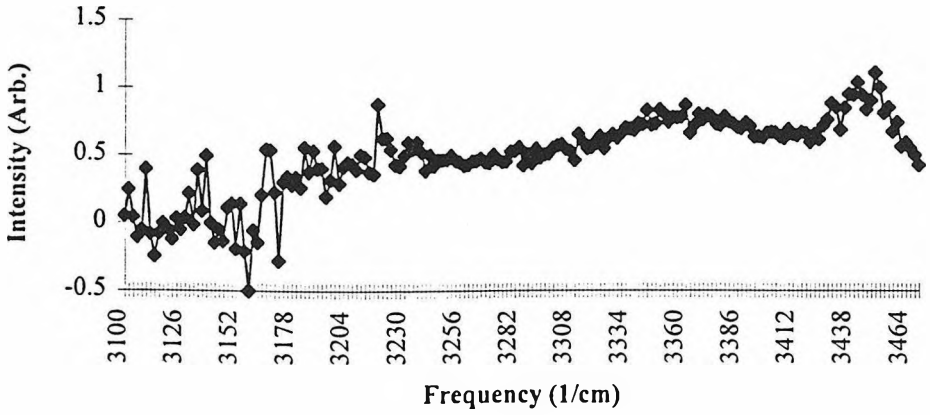

(*b*) Infrared spectra of $I^-(H_2O)_2$. Raw data, 3540 cm^{-1} to 3800 cm^{-1}.

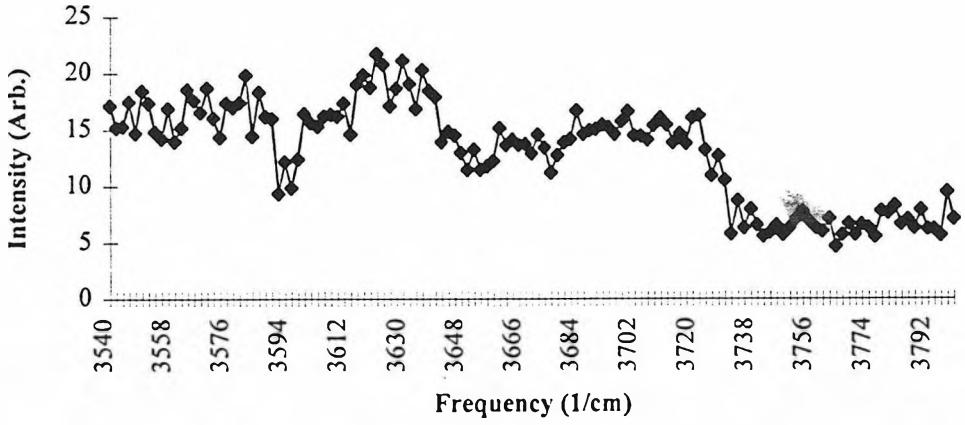

(*c*) Infrared spectra of $I^-(H_2O)_2$. Raw data, 3100 cm^{-1} to 3800 cm^{-1}.

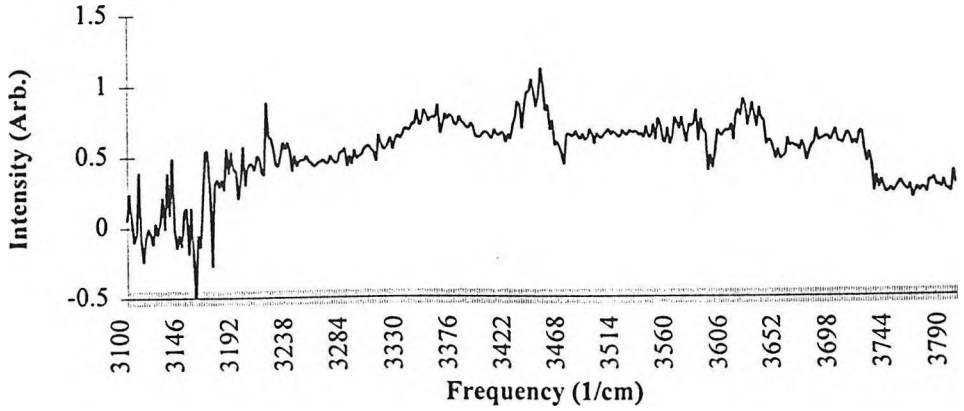

(*d*) Infrared spectra of $I^-(H_2O)_2$. Power normalized data, 3100 cm^{-1} to 3470 cm^{-1}.

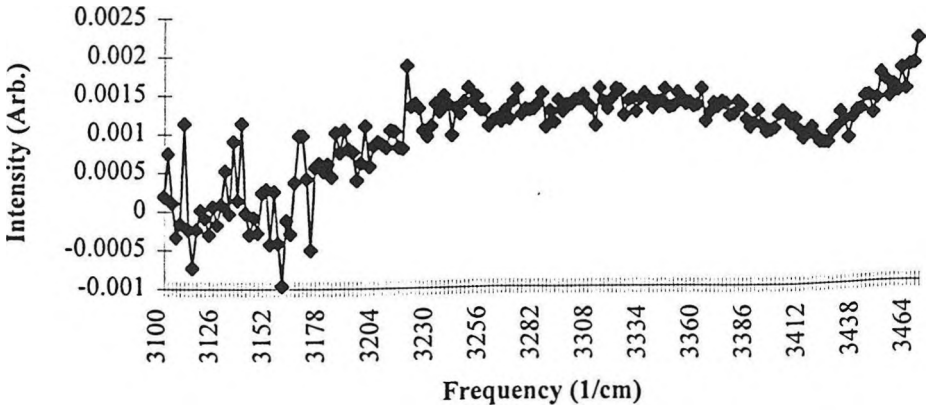

(*e*) Infrared spectra of $I^-(H_2O)_2$. Power normalized data, 3540 cm^{-1} to 3800 cm^{-1}.

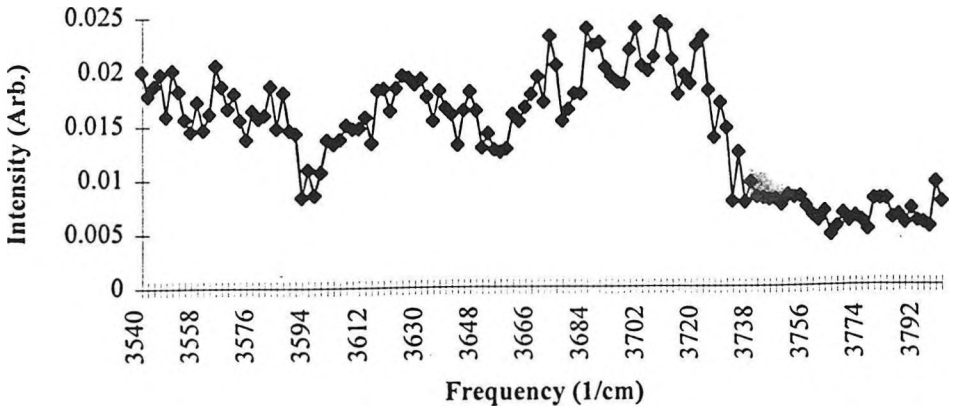

Figure 5.7 Infrared vibrational predissociation spectra of the $I^-(H_2O)_2$ complex.

Chapter 6:

Photoelectron Spectroscopy of Chlorine Nitrate

6.1 Abstract

The He(I) photoelectron spectrum of chlorine nitrate has been measured. State of the art *ab initio* calculations have been performed to aid in the assignment of the spectra. The spectrum of the valence electrons consists of a series of eight peaks with vertical ionization energies of 11.66, 12.25, 12.94, 13.10, 13.86, 14.87, 16.22 and 18.77 eV. In addition, the first determination of the ionization potential of $ClONO_2$ has been made. Its value is 10.86 ± 0.05 eV. The HOMO of the molecule is determined to be predominantly a nonbonding chlorine orbital with a contribution from the $\pi^*_{Cl\,O}$ orbital. The identity of the molecular orbitals is important in light of recent work concerning the UV photolysis branching ratio of $ClONO_2$ and its impact on stratospheric ozone concentrations.[1] Recent *ab initio* calculations by Graña[2] *et al.* conclude that because of a small oscillator strength, the HOMO does not make a significant contribution to the UV absorption spectrum.

6.2 Introduction: The atmospheric role of $ClONO_2$

Interest in chlorine nitrate ($ClONO_2$) centers on its role as a relatively inert reservoir for ClO_x and NO_x in the earth's stratosphere. $ClONO_2$ accounts for 10% to 20% of atmospheric NO_x, and 30% to 60% of an atmospheric chlorine budget that largely is attributable to stable source gases (*e.g.*, CFC's).[3] The dynamic control of O_3 by chlorine is regulated in the stratosphere because most of the chlorine is sequestered in less-reactive reservoir species including HCl and $ClONO_2$. If this chlorine were to be liberated, catastrophic O_3 loss could result. In fact, the Antarctic ozone hole arises in part because much of the reservoir has been transformed to reactive chlorine. By examining the records of the British Antarctic Survey dating to 1957, Farman *et al.* in 1985 discovered a springtime depletion of ozone in the vortex of air over the South Pole.[4] Daily mean values of total column ozone dropped from values of greater than 300 Dobson Units (DU) before 1968 to under 200 in 1984. In 1991 the value had dropped to under 150 DU.[5] Although it was proposed that the decline was linked to the low temperatures of the stratosphere and the return of sunlight in the spring, models of the stratosphere could not account for the depletion.

Studies by Anderson *et al.* established the link between the 'ozone hole' and chlorine.[6] The solution to correctly modeling polar ozone depletion lay in heterogeneous reactions occurring on the surface of polar stratospheric clouds (PSCs) that converted the reservoirs into Cl_2 and HOCl, molecules which are easily photolyzed by sunlight:[7]

$$ClONO_2 + HCl \rightarrow Cl_2 + HNO_3 \quad (1)$$

$$ClONO_2 + H_2O \rightarrow HOCl + HNO_3 \quad (2)$$

$$HOCl + HCl \rightarrow Cl_2 + H_2O \quad (3)$$

Reactions 1 and 3 can be catalyzed by nitric acid trihydrate (NAT or type I PSCs), and all three of these reactions are catalyzed by water ice (type II) PSCs.[8] Type I PSCs form at temperatures at or below 196 K, while type II PSCs will form at or below 188 K. In the Antarctic winter, the atmosphere is cold and dark. Because it is cold, PSCs form and process chlorine compounds into photolabile species. These molecules accumulate in the dark and release their chlorine when the sun comes out in the springtime. This leads to higher than normal atomic chlorine concentrations in the atmosphere, and a near total depletion of ozone at some altitudes. In fig. 6.1, normal stratospheric chlorine chemistry is summarized and contrasted to the perturbed chemistry of the Antarctic spring.

In computer models of the atmosphere it is important to know not only reaction rates, but also photolysis cross sections and product branching ratios. The energetics of the photodissociation channels of $ClONO_2$ are as follows:

$$ClONO_2 + h\nu \rightarrow ClO + NO_2 \quad (26.6 \text{ kcal/mol}) \quad (4)$$

$$\rightarrow Cl + NO_3 \quad (40 \text{ kcal/mol}) \quad (5)$$

$$\rightarrow ClONO + O \quad (67 \text{ kcal/mol}) \quad (6)$$

Early studies had concluded that $ClONO_2$ exhibits a 90% yield in the $Cl + NO_3$ channel (5). It was further noted that $ClONO_2$ photolysis had a 10% ± 10% yield in channel (6) and no yield in channel (4).[9] This is interesting since (4) corresponds to fission of the weakest bond in the molecule. The dominance of (5) over (4) was

attributed to an $n \rightarrow \sigma^*$ transition localized on the ClO chromophore of $ClONO_2$, and it was guessed that ClOOCl would behave in a similar manner.

The following mechanism is believed to account for approximately 70% of the catalytic O_3 destruction in the Antarctic polar vortex:[9,10]

$$ClO + ClO + M \rightarrow ClOOCl + M \quad (7)$$

$$ClOOCl + h\nu \rightarrow ClOO + Cl \quad (8)$$

$$ClOO + M \rightarrow Cl + O_2 + M \quad (9)$$

$$2(Cl + O_3 \rightarrow ClO + O_2) \quad (10)$$

$$\text{Net: } 2O_3 \rightarrow 3O_2 \quad (11)$$

Step 8 in this cycle depends on the preferential cleavage of the Cl-O bond over the weaker O-O bond. Energetically, this is not a straightforward assumption:[11]

$$ClOOCl + h\nu \rightarrow ClO + ClO \quad (18 \text{ kcal/mol}) \quad (12)$$

$$\rightarrow ClOO + Cl \quad (21 \text{ kcal/mol}) \quad (13)$$

Reaction 13 was thought to take place with 100% yield based on a single experiment which detected only Cl atoms.[12] However, recent crossed molecular beam studies of the photodissociation of $ClONO_2$ at 308, 248 and 193 nm indicate that the ClO + NO_2 channel (4) can account for up to about half of the products.[1,13] An understanding of the molecular orbitals of $ClONO_2$ based on photoelectron spectroscopy may help in understanding whether nonbonding electrons on the Cl atom of the ClO chromophore participate in a $n \rightarrow \sigma^*$ transition.

Ultraviolet photoelectron spectroscopy is a valuable tool for learning about the molecular orbitals of a molecule, especially when used in combination with *ab initio*

calculations. Given recent discoveries regarding the earth's ozone layer and especially the perturbed chemistry of the polar stratosphere, this work is a timely addition to our knowledge of $ClONO_2$. More specifically, photoelectron spectroscopy provides a deeper understanding of the electronic absorption spectra of $ClONO_2$, and indirectly provides a model for the photodissociation behavior of that molecule and of hydroperoxy chloride (ClOOCl).

6.3 Experimental

This experiment was conducted on the photoelectron spectrometer used by the undergraduate physical chemistry laboratory at Caltech. The spectrometer was rebuilt for this study to the extent that a computer and interface boards were configured to operate the machine.

6.3.1 The UPS Apparatus

A schematic diagram of the apparatus is shown in fig. 6.2. Ionizing He(I) α radiation (21.22 eV, 58.4 nm) was created by passing UHP He (Matheson) through a liquid nitrogen trap and flowing the dried gas through a quartz glass McCarroll cavity excited at 2450 MHz by a 200 W Burdick diathermy power supply. The lamp was passed through a 1 mm inner diameter quartz capillary which collimated the light before it reached the interaction region. The lamp was adjusted so the He(I) β line accounted for less than 1% of the emission. The chamber was pumped by a 2" diameter liquid nitrogen-baffled diffusion pump. After the radiation ionized the sample, the

photoelectrons traveled through a 2" diameter hemispherical energy analyzer.[14] Surfaces were coated with Aquadag to prevent secondary electron scattering. The electrons were detected by a Galileo Channeltron (Model CEM 4039), and the signal capacitively coupled to conditioning electronics. A pulse amplifier and discriminator allowed electron counts to be recorded by a Keithley-Metrabyte MCN-8 scalar attached to an AT personal computer. The bias on the energy analyzer was controlled by a Keithley-Metrabyte DAC-02 digital to analog converter. The program PES was written in Turbo Pascal to control the scalar and D/A boards. A listing of the program may be found in Appendix B.

6.3.2 Experimental Procedure

$ClONO_2$ was prepared according to the method of Schmeisser.[15] The sample was kept at 199 K by an ETS Systems Multi-Cool chiller (Model MC-4-80A-1), and was transferred to the PES inlet valve by a system composed of Teflon and glass tubing joined by Teflon fittings. Sample pressure in the ionizing chamber was regulated by a stainless steel leak valve (Nupro). The pressure in this line was typically 800 mTorr and occasionally as low as 200 mTorr. Pressure in the main chamber of the PES was typically 2.5×10^{-5} Torr. Degradation of the electron multiplier response over time was noted, presumably due to exposure to $ClONO_2$. This could be corrected to some extent by increasing the detector voltage, but ultimately the Channeltron had to be replaced.

The infrared[16] and ultraviolet[17] spectra of the chlorine nitrate samples were recorded in order to assess the purity of the sample. The sample was stored under liquid

nitrogen and redistilled periodically to ensure purity. The inlet line was passivated by the action of chlorine nitrate passing through it over a period of months. Data runs used to compile the final spectrum (fig. 6.3*d*) were taken only in the last few days of that time period, when the line was thoroughly passivated. In a study of the reaction of chloride ions with chlorine nitrate by ICR,[18] a passivated stainless steel source line resulted in the formation of at most 5% Cl_2 in the sample. In contrast, no Cl_2 formed in a glass and Teflon line. In this work the majority of the flow system was Teflon or glass, with the exception of a passivated stainless steel leak valve. Early scans (Figures 6.3*a* and 6.3*b*) clearly show peaks due to chlorine contamination.

6.4 Results

The chlorine nitrate photoelectron spectrum is shown in fig. 6.3. Eight peaks were found at 11.66, 12.25, 12.94, 13.10, 13.86, 14.87, 16.22 and 18.77 eV. In addition the first determination of the ionization potential of the molecule was made. The ionization potential, previously unknown, was measured to be 10.86 eV. The resolution of the instrument is 0.045 eV.

The scans were calibrated by admitting a small amount of argon through a needle valve into the sample chamber. The argon atomic photoelectron spectra consists of two peaks, $^2P_{3/2}$ at 15.759 eV and $^2P_{1/2}$ at 15.937 eV. In addition, the same results were obtained when the spectra was calibrated with N_2 (fig. 6.3*a*).

6.5 Discussion

6.5.1 Interpreting Photoelectron Spectra

In photoelectron spectroscopy an electron is ejected from the molecule by an energetic photon. It is the molecular version of the photoelectric effect discovered by Einstein in 1905,[19] as expressed in the equation:

$$h\nu = (1/2)m_e v^2 + \Phi$$

Because of conservation of the energy of the incident photon, the kinetic energy of the electron, $(1/2)m_e v^2$, is equal to the photon energy minus the work function of the material Φ. In the case of an individual molecule, the energy of the incident photon is conserved as the kinetic energy of the ejected electron plus the energy of the cation left behind. The cation's energy does not include relaxation processes such as secondary emission of light. Thus it can be seen that the kinetic energy of the electron contains information relating to the electronic and vibrational state of the ion. In 1934 Koopmans proposed that this energy approximated the energy of the molecular orbitals in the neutral molecule. The theory states that for a closed shell molecule the vertical ionization energy of an electron in a particular orbital (I_i) is approximately equal to the negative of the orbital energy calculated by the self-consistent field (SCF) method ($-\varepsilon_i^{SCF}$):[20]

$$I_i \approx -\varepsilon_i^{SCF}$$

Koopmans' theorem allows one to take a look inside the molecule. Since direct observation of $-\varepsilon_i^{SCF}$ is possible, the method vividly illustrates the molecular orbital as linear combination of atomic orbital concepts taught in introductory chemistry courses.[21]

Koopmans' theorem is only a zeroth order approximation. The energies and wavefunctions of the cation are not the same as those of the neutral species:

$$\varepsilon_i^{SCF}(M+) \neq \varepsilon_i^{SCF}(M)$$

The eigenstates reorganize in response to the missing electron. In addition, SCF calculations do not include electron correlation. In the present work, electron correlation is taken into account by *ab initio* methods such as the Møller-Plesset[22] and coupled cluster methods.[23]

Empirical formulas have been devised to overcome the limitations of Koopmans' theorem in an effort to increase knowledge of the neutral molecule's orbital energies:[24]

$$I_i = -0.92\ \varepsilon_j$$

$$I_i = 2.5 - 0.8\ \varepsilon_j$$

As seen in fig. 6.4, calculated and experimental orbital energies typically differ by ±1 eV. The experimental vertical ionization energies thus must be separated by about 2 eV in order to be sure that a given theory-based orbital assignment is valid. As can be seen in table 6.1, this unfortunately is not the case for $ClONO_2$. For differences less than 1 eV, the ordering of orbitals can occasionally be reversed. For example SCF calculations give the wrong ordering for the first two orbitals of N_2.[24] As another example of the tenuous nature of assignments based on Koopmans' theorem, the average error of theoretical orbital energies (as compared to experimental values) in Cl_2O based on SCF calculations is 1.45 eV, with a standard deviation of 0.79 eV.[25] Thus it would not be wise to base an assignment solely on closed shell *ab initio* calculations. Often confirmation of an assignment can be made by looking at the bands of similar molecules. In addition, the techniques of angle-resolved PES [26] and electron correlation calculations on the open shell cation could be used to test a given assignment.

6.5.2 The Photoelectron Spectrum of Chlorine Nitrate

Ab initio calculations were performed on $ClONO_2$ in order to aid in the assignment of the spectrum (see table 6.2). The geometry of $ClONO_2$ and convention used for labeling the oxygen atoms is presented in fig. 6.5.[27] In addition an effort was made to interpret the data in terms of the HOCl,[28] Cl_2O[29] and HNO_3[30] photoelectron spectra to test the hypothesis that the ClO and NO_2 chromophores on $ClONO_2$ would behave independently (see table 6.4). A peak by peak discussion of the assignment follows.

The threshold region of the photoelectron spectra of $ClONO_2$ and HOCl resemble each other, especially in the energy and identity of the first two peaks. The vertical ionization potential of the HOMO of HOCl is 11.22 eV, and of the second orbital 12.27 eV, while the corresponding potentials in $ClONO_2$ are 11.66 eV and 12.25 eV. Colbourne *et al.*[28] have assigned the HOMO of HOCl to an A" $\pi^*_{Cl\ O1}$ occupation, which is similar to the occupation of the HOMO of $ClONO_2$ as given by *ab initio* calculations. Calculations show a 65% occupancy in Cl p_z orbitals, and 18% on O1 p_z orbitals. Similarly the second band of HOCl is given an assignment of A' $n_{Cl} + (\pi^*_{Cl\ O1})$, which is similar to the CCSD occupation of A' $n_{Cl} + (\sigma_{N\ O3})$. (The parentheses signifies a minor contribution to the wavefunction.) In HOCl, the second peak is seen to be more intense than the first, also in agreement with this work. In contrast to HOCl, the first two peaks in $ClONO_2$ do not show evidence of vibrational structure; however, vibrational structure is usually less evident in polyatomic molecules due to the greater number of modes

which are excited upon ionization. The narrow width of these peaks adds support to the assignment of the peaks to nonbonding electrons. It is known that low lying (within ~ 3 eV of the HOMO) virtual orbitals can have a disproportionate effect on Koopmans' energies.[29] For $ClONO_2$, due to terms in the second-order correction to Koopmans' approximation, the major contribution to the relaxation comes from the interaction of the A' LUMO with the A" HOMO. This is indeed the case since the error term $\varepsilon_i - I_i$ is larger for system 1 (A") (1.46 eV) than for band 2 (A') (1.17 eV) (c.f. table 6.3). The relative magnitudes of the correction terms provides corroboration for the assignment given above.

The third and fourth systems are close to each other, broader than the first and second, and appear to have some vibrational structure. A closer view of these bands is given in fig. 6.6. From the calculation detailed in table 6.3, we assign these transitions to nonbonding and antibonding orbitals on the nitrate group. Peak 3 ((*a*) $n_{O2\ O3}$) is narrow, as would be expected. A weak excitation of the ν_3 N-O1 stretch (778 cm^{-1} in neutral $ClONO_2$)[31] can be seen in a series of three peaks with an average frequency of about 805 cm^{-1}. Peak 4, assigned to an $\sigma^*_{N\ O1\ O2\ O3}$ orbital, shows a more well-developed series of five peaks with an average spacing of 450 cm^{-1}. Since the electron is ejected from an antibonding orbital, we would expect the cation to be more strongly bound, and the ν_5 vibration at 434 cm^{-1} (NO_2 symmetric bend) is taken to be responsible for the series. The larger observed NO_2 frequency is consistent with a more strongly bound cation. In the spectrum of HNO_3, the NO_2 asymmetric stretch, in addition to the N-O1 stretch and NO_2 symmetric stretch, is excited in the analogous bands.

Band 5 is assigned to the orbital $n_{Cl\ O3}$, and shows a persistent vibrational series of frequency 825 cm^{-1}. This corresponds to the ν_4 vibration of $ClONO_2$ (Cl-O stretch) at 806 cm^{-1}.

Band 6 is at 14.87 eV, very close to a peak at 14.6 eV in the HOCl spectrum. We assign this band to the $\pi_{Cl\ O1}$ orbital, in analogy to the HOCl assignment. Similarly band 7 is at 16.22 eV, is assigned as A' $\sigma_{Cl\ O1}$, and has an analogous A' orbital at 15.6 eV in HOCl. Neither peak shows vibrational structure. The peaks exhibit similar widths to the analogous peaks in HOCl.

We assign peak 8 at 18.77 eV to ionization of the $\sigma_{O2\ N\ O3}$ orbital. It is analogous to a peak at 18.63 eV in the HNO_3 spectrum which also involves sigma bonding in the nitrate group. Neither peak shows vibrational structure and both show a steep slope on the low energy side and a slower falloff on the high energy side.

A comparison of the orbital energies of these molecules with those of $ClONO_2$ is provided in table 6.4 for reference.

6.6 Implications

An argument has been given for the assignment of the HOMO of $ClONO_2$ as n_{Cl} + $\pi^*_{Cl\ O}$, and for the next highest orbital as n_{Cl} + $(\sigma_{N\ O3})$. Since the *ab initio* results reported indicate that the LUMO is $\sigma^*_{Cl\ O1\ N}$, this would seem to imply that the UV absorption spectrum would have a contribution from an $n \rightarrow \sigma^*$ transition. However, recent theoretical results indicate that this is not the case. Using correlation methods, Graña[2] *et al.* find a Cl($n \rightarrow \sigma^*$) transition at 284 nm (f = 0.0013), an NO_2($n \rightarrow \pi^*$)

transition at 250 nm (f = 0.0000), a weak Cl($n \rightarrow \sigma^*$) transition at 240 nm (f = 0.0006), and an NO_2($n \rightarrow \pi^*$) transition at 215 nm (f = 0.0004). While these transitions are in the wavelength range of the first broad absorption band at 215 nm, the most intense absorption is a $\pi \rightarrow \pi^*$ transition at 190 nm (f = 0.1849). The present study provides experimental evidence for the n_{Cl} orbital and the $n_{O2\ O3}$ orbitals out of which the UV spectrum arises. In any case, although a weak $n \rightarrow \sigma^*$ transition may exist in the molecule, the observed photoproducts in $ClONO_2$ photolysis probably arise from excited state dynamics and curve crossings, and not to a simple bond-selective dissociation. It is difficult to make predictions concerning ClOOCl based on knowledge gained about the molecular orbitals of $ClONO_2$. Given the molecular orbitals of $ClONO_2$ and the observed photoproducts (Cl and ClO), it is improbable that the ClO chromophore and its $n \rightarrow \sigma^*$ transition will cause ClOOCl to photolyse with 100% yield of Cl + ClOO.

In summary, the photoelectron spectrum of $ClONO_2$ has been measured for the first time, and interpreted using *ab initio* calculations in combination with analogies to HOCl and HNO_3. In addition, the ionization potential of the molecule has been determined.

6.7 References

[1] T. K. Minton, C. M. Nelson, T. A. Moore and M. Okumura, *Science* **258**, 1342 (1992).

[2] A. M. Graña, T. J. Lee and M. Head-Gordon, *Journal of Physical Chemistry*, in press.

[3] J. B. Burkholder, R. K. Talukdar and A. R. Ravishankara, *Geophys. Res. Lett.* **21**(7), 585 (1994).

[4] J. C. Farman, B. G. Gardiner, and J. D. Shanklin, *Nature* **315**, 207 (1985).

[5] J. W. Waters, L. Froidevaux, W. G. Read, G. L. Manney, L. S. Elson, D. A. Flower, R. F. Jarnot and R. S. Harwood, *Nature* **362**, 597 (1993).

[6] J. G. Anderson, D. W. Toohey, W. H. Brune, *Science* **251**, 39 (1991).

[7] J. P. D. Abbatt and M. J. Molina, *J. Phys. Chem.* **96**, 7674 (1992). D. R. Hanson and A. R. Ravishankara, *J. Phys. Chem.* **98**, 5728 (1994).

[8] C. R. Webster, R. D. May, D. W. Toohey, L. M. Avallone, F. G. Anderson, P. Newman, L. Lait, M. R. Schoeberl, J. W. Elkins and K. R. Chan, *Science* **261**, 1130 (1993).

[9] L. T. Molina and M. J. Molina, *J. Phys. Chem.* **91**, 433 (1987).

[10] S. L. Nickolaisen, R. R. Freidl, and S. P. Sander, *J. Phys. Chem.* **98**, 155 (1994).

[11] D. D. Wagman, W. H. Evans, V. B. Parker, R. H. Schumm, I. Halow, S. M. Bailey, K. L. Churney and R. L. Nuttall, The NBS Tables of Chemical Thermodynamic Properties, *J. Phys. Chem. Ref. Data* **11**(2) (1982).

[12] W. B. DeMore, S. P. Sander, C. J. Howard, A. R. Ravishankara, D. M. Golden, C. E. Kolb, R. F. Hampson, M. J. Kurylo and M. J. Molina, Chemical Kinetics and Photochemical Data for Use in Stratospheric Modeling, Evaluation Number 10. JPL Publication 92-20, Pasadena, 1992.

[13] T. A. Moore, M. Okumura, M. Tagawa and T. K. Minton, *Faraday Transactions*, in press.

[14] E. M. Purcell, *Phys. Rev.* **54**, 818 (1938).

[15] M. Schmeisser, *Inorg. Synth.* **9**, 127 (1967).

[16] R. H. Miller, D. L. Bernitt and I. C. Hisatsune, *Spectrochimica Acta* **23A**, 223 (1967). J. Shamir, D. Yellin and H. H. Claasen, *Israel J. Chem.* 12(6), 1015 (1974). D. W. Amos and G. W. Flewett, *Spectrochimica Acta* **31A**, 213 (1975).

[17] F. S. Rowland, J. E. Spencer and M. J. Molina, *J. Phys. Chem.* **80**, 2711 (1976). L. T. Molina and M. J. Molina, *J. Photochem* **11**, 139 (1979).

[18] B.-M. Haas, K. C. Crellin, K. T. Kuwata and M. Okumura, *J. Phys. Chem.* **98**, 6740 (1994).

[19] A. Einstein, *Ann. Physik* **17**, 132 (1905).

[20] T. Koopmans, *Physika* **1**, 104 (1934).

[21] R. L. DeKock and H. B. Gray, Chemical Structure and Bonding, Benjamin Cummings, Menlo Park (1980).

[22] C. Møller and M. S. Plesset, *Physical Review* **46**, 618 (1934).

[23] R. J. Bartlett, *J. Phys. Chem.* **93**, 1697 (1989).

[24] D. W. Turner, C. Baker, A. D. Baker and C. R. Brundle, *Molecular Photoelectron Spectroscopy*, Wiley-Interscience, London (1970). K. Kimura, S. Katsumata, Y. Achiba, T. Yamazaki and S. Iwata, *Handbook of HeI Photoelectron Spectra of Fundamental Organic Molecules*, Japan Scientific Societies Press, Tokyo (1981).

[25] D. P. Chong, F. G. Herring and Y. Takahata, *J. Elect. Spect. and Rel. Phen.* **13**, 39 (1978).

[26] D. C. Mason, D. M. Mintz and A. Kuppermann, *Rev. Sci. Instrum.***48**(7), 926 (1977).

[27] B. Casper, P. Lambotte, R. Minkwitz and H. Oberhammer, *J. Phys. Chem.* **97**, 9992 (1993). T. J. Lee and J. E. Rice, *J. Phys. Chem.* **97**, 6637 (1993).

[28] D. Colbourne, D. C. Frost, C. A. McDowell and N. P. C. Westwood, *J. Chem. Phys.* **68**(8), 3574 (1978). D. P. Chong, F. G. Herring and Y. Takahata *J. Elect. Spect. and Rel. Phen.* **13**, 39 (1978).

[29] D. P. Chong, F. G. Herring and Y. Takahata, *J. Electron Spectrosc. Relat. Phenom.* **13**, 39 (1978). A. B. Cornford, D. C. Frost, F. G. Herring and C. A. McDowell, *J. Chem. Phys.* **55**(6), 2820 (1971). D. P. Chong, F. G. Herring and D. McWilliams, *J. Chem. Phys.* **61**, 78 (1974).

[30] D. C. Frost, S. T. Lee, C. A. McDowell and N. P. C. Westwood, *J. Electron Spectrosc. Relat. Phenom.* **7**, 331 (1975).

[31] J. Shamir, D. Yellin and H. H. Claassen, *Israel J. of Chem.* **12**(6), 1015 (1974).

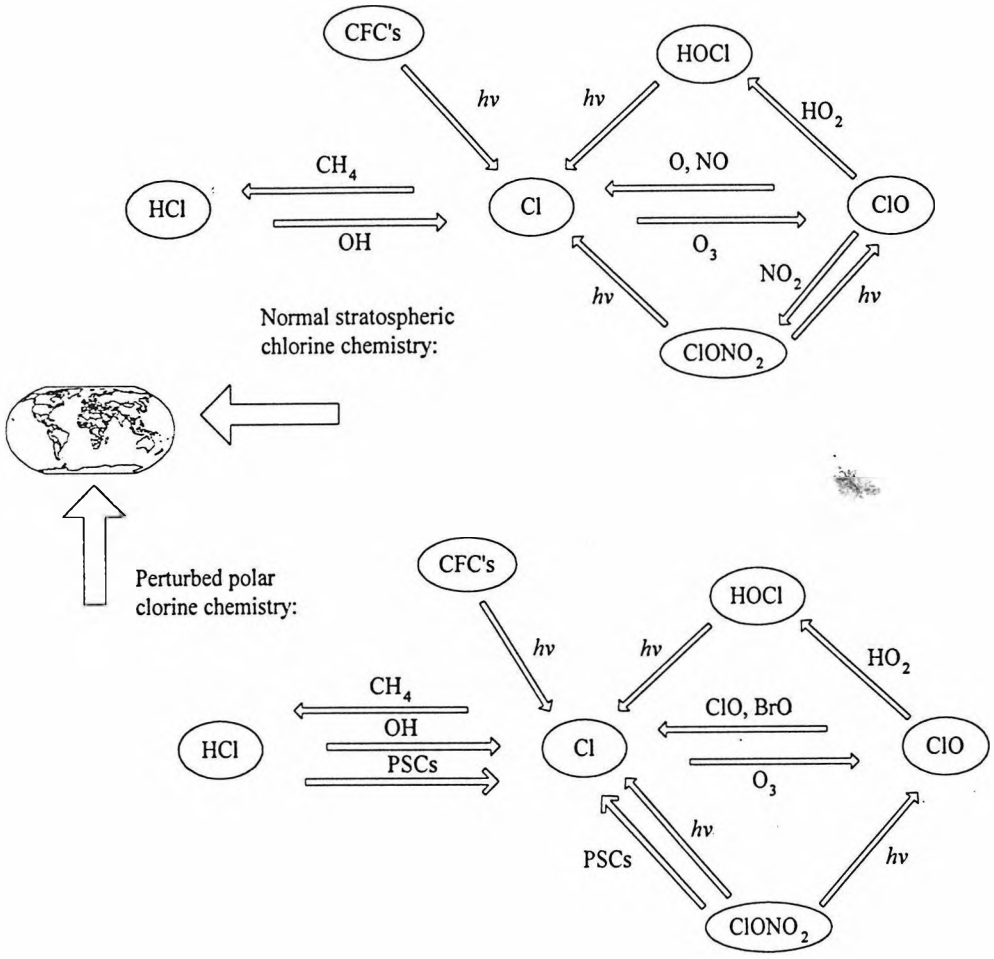

Figure 6.1 Diagram comparing normal stratospheric chlorine chemistry with the perturbed heterogeneous chemistry in the Antarctic vortex.

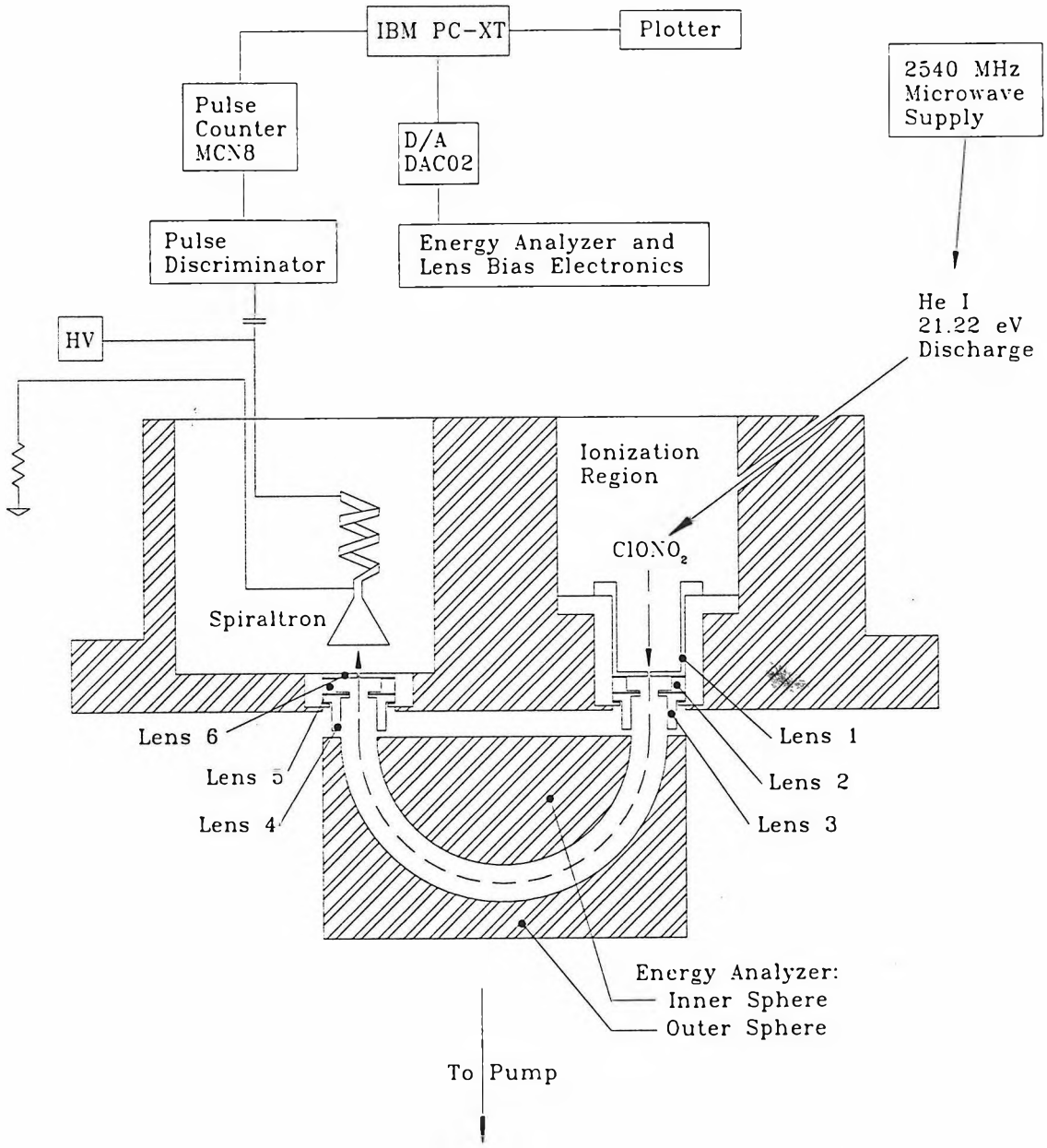

Figure 6.2 Schematic diagram showing primary components of the photoelectron instrument.

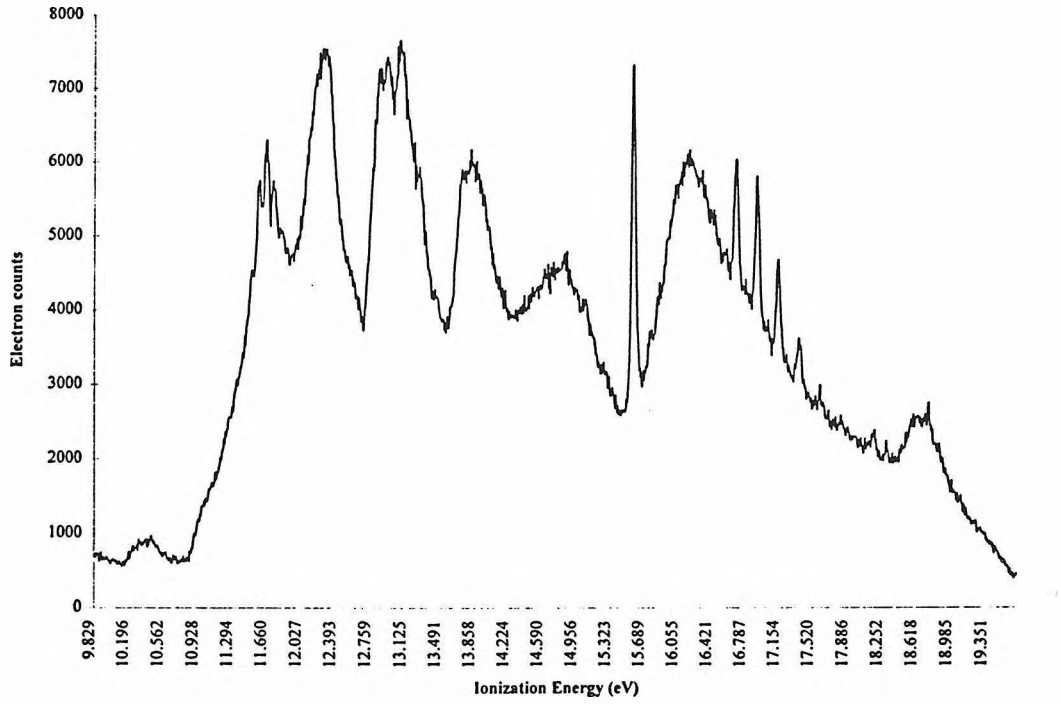

Figure 6.3 (a): $ClONO_2$ photoelectron spectrum, nitrogen calibration, file 0827, 34.6 s/point.

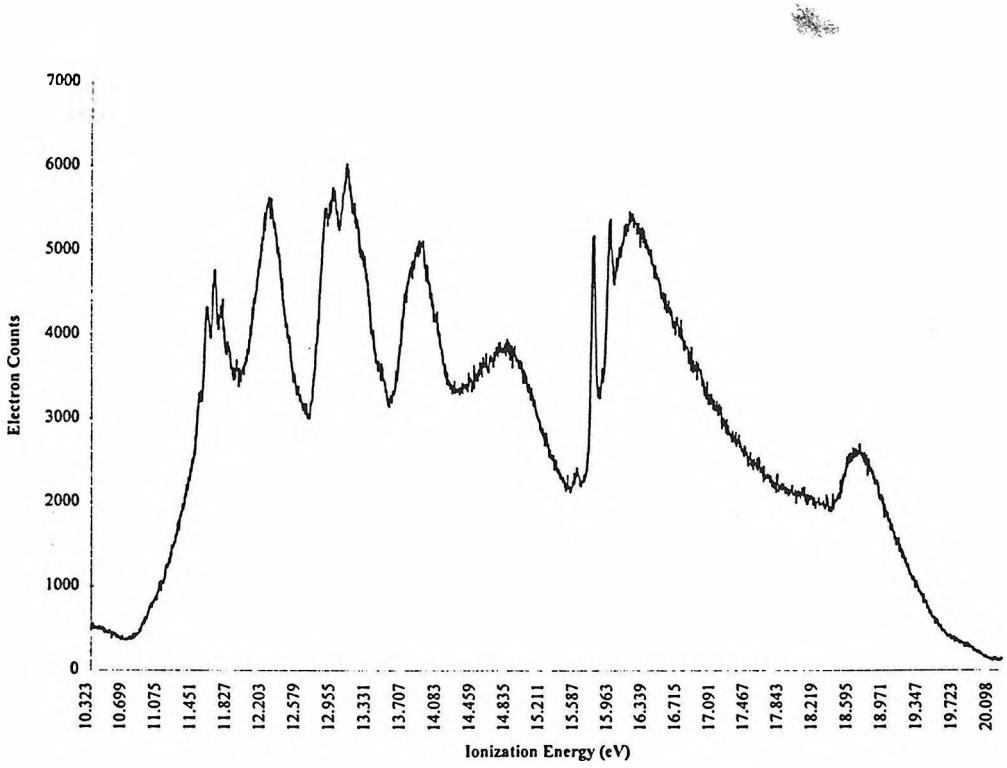

Figure 6.3 (b): $ClONO_2$ photoelectron spectrum, argon calibration, file 0829, 18.6 s/point.

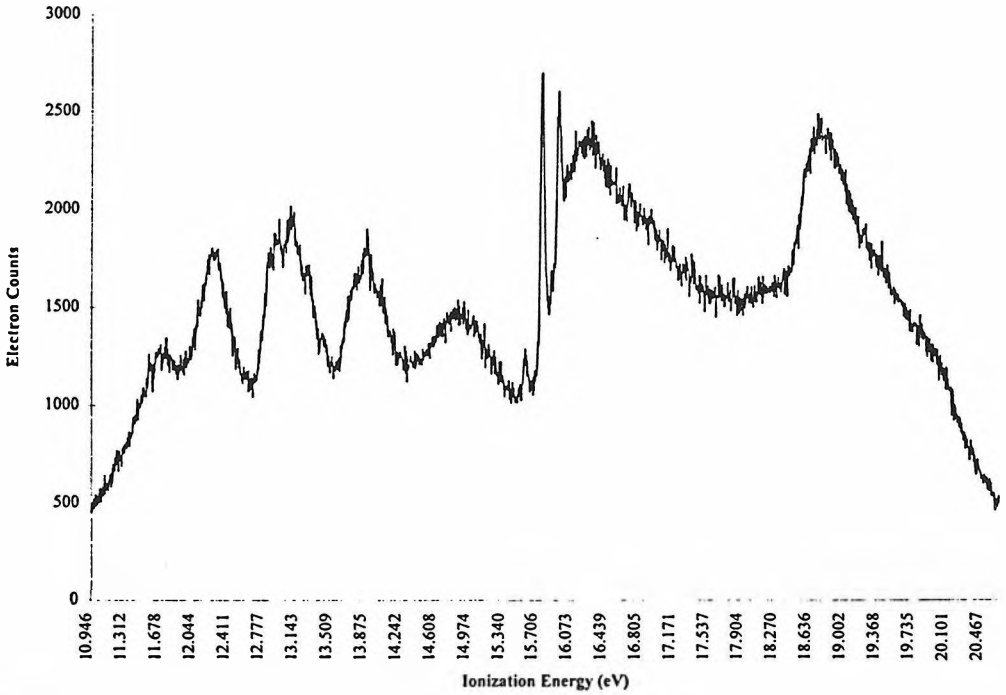

Figure 6.3 (c): $ClONO_2$ photoelectron spectrum, argon calibration, file 0916, 11.9 s/point.

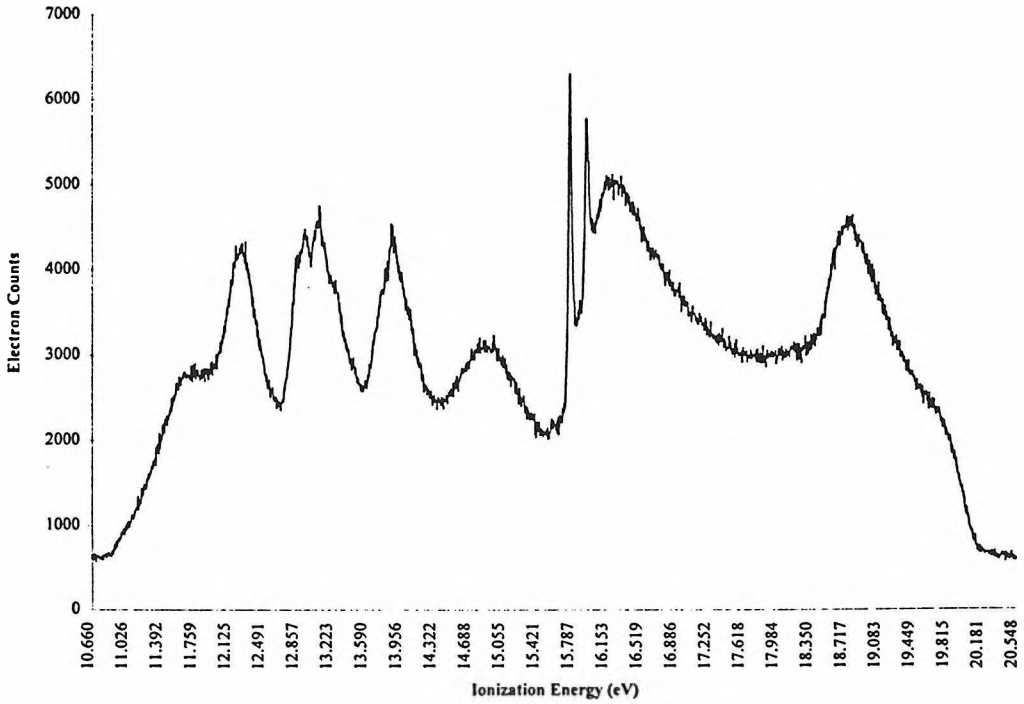

Figure 6.3 (d): $ClONO_2$ photoelectron spectrum, argon calibration, file 0926, 35.7 s/point.

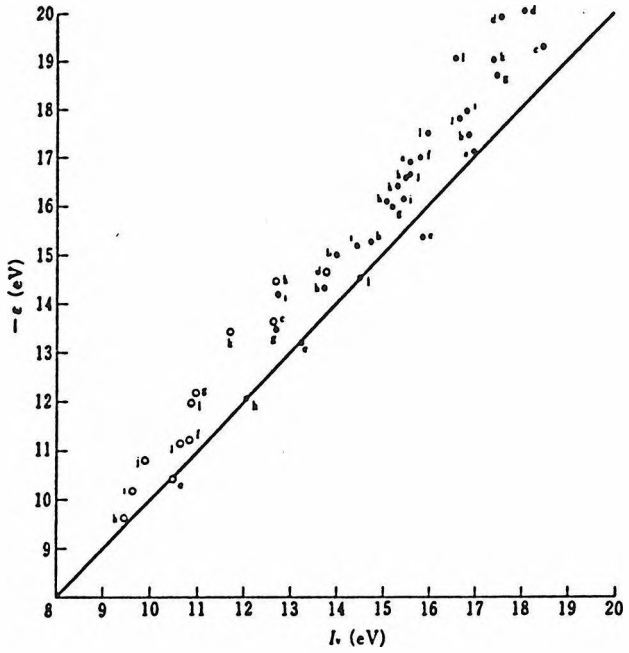

Figure 6.4: Correlation between -ε(Koopmans) and I_i(experimental) for molecules with nonbonding orbitals. Line represents $-\varepsilon = I_i$.

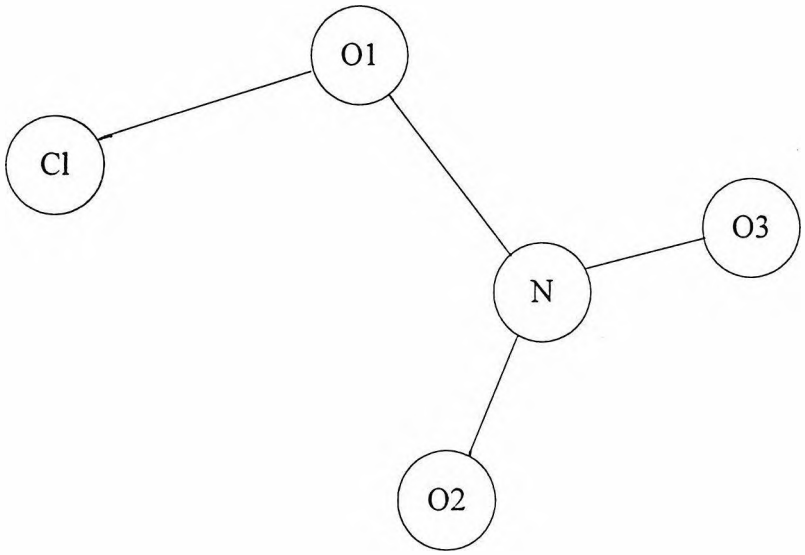

Figure 6.5: The structure of $ClONO_2$ and convention for labelling oxygen atoms.

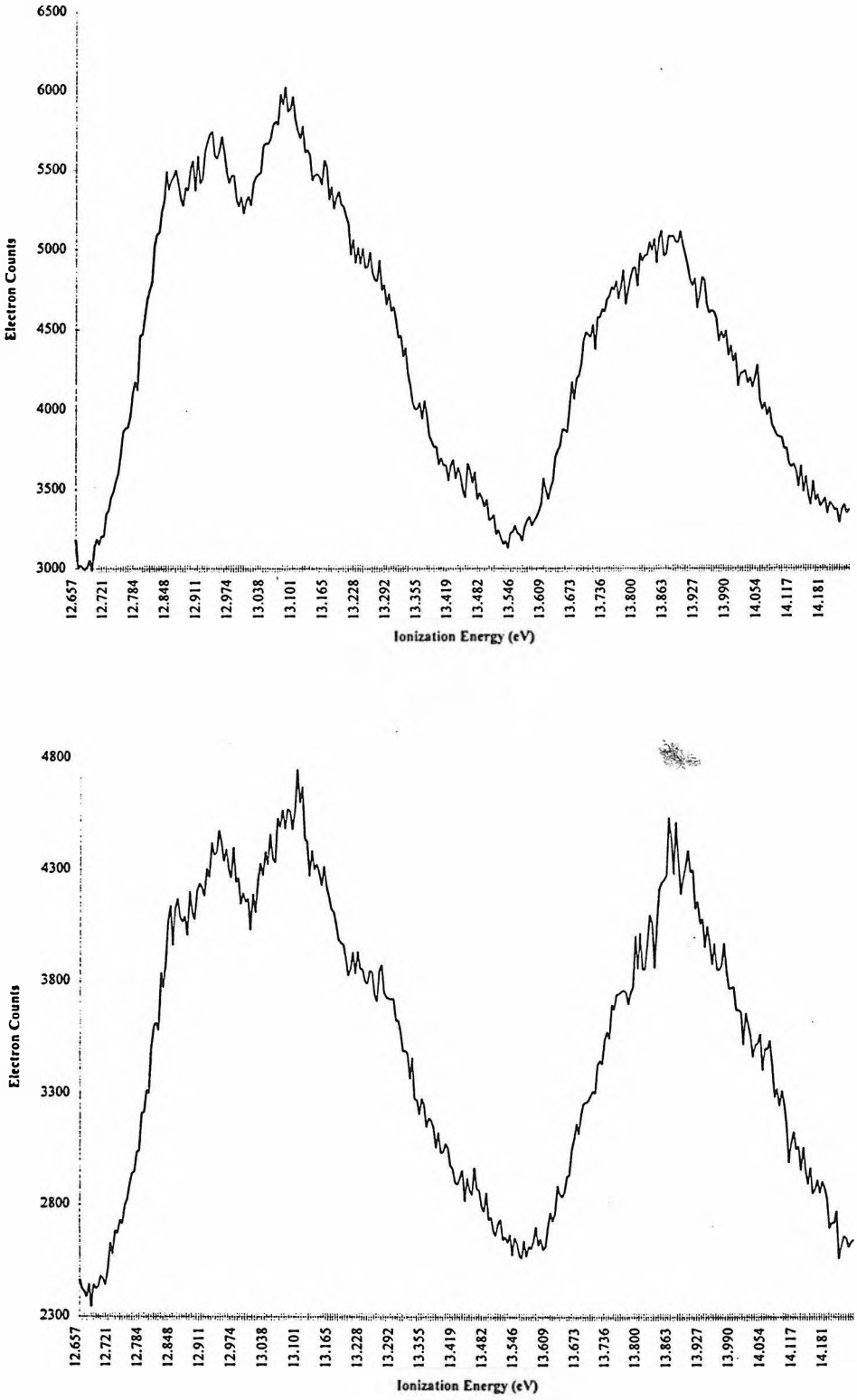

Figure 6.6: Detail of vibrational structure on peaks 3, 4 and 5. (a) File 0829. (b) File 0926.

Peak Number:	IP	1	2	3	4	5	6	7	8
6.2(a) 0827AD02	10.85	11.67	12.27	12.94	13.07	13.83	14.84	16.19	18.65
6.2(b) 0829AD04	10.88	11.66	12.25	12.94	13.08	13.85	14.81	16.18	18.68
6.2(c) 0916AD03	---	11.67	12.27	12.95	13.08	13.89	14.86	16.25	18.77
6.2(d) 0926AD98	10.86	11.66	12.25	12.94	13.10	13.86	14.87	16.22	18.77

Table 6.1. Ionization potential and vertical excitation energy (1 to 8) for $ClONO_2$ spectra in figure 6.2. Energies given in eV. Spectral resolution is 0.045 eV.

Peak Number:	1	2	3	4	5	6	7	8
SCF/631-G	14.09	13.58	14.26	15.09	15.72	18.14	18.30	21.65
SCF/631G(d)	13.35	13.67	13.89	14.74	15.59	17.64	18.37	21.62
MP2fc/6-311+G(d)	13.17	13.45	14.39	15.15	15.56	17.63	17.89	21.84
MP2fc/6-311(2+)G(d)	13.16	13.45	14.38	15.14	15.59	17.62	17.88	21.83
CCSDfc/6-31G(d)// MP2fc/6-311+G(d)	13.01	13.30	14.27	14.98	15.44	17.45	17.72	21.66
CCSDfc/6-31+G(d)// MP2fc/6-311+G(d)	13.12	13.42	14.42	15.13	15.58	17.59	17.87	21.80
CCSDfc/6-31+G(d)// MP2fc/6-311(2+)G(d)	13.12	13.42	14.42	15.13	15.58	17.59	17.87	21.80

Table 6.2. Orbital energies for $ClONO_2$. Note that the ordering of the first two valence levels in the SCF/631-G calculation is reversed. The symmetry and atomic orbital occupations from the calculations are presented in table 6.3. For the CCSD calculations the notation signifies that the orbital energies were calculated using the first level of theory (before the double slash) using a geometry optimized and frozen at the second level of theory. Calculations performed using the Gaussian 92 suite of programs.

	System	I_i	ε_i		Assignment
0	LUMO		-1.04	*A'*	$\sigma^*_{Cl\ O1\ N}$
1	HOMO	11.66	13.12	*A"*	$n_{Cl} + \pi^*_{Cl\ O}$
2		12.25	13.42	*A'*	$n_{Cl} + (\sigma_{N\ O3})$
3		12.94	14.42	*A"*	*(a)* $n_{O2\ O3}$
4		13.10	15.13	*A'*	$\sigma^*_{N\ O1\ O2\ O3}$
5		13.86	15.58	*A'*	$n_{Cl\ O3}$
6		14.87	17.59	*A"*	$\pi_{Cl\ O1}$
7		16.22	17.87	*A'*	$\sigma_{Cl\ O1}$
8		18.77	21.80	*A'*	$\sigma_{O2\ N\ O3}$

Table 6.3. Eigenvalues and wavefunctions of CCSDfc/6-31+G(d)//MP2fc/6-311(2+)G(d) calculation, and comparison of energies to experimental values.

HOCl		$ClONO_2$		HNO_3	
11.22	*A"* $\pi^*_{Cl\ O1}$	11.66	*A"* $n_{Cl} + \pi^*_{Cl\ O}$		
12.27	*A'* $n_{Cl} + \pi^*_{Cl\ O1}$	12.25	*A'* $n_{Cl} + (\sigma_{N\ O3})$	12.39	*A"* $n_{O2\ O3}$
		12.94	*A"* *(a)* $n_{O2\ O3}$	12.63	*A'* *(a)* $n_{O2\ O3}$
		13.10	*A'* $\sigma^*_{N\ O1\ O2\ O3}$	13.23	*A'* *(b)* $n_{O2\ O3}$
		13.86	*A'* $n_{Cl\ O3}$	13.70	*A"* n_o
14.6	*A"* $\pi_{Cl\ O1}$	14.87	*A"* $\pi_{Cl\ O1}$		
15.6	*A'* $\sigma_{Cl\ O1}$	16.22	*A'* $\sigma_{Cl\ O1}$	16.78	*A'* σ_{OH}
		18.77	*A'* $\sigma_{O2\ N\ O3}$	18.63	*A'* $\sigma_{N\ O1\ O2\ O3}$
				19.24	*A"* $\pi_{N\ O2\ O3}$
				21	*A'* $\sigma^*_{N\ O1\ O2\ O3}$

Table 6.4. Comparison of the vertical ionization potentials of HOCl, $ClONO_2$ (this work) and HNO_3.

Appendix A:

Some Useful Circuits

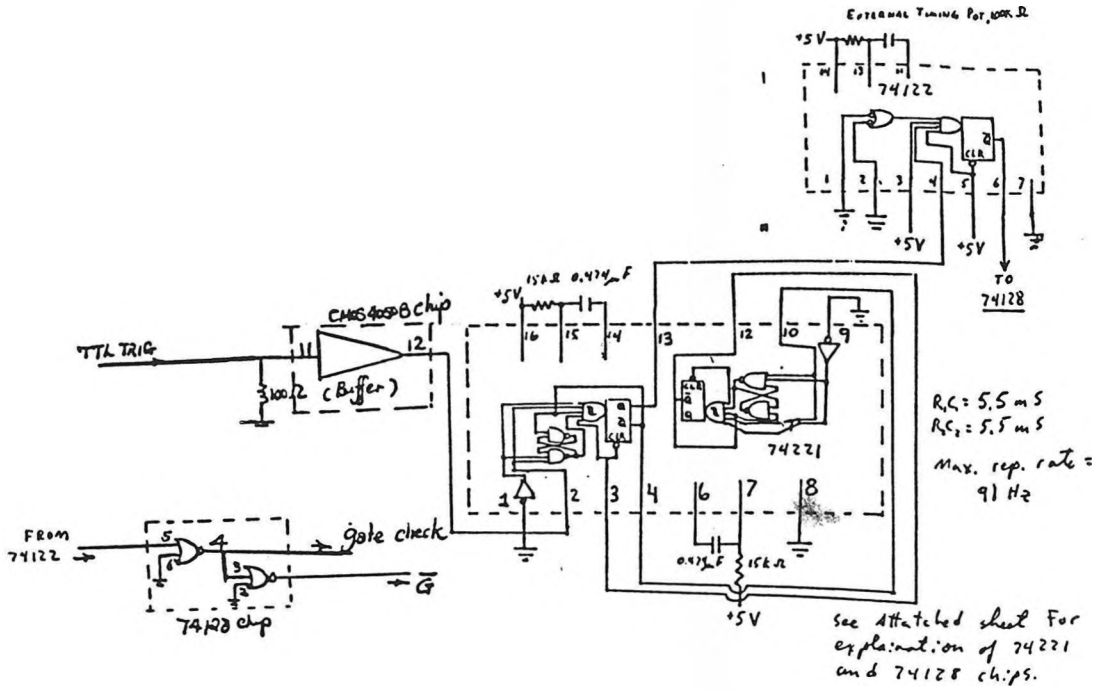

Figure A.1 Diagram of the TTL buffer board. In this circuit an external potentiometer controls the width of the output pulse. Pulse widths from 30 ns to 500 ms are possible, depending on the value of the resistor and capacitor used in the 74122 chip. The pulse width is approximately $\tau = R\ C\ \ln(2)$. The 74221 chip causes the board to have a maximum possible repetition rate of 91 Hz. This safety feature will prevent damage to whatever circuit this board is driving through too rapid triggering. The output chip is a 50 Ω line driver, and the input impedance is 50 Ω. This circuit has been in continuous use for five years in a variety of applications, including high voltage pulse generators, piezoelectric drivers, solenoid drivers, and the thyratron pulse generator (chapter 4).

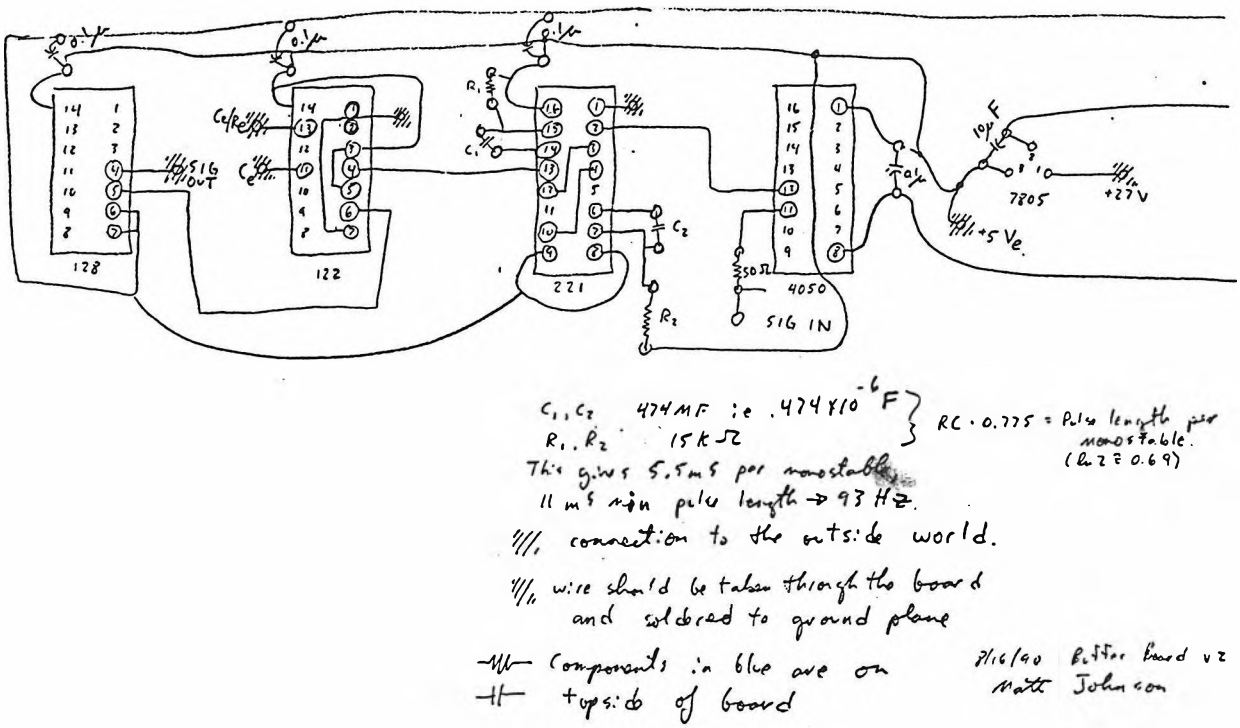

Figure A.2 Circuit diagram for the TTL pulse delay generator shown in fig. A.1, giving a more detailed explanation of circuit operation.

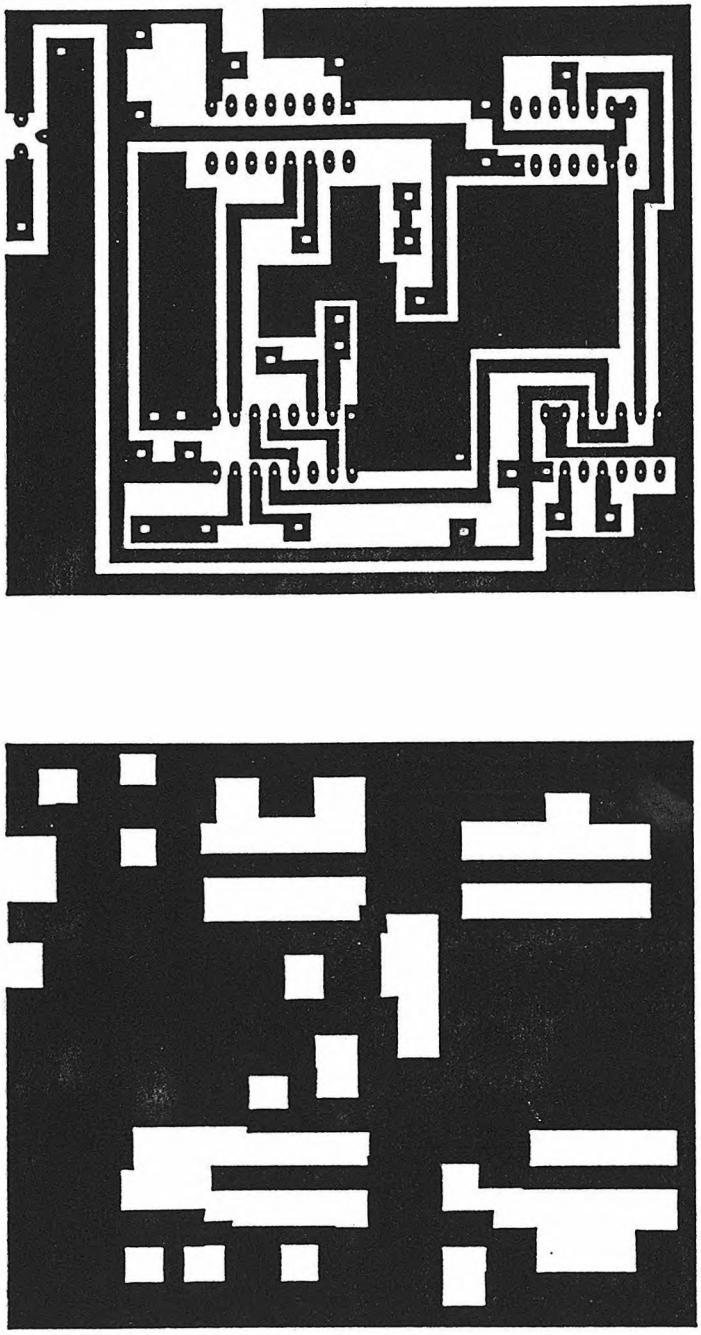

Figure A.3 Masks used for etching the printed circuit boards used in the TTL pulse delay generator. Directions for etching circuit boards may be found for example in *The Art of Electronics* by Horowitz and Hill (1989). The scale is 1:1.

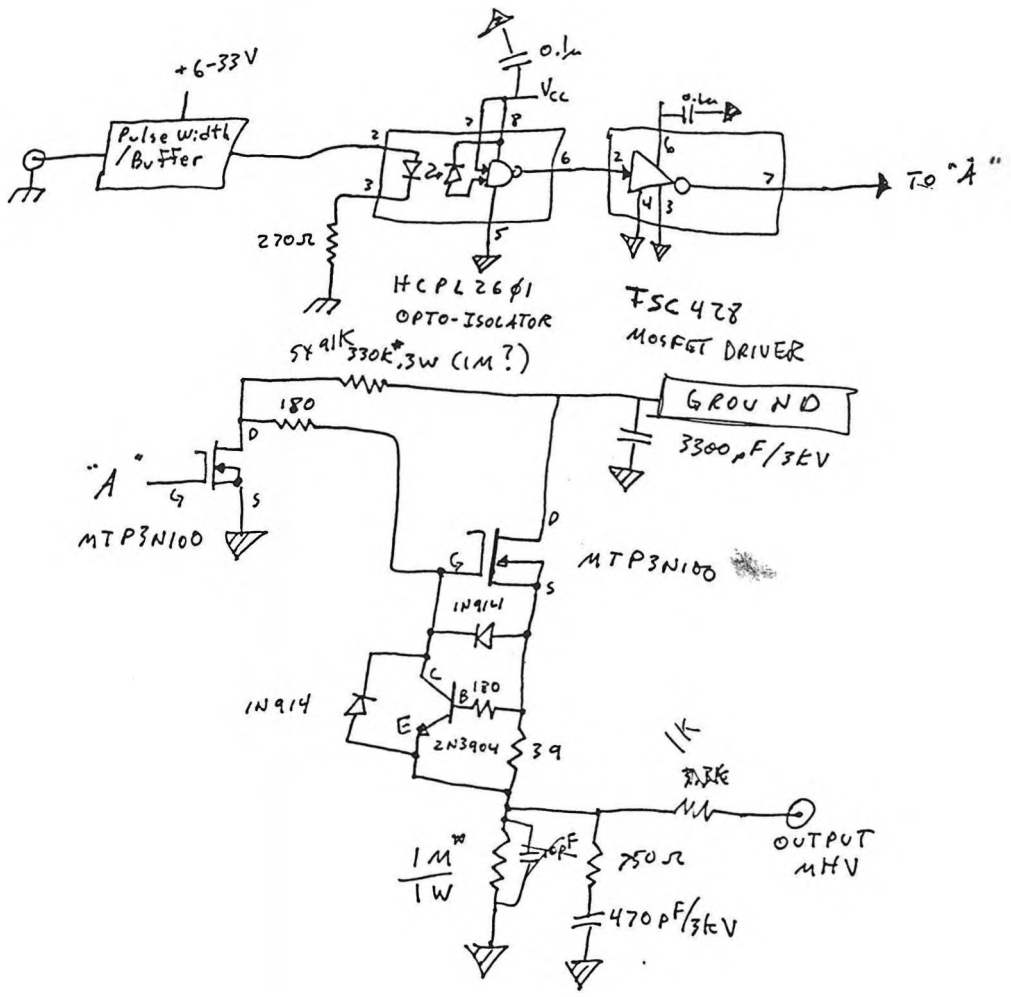

Figure A.4 Circuit diagram of piezoelectric driver circuit used to drive the piezoelectric valve detailed in chapters 2 and 4. This circuit has provided dependable service for five years, and at least two copies have been made. The circuit is modified from a lower voltage piezo driver presented in *The Art of Electronics* by Horowitz and Hill, pg. 169.

(*a*) 40 dB op amp circuit used for amplification of power meter signal in chapters 2 and 3.

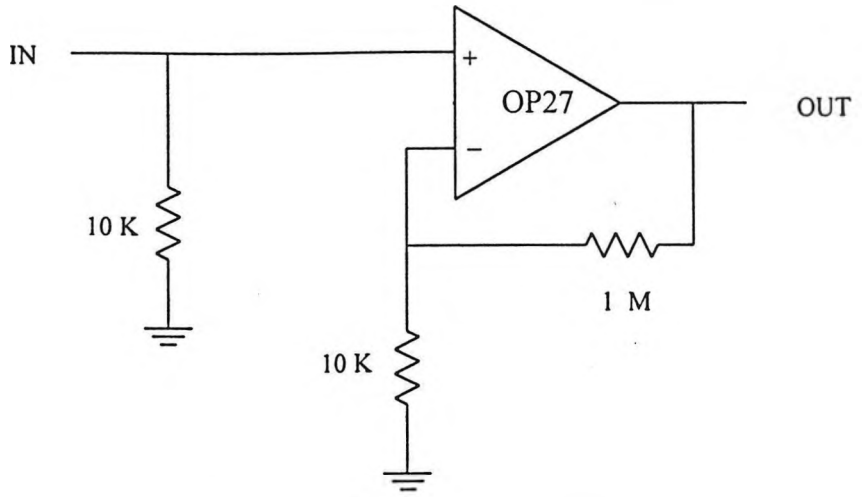

(*b*) 26 dB fast op amp used for amplifying photomultiplier signal in chapter 3. Elimination of stray capacitance and power supply noise was critical to the success of this circuit. The rise time of the circuit was measured at 10 ns.

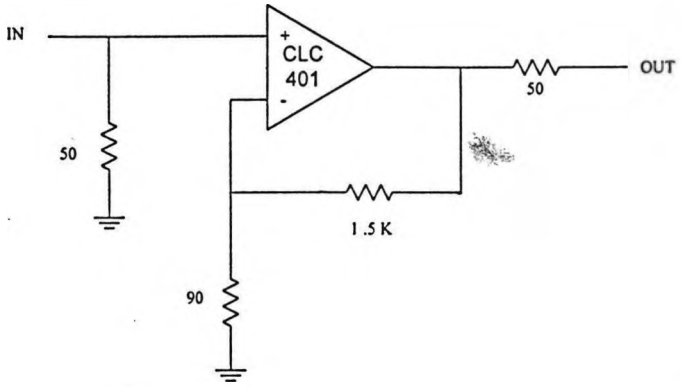

(*c*) 14 dB fast (10 ns) op amp used for amplifying photomultiplier signal in chapter 3. As with the circuit above, careful construction was necessary to avoid oscillation.

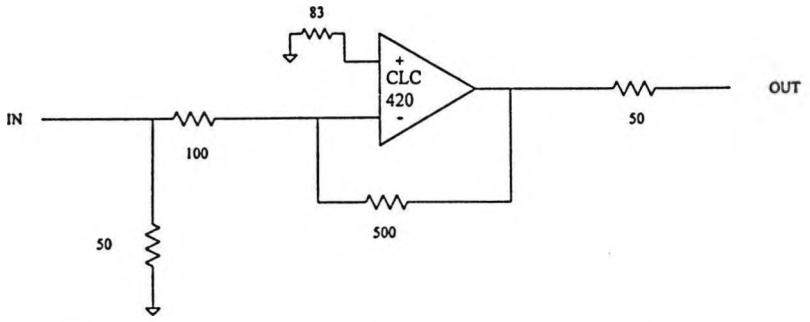

Figure A.5 Op amps used for signal amplification. Each of these circuits was constructed on a board provided by the Comlinear company which was designed specifically for fast op amp applications. The three circuits shown above employed OP27, CLC401 and CLC420 eight pin chips respectively.

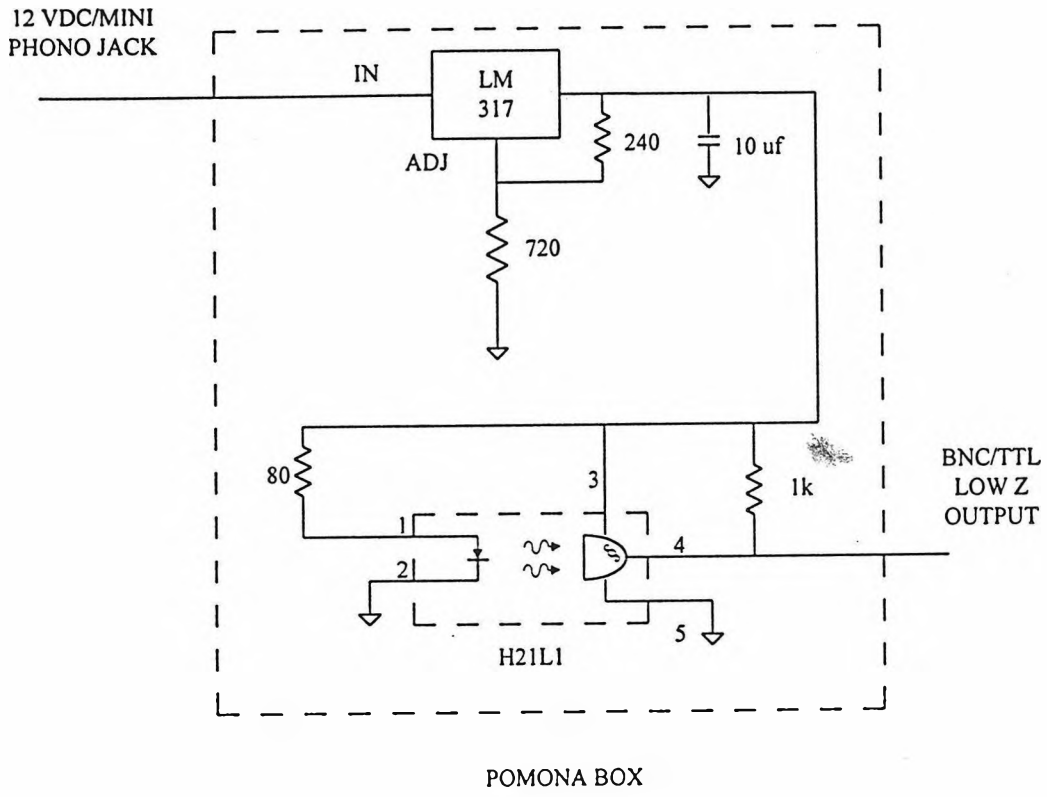

Figure A.6 Photon coupled interrupter circuit used to detect the frequency of rotation of a chopper wheel (SRS). The output of this circuit was fed into a lock-in amplifier to provide phase-sensitive detection of a fluorescence experiment.

Appendix B:

The Program PES

B.1 Abstract

The program PES was written using Borland Turbo Pascal version 4.0. The program controls scanning and data collection for the photoelectron spectrometer (PES) used in chapter 6, and used by the undergraduate physical chemistry laboratory at the California Institute of Technology. The program controls a scalar board and a D/A converter (Keithley-Metrabyte), saves data files in a text format suitable for loading into a spreadsheet program, and runs on a PC-AT.

```
{                    PES.PAS                    }

{ The program PES.PAS is intended to interface with the Chem. 6 Photoelectron
  Spectrometer. The program will control scanning of the spectrometer, data
  collection, and data manipulation. Written by Matt Johnson, winter and
  spring 1992.}
{ Unit CURSORS added 8/3/92 MSJ}
{ Menu options F9, F10, Alt-Z, Alt-A added 8/92 MSJ}

{$E-}
{$I+}   {I/O checking on}
{$N+}   {Numeric coprocessor on}
{$S+}   {Stack checking on}
{$M 65220,0,10000}
      {Maximize stack volume}

program PES;

uses GLOBALS, DOS, CRT, Graph, DOKEYU, GRAPHU, CURSORS;

var
  BGIGraphDriver, BGIGraphMode : integer;
  Key  : Char;
  keyF : Boolean;
  keyN,i,j : integer;
  rj : real;

procedure introscreen;  {Title Screen}
  begin
    textbackground(black);
    clrscr;
    window(20,10,60,20);
    textbackground(blue);
    clrscr;
    window(18,9,58,19);
    textbackground(lightgray);
    clrscr;
    window(16,8,56,18);
    textbackground(red);
    clrscr;
    textcolor(black);
    gotoxy(15,5);
    writeln('** PES **');
    Delay(1000);
    {for j := 1 to 2000 do}
    {   sound(round(640 + 200*sin(j/50)*sin(j/40)));}
    {NoSound;}
    for i := 1 to 30 do
      begin
      textbackground(random(16));
      clrscr;
```

```
        delay(50);
        end;
    window(1,1,80,25);
    textbackground(black);
    clrscr;
  end;  {procedure introscreen}

procedure initvars;  {initializes global variables}
  begin
    minv := $0000; rminv := 0;  minvax := 0;
    maxv := $0FFF; rmaxv := 10;  maxvax := $0FFF;
    slopex := 1; slopey := 1; xoff := 0; yoff := 0;
    exiting  := FALSE;
    pause := 50;
    df:= 1;
    SetGraphMode(BGIGraphMode);
    zoomx := 1;  zoomy := 1;
    xoffset := 0;  yoffset := 0;
    scl2 := 1;
    numsweeps := 1;
    resolution := 2;
    minvax := 0;
    maxvax := 4095;
    erasegraph := TRUE;
    for i := 1 to 2 do
        begin
        offset[i] := 0;
        integrl[i] := 0;
        gotdata[i] := FALSE;
        datafile[i] := 'noname';
        end;
    for i := 0 to 15 do
        SetPalette(i,i);  {resets color palette}
    ActiveCursor := 1;
    for i := 1 to 4 do
       CursorPos[i] := 0;
  end;      { procedure doinit }

procedure bgiinit;  {initializes bgi graphics}
   begin
      BGIGraphDriver := Detect;
      DetectGraph(BGIGraphDriver, BGIGraphMode);
      InitGraph(BGIGraphDriver, BGIGraphMode, 'C:\LIB');
      RestoreCRTMode;
   end;       {procedure bgiinit}

begin { program PES }

  bgiinit;          {PES}
  introscreen;       {uses CRT mode}
  initvars;         {Changes to graph mode for rest of program}
  drawscreen;        {GRAPHU}
  disppars;         {GRAPHU}
  curswind;          {CURSORS}
```

```
  while NOT exiting do      {this loop is the program; see DOKEYU}
     begin
     GetKey(KeyF,KeyN,Key);
     DoKey(KeyF,KeyN);
     end;
  CloseGraph;
  TextColor(LightGray);
  ClrScr;
end.
      { Program  PES }


{                    GLOBALS.PAS                          }
{constant and variable declarations for PES program              }
unit GLOBALS;

interface

uses DOS;

const DATAIO = $300;  {data I/O address for MDB-64}
     ADRPTR = $301;  {address pointer for MDB-64}
     MRESET = $302;  {address of reset for MDB-64}
     MCN8   = $00;   {address of MCN8 on MDB-64 bus}
     LOBYTADDR = 2;  {low byte counter on MCN8}
     HIBYTADDR = 3;  {high byte counter on MCN8}
     DAC0   = $308;  {address of DAC02 channel 0}
     DAC1   = $30A;  {address of DAC02 channel 1}
     MAXDATA = $1000; {max number of data points- 12 bits.}
     FORE = 1;       {Color code for foreground cursor}
     BACK = 2;       {Color code for background cursor}
     ERASE = 3;      {Code for eraseng cursor}

type  PESdatatype = array[1..2, 1..2, 1..MAXDATA] of word;
      cursortype = array[1..4] of word;
      integrltype = array[1..2] of longint;
      datafiletype = array[1..2] of pathstr;
      gotdatatype = array[1..2] of boolean;
      offsettype = array[1..2] of integer;

var  {global variables}
     minv, maxv, pause : word;  {min and max voltages of scan; delay in ms}
     timeperpoint, minvax, maxvax  : word;   {min and max voltages for graph, 12 bit}
     erasegraph, graphtrue, exiting : boolean;    {Condition flags}
     PESdata : PESdatatype;                  {Holds PES data}
     scl2, rminv, rmaxv, zoomx, zoomy, xoffset, yoffset : real;
     resolution, numsweeps : integer;
     ActiveCursor, int12, int34 : integer;
     CursorPos : cursortype;
     slopex, slopey, xoff, yoff  :  real;  {used in graphing data}
     integrl :  integrltype;  {integral values between markers}
     datafile  :  datafiletype;  {holds pathnames for two files}
     df  :  word;  {dataflag; signals which data set is active}
     gotdata  :  gotdatatype;  {signals if active data set exists}
```

```
   offset : offsettype;

implementation

end.   {unit globals}

{              DOKEYU.PAS              }

unit DOKEYU;

interface

uses GRAPH, DOS, CRT, GLOBALS, GRAPHU, CURSORS;


procedure GetKey(var funckey: boolean; var i: integer; var ch: char);
procedure DoKey(fnction: boolean; keycode: integer);

implementation

procedure GetKey(var funckey: boolean; var i: integer; var ch: char);
      begin
      funckey := FALSE;
      ch := ReadKey;
      if ch = #0 then
         begin
         funckey := TRUE;
         ch := ReadKey;
         end;
      i := ord(ch);
      end;          {procedure GetKey}

procedure DoKey(fnction: boolean; keycode: integer);
   type newpestype = array[1..2, 1..MAXDATA] of word;
   var
      i,j, minok, maxok, strok, intok : integer;
      continue, ok, okdokey : boolean;
      resp, minvp, maxvp, tempdf, voltage, sig, word1, tempword : word;
      sighi, siglo : byte;
      OldD, TempD, name, TempStr, TempStr1, TempStr2 : string;
      data : text;
      tempreal, temprl : real;
      reso, tempint, scanlength, lo, hi : integer;
      ch : char;
      Fillinfo : FillSettingsType;
      tmpi1, tmpi2 :  integer;
      newpes : newpestype;

   begin
      if fnction = TRUE then
         case keycode of
            20 : begin {Alt-T}  {Take Data}
                    ChToUsWind;
                    continue := TRUE;
```

```
SetColor(Black);
Bar(1,61,308,90);
OutTextXY(1,61,'Taking Data');
OutTextXY(1,71,'Press Alt-S To Stop Scan.');
GetFillSettings(Fillinfo);
SetFillStyle(SolidFill,Cyan);
Bar(1,81,250,90);
voltage := maxv;
i := 3;
PESdata[df,1,1] := minv;
PESdata[df,2,1] := maxv;
PESdata[df,1,2] := resolution;
timeperpoint := pause * numsweeps;
PESdata[df,2,2] := timeperpoint;  {time per point}
scanlength := 1 + ((maxv - minv) div resolution);
for j := 3 to (scanlength + 3) do
   PESdata[df,2,j] := 0;
j := 1;
graphtrue := TRUE;
datafile[df] := 'noname';
gotdata[df] := TRUE;
portw[DAC0] := (voltage shl 4);
delay(500);  {These last two lines may help increas accuracy.}
while ((j <= numsweeps) AND (continue = TRUE)) do
    begin
    while  ((voltage >= minv) AND (voltage < 4097) AND (continue = TRUE)) do
        begin
        port[MRESET] := $00;  {reset counters}
        delay(pause);   {allow data to accumulate}
        port[ADRPTR] := MCN8 + LOBYTADDR;
        siglo := port[DATAIO];
        port[ADRPTR] := MCN8 + HIBYTADDR;
        sighi := port[DATAIO];
        PESdata[df,1,i] := voltage;
        voltage := voltage - (resolution * $0001);
        portw[DAC0] := (voltage shl 4);
        sig := 256 * sighi + siglo;
        PESdata[df,2,i] := PESdata[df,2,i] + sig;
        i := i + 1;
        if (i mod 40 = 0) then
            begin
            SetFillStyle(InterLeaveFill, Magenta);
            tempreal := (i + (j - 1) * scanlength)/(scanlength * numsweeps);
            Bar(1,81,round(tempreal * 250), 90);
            if KeyPressed = TRUE then
              begin
              Ch := ReadKey;
              if (Ch = #0) then
                begin
                Ch := Readkey;
                if ord(Ch) = 31 then
                    continue := FALSE;
                end;  {if}
              end;  {if}
```

```
                end; {if}
              end;  {while}
            voltage := maxv;
            i := 3;
            j := j + 1;
            graphdata;
            ChToUsWind;
            end; {while}
          portw[DAC0] := $0000;
          ChToUsWind;
          with FillInfo do
            SetFillStyle(Pattern, Color);
          Bar(1,61,308,80);
          OutTextXY(1,61,'Done Collecting Data.');
          Sound(440); Delay(500); NoSound; Delay(500);
          Bar(1,61,308,90);
      end;  {Take Data}

34 : begin {Alt-G}  {Graph Data}
          ChToUsWind;
          SetColor(LightBlue);
          if gotdata[df] = TRUE then
            begin
            Bar(1,61,308,70);
            OutTextXY(1,61,'Graphing Data.');
            graphtrue := TRUE;
            graphdata;
            ChToUsWind;
            Bar(1,61,308,80);
            end; {if}
          if gotdata[df] = FALSE then
            begin
            Bar(1,61,308,70);
            OutTextXY(1,61,'No Data to Graph.');
            Sound(880); Delay(500); NoSound; Delay(500);
            Bar(1,61,308,70);
            end;  {if}
      end;  {Graph Data}

16 : begin {Alt-Q}  {Quit Program}
          ChToUsWind;
          Bar(1,61,308,70);
          OutTextXY(1,61,'Exiting Program.');
          exiting := TRUE;
      end;  {Quit Program}

25 : begin {Alt-P}  {Plot Data}
          ChToUsWind;
          SetColor(LightCyan);
          Bar(1,61,308,70);
          if gotdata[df] = TRUE then
            begin
            OutTextXY(1,61,'Plotting File ' + datafile[df]);
            graphtrue := FALSE;
```

```
            graphdata;
            ChToUsWind;
            end  {if}
         else  OutTextXY(1,61,'No Data to Plot.');
         Sound(880); Delay(500); NoSound; Delay(500);
         Bar(1,61,308,70);
      end;  {Print Data}

   31 : begin {Alt-S}  {Save Data}
         ChToUsWind;
         SetColor(LightGreen);
         if gotdata[df] = TRUE then
            begin
            {$I-}
            Bar(1,61,308,80);
            OutTextXY(1,61,'Enter filename for data:');
            OutTextXY(1,71,'(PES will append .dat to name)');
            GetStr(tempstr);
            datafile[df] := tempstr;
            Bar(1,71,308,80);
            OutTextXY(1,71,'Filename is ' + datafile[df] + '.dat');
            assign(data, datafile[df] + '.dat');
            rewrite(data);
            for i := 1 to (((maxv - minv) div resolution) + 3) do
               begin
               Str(PESdata[df,1,i], TempStr1);
               Str(Pesdata[df,2,i], TempStr2);
               writeln(data, TempStr1 + '  ' + TempStr2);
               end;  {for}
            close(data);
            Bar(1,71,308,80);
            OutTextXY(1,71,'Data Saved.');
            Sound(400); Delay(300); NoSound; Delay(400);
            Bar(1,61,308,90);
            graphdata;
            {$I+}
            end;  {if}
      end;  {Save Data}

   38 : begin {Alt-L}  {Set Scan Limits}
         ChToUsWind;
         SetColor(Blue);
         ok := FALSE;
         while ok = FALSE do
            begin
            Bar(1,61,308,70);
            OutTextXY(1,61,'Enter Voltage for start of scan,');
            OutTextXY(1,71,'0 to 10V range.');
            GetStr(Tempstr);
            Val(Tempstr, rmaxv, minok);
            Bar(1,61,308,70);
            OutTextXY(1,61,'Enter Voltage for end of scan,');
            OutTextXY(1,71,'0 to 10V.');
            GetStr(Tempstr);
```

```
                Val(Tempstr, rminv, maxok);
                if ( (rminv < rmaxv) AND (rmaxv <= 10) AND (minok = 0) AND (maxok = 0) )
then
                    begin
                    ok := TRUE;
                    minv := round(rminv * 4095 / 10);
                    if minv < $0001 then minv := $0001;
                    minvax := minv;
                    maxv := round(rmaxv * 4095 / 10);
                    maxvax := maxv;
                    end;  {if}
                end;    {while}
            Bar(1,61,308,90);
            OutTextXY(1,61,'Scan limits are set.');
            Sound(500); Delay(100); NoSound; Delay(500);
            Bar(1,61,308,70);
            disppars;
        end;  {Set scan limits}

    33 : begin {Alt-F}  {Read File}
            ChToUsWind;
            SetColor(Yellow);
            Bar(1,61,308,80);
            OutTextXY(1,61,'Enter file name:');
            OutTextXY(1,71,'(Program will add .dat to name)');
            GetStr(name);
            {$I-}
            assign(data, name + '.dat');
            reset(data);
            if IOResult = 0 then
                begin
                datafile[df] := name;
                readln(data, minv, maxv);
                PESdata[df,1,1] := minv;
                PESdata[df,2,1] := maxv;
                minvax := minv;
                maxvax := maxv;
                readln(data, resolution, timeperpoint);
                PESdata[df,1,2] := resolution;
                PESdata[df,2,2] := timeperpoint;
                for i := 3 to (((maxv - minv) div resolution) + 4) do
                   begin
                   read(data, word1);
                   PESdata[df,1,i] := word1;
                   read(data, word1);
                   PESdata[df,2,i] := word1;
                   end;  {for}
                close(data);
                Bar(1,61,308,80);
                OutTextXY(1,61,'File has been read.');
                gotdata[df] := TRUE;
                DoKey(TRUE,34);
                end {if}
             else begin
```

```
            Bar(1,61,308,70);
            OutTextXY(1,61,'File not found in this directory.');
            end; {else}
        {$I+}
        Sound(800); Delay(250); NoSound;
        Delay(250);
        Bar(1,61,308,80);
    end; {Read File}

19 : begin {Alt-R} {Set Resolution}
        ChToUsWind;
        SetColor(Black);
        ok := FALSE;
        while ok = FALSE do
            begin
            Str(resolution, tempstr);
            Bar(1,61,308,90);
            OutTextXY(1,61,'Current Resolution is ' + tempstr);
            OutTextXY(1,71,'Input new resolution (2.44mV/unit),');
            OutTextXY(1,81,'range 1 to 1000:');
            GetStr(TempStr);
            Val(TempStr, tempint, intok);
            if (tempint > 0) AND (tempint <= 1000) AND (intok = 0) then
                begin
                ok := TRUE;
                resolution := tempint;
                end; {if}
            end; {begin}
        disppars;
        Bar(1,61,308,90);
    end; {Set Resolution}

18 : begin {Alt-E} {Set Numsweeps}
        ChToUsWind;
        SetColor(White);
        ok := FALSE;
        while ok = FALSE do
            begin
            Bar(1,61,308,70);
            OutTextXY(1,61,'Enter Number of Sweeps');
            GetStr(TempStr);
            Val(TempStr, tempint, strok);
            if ((tempint > 0) AND (tempint < 100000) AND (strok = 0)) then
                begin
                ok := TRUE;
                numsweeps := tempint;
                end; {if}
            end; {while}
        Bar(1,61,308,70);
        OutTextXY(1,61,'Number of Sweeps is set.');
        disppars;
        Bar(1,61,308,70);
    end; {Set Numsweeps}
```

```
32 : begin {Alt-D}  {Set Dwell Time}
       ChToUsWind;
       SetColor(white);
       ok := FALSE;
       while ok = FALSE do
           begin
           Bar(1,61,308,70);
           OutTextXY(1,61,'Enter Dwell in ms: (10ms minimum)');
           GetStr(TempStr);
           Val(TempStr, pause, strok);
           if ((pause >= 10) AND (pause < 65000) AND (strok = 0)) then
               ok := TRUE;
           end;    {while}
       Bar(1,61,308,70);
       OutTextXY(1,61,'Dwell Time is set.');
       disppars;
       delay(500);
       bar(1,61,308,70);
   end; {Set Dwell Time}

46 : begin {Alt-C}  {Change Directory}
       ChToUsWind;
       SetColor(Black);
       GetDir(0,OldD);
       Bar(1,61,308,70);
       OutTextXY(1,61,'Current Directory is '+ OldD);
       Bar(1,71,308,80);
       OutTextXY(1,71,'Input new directory or "q" to escape');
       GetStr(TempD);
       if (TempD <> 'q') and (TempD <> 'Q') then
          begin
          {$I-}
          ChDir(TempD);
          {I+}
          if IoResult <> 0 then
              begin
              Bar(1,61,308,70);
              OutTextXY(1,61,'Directory not found.');
              ChDir(OldD);
              sound(1000); Delay(500); NoSound;
              end  {if}
          else OutTextXY(1,81,'Directory Changed.');
          end;  {if}
       Bar(1,61,308,90);
   end;   {Change Directory}

21 : begin {Alt-Y}  {Y Zoom}
       ChToUsWind;
       SetColor(Cyan);
       ok := FALSE;
       while ok = FALSE do
           begin
           Str(zoomy,TempStr);
           Bar(1,61,308,90);
```

```
            OutTextXY(1,61,'Note: Axis labels will not be zoomed.');
            OutTextXY(1,71,'Old Y Zoom is ' + TempStr);
            OutTextXY(1,81,'Enter New Y Zoom');
            GetStr(TempStr);
            Val(TempStr, TempReal, strok);
            if (TempReal > 0) AND (TempReal < $FFF) AND (strok = 0) then
               begin
               ok := TRUE;
               zoomy := tempreal;
               end; {if}
            end; {begin}
         Sound(300); Delay(500); NoSound;
         Bar(1,61,308,90);
         DoKey(TRUE,34);
      end; {Y Zoom}

   45 : begin {Alt-X} {X Zoom}
         ChToUsWind;
         SetColor(Cyan);
         ok := FALSE;
         while ok = FALSE do
            begin
            Str(zoomx:3:3, TempStr);
            Bar(1,61,308,90);
            OutTextXY(1,61,'Note: Points will zoom; axis labels');
            OutTextXY(1,71,'will not. Old X Zoom is ' + TempStr);
            OutTextXY(1,81,'Enter New X Zoom');
            GetStr(TempStr);
            Val(TempStr, TempReal, strok);
            if (TempReal > 0) AND (TempReal < $FFF) AND (strok = 0) then
               begin
               ok := TRUE;
               zoomx := TempReal;
               end; {if}
            end; {begin}
         Sound(350); Delay(500); NoSound;
         Bar(1,61,308,90);
         DoKey(TRUE, 34);
      end; {X Zoom}

   23 : begin {Alt-I} {Integrate between cursors}
         ChToUsWind;
         reso := PESdata[df,1,2];
         CheckPhase;
         for j := 1 to 2 do
            begin
            integrl[j] := 0;
            if CursorPos[2*j-1] > CursorPos[2*j] then
               begin
               lo := CursorPos[2*j];
               hi := CursorPos[2*j-1];
               end {if}
            else begin
               lo := CursorPos[2*j-1];
```

```
                hi := CursorPos[2*j];
                end; {else}
            i := lo;
            while i <= hi do
                begin
                tempint := round(-(i / reso) + 3 + (maxv / reso)) + offset[df];
                integrl[j] := integrl[j] + PESdata[df,2,tempint];
                i := i + reso;
                end; {while}
            end; {for}
        updateint;
    end; {Integrate}

104,105,106,107,59,60,61,62 : begin {Alt-F(1..4), F(1..4)} {Set Active Cursor}
        j := BACK;
        DrawCursor(j);
        if keycode > 103 then ActiveCursor := keycode - 103
            else ActiveCursor := keycode - 58;
        j := FORE;
        DrawCursor(j);
    end; {Set active cursor}

75,79 : begin {left arrow, end} {Move active cursor left, slow or fast.}
        reso := PESdata[df,1,2];
        CheckPhase;
        j := ERASE;
        DrawCursor(j);
        Tempword := CursorPos[ActiveCursor];
        CursorPos[ActiveCursor] := Tempword + round(keycode*reso*19/4 + reso*(1-
(75*19/4)));
        if ((CursorPos[ActiveCursor] > maxvax) OR (CursorPos[ActiveCursor] > 4095)) then
            CursorPos[ActiveCursor] := maxvax;
        j := FORE;
        DrawCursor(j);
        updatecurswind;
    end; {MoveCursor left}

77,81 : begin {right arrow, PgDn} {Move active cursor right slow or fast.}
        j := ERASE;
        DrawCursor(j);
        Tempword := CursorPos[ActiveCursor];
        reso := PESdata[df,1,2];
        CheckPhase;
        CursorPos[ActiveCursor] := Tempword - round(keycode*reso*19/4 + reso*(1-
(77*19/4)));
        if ((CursorPos[ActiveCursor] < minvax) OR (CursorPos[ActiveCursor] > 4095)) then
            CursorPos[ActiveCursor] := minvax;
        j := FORE;
        DrawCursor(j);
        updatecurswind;
    end; {MoveCursor right}

112, 113, 67, 68 : begin {F9, F10, Alt-F9 or F10} {Toggle Active Data Set}
    tempdf := df;
```

```
    if ((keycode = 112) OR (keycode = 67)) then
        df := 1
    else df := 2;
    if df <> tempdf then
        begin
        minv := PESdata[df,1,1];
        maxv := PESdata[df,2,1];
        resolution := PESdata[df,1,2];
        timeperpoint := PESdata[df,2,2];
        DoKey(TRUE, 34);
        end;
    SetColor(LightGreen);
    Bar(1,61,308,70);
    OutTextXY(1,61,'Active Data Set Toggled.');
    Sound(750);  Delay(200);  NoSound;  Delay(300);
    Bar(1,61,308,70);
    end;  {Toggle Active Data Set}

44 :  begin  {Alt-Z}  {Double Display}
    ChToUsWind;
    Bar(1,61,308,90);
    SetColor(LightGreen);
    ok := FALSE;
    while ok = FALSE do
        begin
        Str(offset[2]:3, tempstr);
        OutTextXY(1,61,'Data 2 offset ' + tempstr + ' resolution units.');
        OutTextXY(1,71,'Input new data 2 offset (int):');
        GetStr(TempStr);
        Val(TempStr, tempint, intok);
        if (tempint > -4095) and (tempint < 4095) and (intok = 0) then
            begin
            ok := TRUE;
            offset[2] := tempint;
            end;  {if}
        end; {while}
    ok := FALSE;
    while ok = FALSE do
        begin
        Str(scl2:3, tempstr);
        Bar(1,61,308,80);
        OutTextXY(1,61,'Data 2 scalar is ' + tempstr);
        OutTextXY(1,71,'Input new data set 2 scalar:');
        GetStr(TempSTr);
        Val(TempStr, tempreal, strok);
        if (strok = 0) then
            begin
            ok := TRUE;
            scl2 := tempreal;
            end; {if}
        end; {while}
        graphtrue := TRUE;
        tempdf := df;
        df := 1;
```

```
                erasegraph := TRUE;
                graphdata;
                df := 2;
                erasegraph := FALSE;
                graphdata;
                df := tempdf;
                erasegraph := TRUE;
                Bar(1,61,308,80);
            end;

        30 : begin {Alt-A} {Combine two data sets}
            ChToUsWind;
            SetColor(Black);
            Bar(1,61,308,90);
            if((gotdata[1] = TRUE) AND (gotdata[2] = TRUE)) then
                begin
                {$I-}
                OutTextXY(1,61,'Scaled and offset data 2, added to');
                OutTextXY(1,71,'data 1, will be stored as data 1.');
                OutTextXY(1,81,'Enter Alt-S to save data 1.');
                ok := TRUE;
                if PESdata[1,1,2] <> PESdata[2,1,2] then ok := FALSE;
                if ok = FALSE then
                    begin
                    Delay(500);
                    Bar(1,61,308,90);
                    OutTextXY(1,61,'Data sets incompatible.');
                    OutTextXY(1,71,'Sets must have same resolution.');
                    Sound(440); Delay(500); NoSound; Delay(500);
                    end {if}
                else begin
                    resp := PESdata[1,1,2];
                    minvp := PESdata[1,1,1];
                    if ((PESdata[2,1,1]+offset[2]*resp) > minvp) then minvp :=
PESdata[2,1,1]+offset[2]*resp;
                    maxvp := PESdata[1,2,1];
                    if ((PESdata[2,2,1]+offset[2]*resp) < maxvp) then maxvp :=
PESdata[2,2,1]+offset[2]*resp;
                    newpes[1,1] := minvp;
                    newpes[2,1] := maxvp;
                    newpes[1,2] := resp;
                    newpes[2,2] := PESdata[1,2,2] + PESdata[2,2,2];
                    for i := 1 to (((maxvp - minvp) div resp) + 1) do
                        begin
                        tmpi1 := i + ((PESdata[1,2,1] - maxvp) div resp) + 2;
                        tmpi2 := i + ((PESdata[2,2,1] - maxvp) div resp) + 2 + offset[2];
                        newpes[1,i+2] := maxvp - ((i-1) * resp);
                        newpes[2,i+2] := PESdata[1,2,tmpi1] + round(scl2*(PESdata[2,2,tmpi2]));
                        end; {for}
                    df := 1;
                    for i := 1 to (((maxvp - minvp) div resp) + 3) do
                        begin
                        PESdata[1,1,i] := newpes[1,i];
                        PESdata[1,2,i] := newpes[2,i];
```

```
                    end; {for}
                  datafile[1] := 'nonamesum';
                  graphdata;
                  end;
                {$I+}
                end {if}
              else begin
                OutTextXY(1,61,'One of data sets 1,2 does not exist.');
                Sound(450); Delay(500); NoSound; Delay(500);
                end; {else}
              Bar(1,61,308,90);
              end; {Combine two data sets}

            17 : begin {Alt-W} {Set View Window}
                  ChToUsWind;
                  SetColor(Cyan);
                  ok := FALSE;
                  okdokey := FALSE;
                  Str((maxvax * 10 / 4095):3:2, TempStr1);
                  Str((minvax * 10 / 4095):3:2, TempStr2);
                  while ((ok = FALSE) OR (okdokey = FALSE)) do
                    begin
                    Bar(1,61,308,90);
                    OutTextXY(1,61,'Current graph window is from ');
                    OutTextXY(1,71,TempStr1 + ' to ' + TempStr2 + ' V.');
                    OutTextXY(1,81,'Enter new values:');
                    GetStr(TempStr);
                    Val(TempStr, TempReal, strok);
                    if ((strok = 0) AND (TempReal > -0.01) AND (TempReal < 10.01)) then
                      begin
                      ok := TRUE;
                      maxvax := round(TempReal * 4095 / 10);
                      end; {if}
                    GetStr(TempStr);
                    Val(TempStr, TempRl, strok);
                    if ((strok = 0) AND (TempRl < TempReal) AND (TempRl >= 0)) then
                      begin
                      okdokey := TRUE;
                      minvax := round(TempRl * 4095 / 10);
                      end; {if}
                    end; {while}
                  Bar(1,61,308,90);
                  OutTextXY(1,61,'Graph window is set.');
                  Sound(440); Delay(500); NoSound; Delay(500);
                  Bar(1,61,308,90);
                  DoKey(TRUE,34);
                end; {Set View Window}

          end;   {case}
    end;       {procedure dokey}
end.           {unit dokeyu}


{              CURSORS.PAS              }
```

```
{   Unit of cursor handling routines    8/3/92  MSJ       }
unit CURSORS;

interface

procedure updateint;  {prints values of integrals to cursor window}
procedure updatecurswind;  {updates position information of active cursor}
procedure curswind;  {Draws cursor window containing position & integral data}
procedure checkphase;  {makes sure cursors are in phase with resolution}
procedure drawcursor( var ccolor : integer);   {Draws active cursor in }
                {selected color: 1-foreground 2-background 3-erase}
implementation

uses GRAPH, CRT, GLOBALS, DOS, GRAPHU;

procedure checkphase;

   var  mxmores, i,j  : integer;
      ok  :  boolean;

   begin
      mxmores := maxv mod resolution;
      for i := 1 to 4 do
         begin
         ok := FALSE;
         while (ok = FALSE) do
            begin
            j := CursorPos[i] mod resolution;
            if j = mxmores then ok := TRUE
            else if j/resolution >= 0.5 then
                  CursorPos[i] := CursorPos[i] + 1
               else CursorPos[i] := CursorPos[i] - 1;
            end;  {while}
         end;  {for}
   end;  {procedure checkphase}

procedure drawcursor(var ccolor : integer);

   var reso, pixcolor, i : integer;
      cchar : string;
      cpacx, cpacy : word;
      ysc : real;

   begin
      ChToGrWind;
      i := black;
      reso := PESdata[df,1,2];
      if ccolor = FORE then SetColor(LightGreen)
         else if ccolor = BACK then SetColor(Magenta)
         else SetColor(Black); {because ccolor must be ERASE}
      Str(ActiveCursor, cchar);
      cpacx := CursorPos[ActiveCursor];
      cpacy := round(-(cpacx / reso) + 3 + (maxv / reso)) + offset[df];
      if df = 1 then
```

```
            begin  pixcolor := white; ysc := 1;  end
        else begin  pixcolor := yellow; ysc := scl2;  end;
        if ccolor <> ERASE then

PutPixel(round((cpacx*slopex)+xoff),round(((PESdata[df,2,cpacy])*slopey*ysc)+yoff),lightmagenta)
        else

PutPixel(round((cpacx*slopex)+xoff),round(((PESdata[df,2,cpacy])*slopey*ysc)+yoff),pixcolor);
        OutTextXY(round((cpacx * slopex) + xoff), 2, cchar);
        ChToUsWind;

    end;  {procedure drawcursor}

procedure curswind;  {Draws cursor window}

    type  intstr = array[1..2] of string;
          curstr = array[1..4] of string;

    var  i,j : integer;
        istr : intstr;
        cstr : curstr;
        tempreal : real;

    begin
        ChToUsWind;
        Bar(312,61,615,90);
        SetColor(Cyan);
        for i := 1 to 2 do
            Str(integrl[i],istr[i]);
        for i := 1 to 4 do
            begin
            tempreal := CursorPos[i]*10/4095;
            Str(tempreal:3:2, cstr[i]);
            end;  {for}
        OutTextXY(312,61,'1-> ' + cstr[1]);
        OutTextXY(463,61,'3-> ' + cstr[3]);
        OutTextXY(312,71,'2-> ' + cstr[2]);
        OutTextXY(463,71,'4-> ' + cstr[4]);
        OutTextXY(312,81,'Int-> ' + istr[1]);
        OutTextXY(463,81,'Int-> ' + istr[2]);
    end;  {procedure curswind}

procedure updateint;

    var  istr1, istr2 : string;

    begin
        Str(integrl[1]:8, istr1);
        Str(integrl[2]:8, istr2);
        SetColor(Cyan);
        Bar(360,81,462,90);
        OutTextXY(360,81,istr1);
        Bar(511,81,615,90);
        OutTextXY(511,81,istr2);
```

```
    end;  {procedure updateint}

procedure updatecurswind;

    var  xc, yc : integer;
         cstr : string;
         tempreal : real;

    begin
         SetColor(Cyan);
         tempreal := CursorPos[ActiveCursor] * 10 / 4095;
         Str(tempreal:4:3,cstr);
         case ActiveCursor of
              1 : begin  xc := 344;  yc := 61;  end;
              2 : begin  xc := 344;  yc := 71;  end;
              3 : begin  xc := 495;  yc := 61;  end;
              4 : begin  xc := 495;  yc := 71;  end;
         end;  {case}
         Bar(xc,yc,xc + 118,yc + 9);
         OutTextXY(xc,yc,cstr);
    end;  {procedure updatecurswind}

end.  {unit CURSORS}

{                ADJVOLT.PAS                }

{Adjvolt.pas written 8/22/92 MSJ to correct error in data files}
{$I-}  {IO checking off, is done through IOResult.}
program adjvolt;

uses DOS, CRT;

var  minv, maxv, resolution, timeperpoint, voltage, counts : integer;
     i, stop  :  integer;
     infl, outfl  :  text;
     inname, outname  :  pathstr;
     str1, str2  :  string;

begin
      inname := getenv('INPUT') + '.dat';
      outname := getenv('OUTPUT') + '.dat';
      writeln('input is ' + inname + '   output is ' + outname);
      if IOResult = 0 then
           begin
           assign(infl, inname);
           assign(outfl, outname);
           reset(infl);
           rewrite(outfl);
           Readln(infl, minv, maxv);
           Readln(infl, resolution, timeperpoint);
           minv := minv - 1;  maxv := maxv -1;
           Str(minv, str1);  Str(maxv, str2);
           Writeln(outfl, str1 + ' ' + str2);
           Str(resolution, str1);  Str(timeperpoint, str2);
```

```
        Writeln(outfl, str1 + ' ' + str2);
        i := 1;
        Stop := ((maxv - minv) div resolution) + 1;
        while ((eof(infl) = FALSE) AND (IOResult = 0) AND (i <= Stop)) do
           begin
           readln(infl, voltage, counts);
           voltage := voltage - 1;
           Str(voltage, str1);  Str(counts, str2);
           writeln(outfl, str1 + ' ' + str2);
           i := i + 1;
           end;  {data adjusting loop}
        end;  {output file exists branch}
    close(infl);
    close(outfl);
end.


{              QLLS.PAS              }
{This program will perform a linear least squares fit of PES data.}
{Initial basis functions will be 1, x, x^2, but this can be changed}
{by altering procedure funcs.   MSJ 9/92}
program qlls;

uses DOS, CRT;

const    MAP = 3;
       NDATAP = 30;
       MA = 3;
       MFIT = 3;

type     RealArrayMAbyMA = ARRAY [1..map,1..map] OF real;
       IntegerArrayMA = ARRAY [1..map] OF integer;
       RealArrayNDATA = ARRAY [1..ndatap] OF real;
       RealArrayMA = ARRAY [1..map] OF real;
       IntegerArrayMFIT = ARRAY [1..map] OF integer;
       RealArrayMAbyMP = ARRAY [1..map,1..1] OF real;

var      i, stop  :  integer;
       minv, maxv, res, tpp, voltage  :  integer;
       infl, outfl  :  text;
       inname, outname  :  pathstr;
       str1, str2  :  string;
       xval  :  integer;
       x, y, sig  :  RealArrayNDATA;
       a  :  RealArrayMA;
       lista  :  IntegerArrayMFIT;
       covar  :  RealArrayMAbyMA;
       chisq  :  real;

PROCEDURE funcs(x: real;
      VAR afunc: RealArrayMA;
          ma: integer);

var      i  :  integer;
```

```
        xval : real;

begin
    xval := 1;
    for i := 1 to ma do
        begin
        afunc[i] := xval;
        xval := xval * x;
        end;
end; {procedure funcs}

{PROCEDURE covsrt(VAR covar: RealArrayMAbyMA;
                  ma: integer;
              VAR lista: IntegerArrayMFIT;
                  mfit: integer);
VAR
  j,i: integer;
  swap: real;
BEGIN
  FOR j := 1 TO ma-1 DO
    FOR i := j+1 TO ma DO covar[i,j] := 0.0;
  FOR i := 1 TO mfit-1 DO BEGIN
    FOR j := i+1 TO mfit DO
      IF lista[j] > lista[i] THEN
        covar[lista[j],lista[i]] := covar[i,j]
      ELSE
        covar[lista[i],lista[j]] := covar[i,j]
  END;
  swap := covar[1,1];
  FOR j := 1 TO ma DO BEGIN
    covar[1,j] := covar[j,j];
    covar[j,j] := 0.0
  END;
  covar[lista[1],lista[1]] := swap;
  FOR j := 2 TO mfit DO
    covar[lista[j],lista[j]] := covar[1,j];
  FOR j := 2 TO ma DO
    FOR i := 1 TO j-1 DO
      covar[i,j] := covar[j,i]
END;}

PROCEDURE gaussj(VAR a: RealArrayMAbyMA;
                 n: integer;
             VAR b: RealArrayMAbyMP;
                 m: integer);
VAR
  big,dum,pivinv: real;
  i,icol,irow,j,k,l,ll: integer;
  indxc,indxr,ipiv: ^IntegerArrayMA;
BEGIN
  new(indxc);
  new(indxr);
  new(ipiv);
  FOR j := 1 TO n DO ipiv^[j] := 0;
```

```
FOR i := 1 TO n DO BEGIN
  big := 0.0;
  FOR j := 1 TO n DO
    IF ipiv^[j] <> 1 THEN
      FOR k := 1 TO n DO
        IF ipiv^[k] = 0 THEN
          IF abs(a[j,k]) >= big THEN BEGIN
            big := abs(a[j,k]);
            irow := j;
            icol := k
          END
        ELSE IF ipiv^[k] > 1 THEN BEGIN
          writeln('pause 1 in GAUSSJ - singular matrix');
          readln
        END;
  ipiv^[icol] := ipiv^[icol]+1;
  IF irow <> icol THEN BEGIN
    FOR l := 1 TO n DO BEGIN
      dum := a[irow,l];
      a[irow,l] := a[icol,l];
      a[icol,l] := dum
    END;
    FOR l := 1 TO m DO BEGIN
      dum := b[irow,l];
      b[irow,l] := b[icol,l];
      b[icol,l] := dum
    END
  END;
  indxr^[i] := irow;
  indxc^[i] := icol;
  IF a[icol,icol] = 0.0 THEN BEGIN
    writeln('pause 2 in GAUSSJ - singular matrix');
    readln
  END;
  pivinv := 1.0/a[icol,icol];
  a[icol,icol] := 1.0;
  FOR l := 1 TO n DO
    a[icol,l] := a[icol,l]*pivinv;
  FOR l := 1 TO m DO
    b[icol,l] := b[icol,l]*pivinv;
  FOR ll := 1 TO n DO
    IF ll <> icol THEN BEGIN
      dum := a[ll,icol];
      a[ll,icol] := 0.0;
      FOR l := 1 TO n DO
        a[ll,l] := a[ll,l]-a[icol,l]*dum;
      FOR l := 1 TO m DO
        b[ll,l] := b[ll,l]-b[icol,l]*dum
    END
END;
FOR l := n DOWNTO 1 DO
  IF indxr^[l] <> indxc^[l] THEN
    FOR k := 1 TO n DO BEGIN
      dum := a[k,indxr^[l]];
```

```
        a[k,indxr^[l]] := a[k,indxc^[l]];
        a[k,indxc^[l]] := dum
      END;
  dispose(ipiv);
  dispose(indxr);
  dispose(indxc)
END;

PROCEDURE lfit(VAR x,y,sig: RealArrayNDATA;
               ndata: integer;
               VAR a: RealArrayMA;
                 ma: integer;
             VAR lista: IntegerArrayMFIT;
               mfit: integer;
             VAR covar: RealArrayMAbyMA;
             VAR chisq: real);
VAR
  k,kk,j,ihit,i: integer;
  ym,wt,sum,sig2i: real;
  beta: ^RealArrayMAbyMP;
  afunc: ^RealArrayMA;
BEGIN
  new(beta);
  new(afunc);
  kk := mfit+1;
  FOR j := 1 TO ma DO BEGIN
    ihit := 0;
    FOR k := 1 TO mfit DO
      IF lista[k] = j THEN ihit := ihit+1;
    IF ihit = 0 THEN BEGIN
      lista[kk] := j;
      kk := kk+1
    END
    ELSE IF ihit > 1 THEN BEGIN
      writeln('pause in routine LFIT');
      writeln('improper permutation in LISTA');
      readln
    END
  END;
  IF kk <> ma+1 THEN BEGIN
    writeln('pause in routine LFIT');
    writeln('improper permutation in LISTA');
    readln
  END;
  FOR j := 1 TO mfit DO BEGIN
    FOR k := 1 TO mfit DO covar[j,k] := 0.0;
    beta^[j,1] := 0.0
  END;
  FOR i := 1 TO ndata DO BEGIN
    funcs(x[i],afunc^,ma);
    ym := y[i];
    IF mfit < ma THEN
      FOR j := mfit+1 TO ma DO
        ym := ym-a[lista[j]]*afunc^[lista[j]];
```

```
    sig2i := 1.0/sqr(sig[i]);
    FOR j := 1 TO mfit DO BEGIN
      wt := afunc^[lista[j]]*sig2i;
      FOR k := 1 TO j DO
        covar[j,k] := covar[j,k]+wt*afunc^[lista[k]];
      beta^[j,1] := beta^[j,1]+ym*wt
    END
  END;
  IF mfit > 1 THEN BEGIN
    FOR j := 2 TO mfit DO
      FOR k := 1 TO j-1 DO covar[k,j] := covar[j,k]
  END;
  gaussj(covar,mfit,beta^,1);
  FOR j := 1 TO mfit DO
    a[lista[j]] := beta^[j,1];
  chisq := 0.0;
  FOR i := 1 TO ndata DO BEGIN
    funcs(x[i],afunc^,ma);
    sum := 0.0;
    FOR j := 1 TO ma DO
      sum := sum+a[j]*afunc^[j];
    chisq := chisq+sqr((y[i]-sum)/sig[i])
  END;
{  covsrt(covar,ma,lista,mfit);  }  {Not needed now}
  dispose(afunc);
  dispose(beta)
END;

begin
    inname := getenv('INPUT') + '.dat';
    outname := getenv('OUTPUT') + '.dat';
    writeln('input is ' + inname + '   output is ' + outname);
    if IOResult = 0 then
        begin
        assign(infl, inname);
        assign(outfl, outname);
        reset(infl);
        rewrite(outfl);
        readln(infl, minv, maxv);
        readln(infl, res, tpp);
        voltage := maxv - round(NDATAP * res / 2);
        str(minv + round(NDATAP * res / 2), str1);  str(voltage, str2);
        writeln(outfl, str1 + ' ' + str2);
        str(res, str1);  str(tpp, str2);
        writeln(outfl, str1 + ' ' + str2);
        for i := 1 to MFIT do
            lista[i] := i;
        for i := 1 to NDATAP do
            sig[i] := 1;
        for i := 1 to NDATAP - 1 do
            readln(infl, x[(i mod NDATAP) + 1], y[(i mod NDATAP) + 1]);
        i := NDATAP;
        stop := ((maxv - minv) div res) - NDATAP + 1;
        while((eof(infl) = FALSE) AND (IOResult = 0) AND (i <= stop)) do
```

```
            begin
            readln(infl, x[(i mod NDATAP) + 1], y[(i mod NDATAP) + 1]);
            lfit(x, y, sig, NDATAP, a, MA, lista, MFIT, covar, chisq);
            xval := round(a[1] + a[2] * voltage + a[3] * voltage * voltage);
            str(voltage, str1);  str(xval, str2);
            writeln(outfl, str1 + ' ' + str2);
            voltage := voltage - res;
            i := i + 1;
            end;
        end;
    close(infl);
    close(outfl);
end.
```

Appendix C:

Infrared Spectrum of the Silicon Hydride Cation SiH_7^+

J. Phys. Chem. 1993, 97, 5215–5217 5215

Infrared Spectrum of the Silicon Hydride Cation SiH_7^+

Yibin Cao, Jong-Ho Choi, Bernd-Michael Haas, Matthew S. Johnson, and Mitchio Okumura*

Arthur Amos Noyes Laboratory of Chemical Physics,† California Institute of Technology, Pasadena, California 91125

Received: March 12, 1993; In Final Form: April 2, 1993

We report the infrared spectrum of the silicon hydride cluster ion SiH_7^+ obtained by vibrational predissociation spectroscopy. SiH_7^+ ions were excited by a tunable infrared laser, and the resulting SiH_5^+ photofragment intensity was measured as a function of the laser wavelength. We observed a vibrational band centered at 3866 cm^{-1}, which we assigned as a perturbed H_2 stretch. The absence of a second band between 3500 and 4200 cm^{-1} suggests that the ion forms a symmetric complex with the structure $H_2{\cdot}SiH_3^+{\cdot}H_2$, in contrast to the species CH_7^+, which has the structure $CH_5^+{\cdot}H_2$.

Introduction

Silanium ions are an important class of hypervalent molecules. Investigations of the chemistry of silicon hydride cations have been motivated by the possible role of ion–molecule reactions in the gas-phase silane chemistry occurring during chemical vapor deposition (CVD) of silicon films, especially plasma-enhanced CVD. Both experimental[1-9] and theoretical[10-13] studies have focused on reactions of Si^+ and SiH_3^+ with silane that produce hydrogenated silicon cluster ions $Si_nH_m^+$. Theoretical calculations[10-13] suggest that these cluster ions exhibit rather novel nonclassical bonding, analogous to but distinct from the nonclassical bonding observed in carbonium ions. Such bonding is believed to occur even in monosilane cluster ions such as SiH_5^+.[15]

Although the gas-phase chemistry of silicon hydride ions has been studied extensively, there have been few spectroscopic studies to date. Whitham *et al.* have obtained electronic predissociation spectra of SiH^+ and SiH_2^+ by using a fast ion beam apparatus.[16-18] Dyke *et al.*[19] have reported the frequency of the out-of-plane bending mode of SiH_3^+ from the photoelectron spectrum of the SiH_3 radical. Smith, Martineau, and Davies[20] have recently reported a high-resolution infrared absorption spectrum of the ν_3 band of the SiH_3^+ cation detected in a glow discharge. SiH_3^+ is the dominant ion in low-pressure silane discharges, and no other species have thus far been detected by this method.

Based on the analysis of the rotationally resolved ν_3 band, the SiH_3^+ cation has a classical trigonal planar structure like CH_3^+. In the case of SiH_5^+, *ab initio* calculations by Hu *et al.* suggest that an H_2 is bound to SiH_3^+ through a three-center, two-electron bond. This bonding is analogous to the case of CH_5^+, but the SiH_3^+–H_2 bond is weaker. The best theoretical estimate of the dissociation energy D_0 for SiH_5^+ is 10.3 kcal/mol, less than the experimental value of 17.8 kcal/mol.[4] Larger silicon hydride cations are expected to be more weakly bound. The SiH_7^+ ion has not been previously observed experimentally, and theoretical calculations on its structure have not yet been carried out.

Using an ion trapping tandem mass spectrometer apparatus, Lee and co-workers have obtained infrared vibrational predissociation and multiphoton photodissociation spectra for a number of ionic clusters.[21-24] This technique has proved to be a powerful method for obtaining spectra of mass-selected clusters. We have developed a simpler apparatus using pulsed techniques, based on the ion photodissociation spectrometer developed by Johnson and Lineberger.[25] We have begun to apply the vibrational predissociation method to silicon hydride cations, and in this paper we report our initial results on the infrared spectrum of the SiH_7^+ cation.

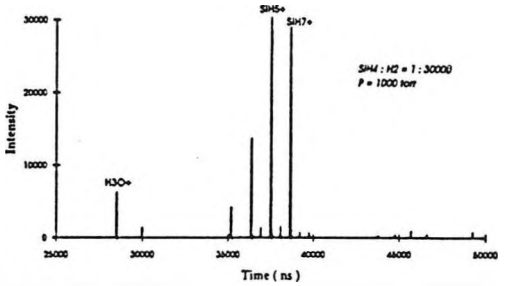

Figure 1. Time-of-flight mass spectrum of the silanium ions. The pulsed valve stagnation pressure was 1000 Torr. The gas mixing ratio SiH_4:H_2 was 1:30 000.

Experimental Section

Silanium ions were generated in a pulsed, high-pressure glow discharge source which we developed recently. A MKS gas flow control system was used to produce a mixture of 30 ppm SiH_4 in H_2 at 1000 Torr. This gas mixture expanded through a piezo-driven pulsed valve[26] (pulse width 200 μs) into a 0.5-mm-diameter channel. The gas then entered a small chamber with two tungsten electrodes (0.5-mm diameter) where a high-voltage pulse (typically ~1 kV, 100 μs wide) was applied to the cathode. Ions in the discharge were swept out by the gas pulse through a 1-mm-diameter, 1.5-cm-long channel and into the first differential vacuum chamber (pumped by a 10-in. baffled diffusion pump and maintained at a pressure of $(2–10) \times 10^{-5}$ Torr). This plasma was cooled as the gas flowed through the channel and underwent supersonic expansion. The effectiveness of the cooling was demonstrated by the formation of cluster ions with binding energies of 3 kcal/mol or less such as $H_3O^+{\cdot}H_2$. A typical time-of-flight mass spectrum is shown in Figure 1. The source, operated at a repetition rate of 30 Hz, produced intense and stable silanium ion beams.

The plasma expanded supersonically and was collimated by a skimmer to enter a second chamber (6-in. diffusion pump, 5×10^{-6} Torr) containing time-of-flight ion optics. A pulsed electric field between two plates 3 cm apart extracted the positive ions. The ions were further accelerated by additional electric fields and then entered a field-free region with a final kinetic energy of 1 keV. After passing through a third differential pumping region (4-in. diffusion pump, 1×10^{-6} Torr) and into a photolysis/detection chamber (500 L/s turbomolecular pump, 3×10^{-7} Torr), the ions entered a 1-cm-long mass gate where a pulsed transverse field was applied to deflect all incident ions except those of the mass of interest. The selected ions were focused into a packet

† Contribution No. 8760.

0022-3654/93/2097-5215$04.00/0

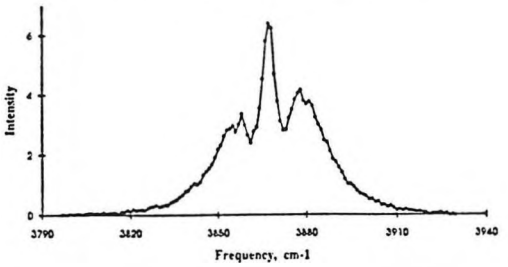

Figure 2. Vibrational predissociation spectrum of the SiH_7^+ ion in the 3800–3925-cm^{-1} region. No other predissociation bands were observed from 3500 to 4200 cm^{-1}.

9 mm long and 5 mm in diameter at 1.5 m downstream from the acceleration optics, where they were intersected by the infrared laser beam. The ions were then mass-analyzed by a 15-cm-long reflectron,[22] and the photofragments were detected by a microchannel plate detector. The signal was amplified and then collected by a LeCroy Model 8818 transient digitizer and Model 6010 signal averager.

The tunable, pulsed infrared radiation was produced by a $LiNbO_3$ optical parametric oscillator (OPO). The OPO, based on the design of Brosnan and Byer,[27] was pumped by a Continuum 661s Nd:YAG laser which generated 250-mJ pulses at 1.06 μm. To avoid damaging the $LiNbO_3$ crystal, the pump beam was multipassed 14 m to achieve a Gaussian intensity profile at the OPO entrance. The OPO was continuously tunable from 2700 to 4300 cm^{-1} by simultaneously adjusting the crystal and the grating angles. Typical OPO pulse energies were about 5 mJ with a line width of 1.5 cm^{-1}. The optical path from the laser to the vacuum chamber was purged with dry air to eliminate absorption caused by ambient water vapor.

Spectra were recorded by stepping the OPO wavelength and averaging the photofragment signal for 400 laser shots at each wavelength. To achieve a better signal-to-noise ratio, we averaged 10 such scans. Background signal, primarily caused by collision-induced dissociation in the ion optics chamber, was subtracted by firing the laser beam alternately at the parent ion arrival time and 10 μs before the ion arrival and taking the difference. The data were then normalized with respect to the OPO laser intensity, measured by a Molectron joulemeter. The OPO laser wavelength was calibrated during the scan by simultaneously recording the vibrational spectrum of acetylene in a photoacoustic cell.

Results and Discussion

An absorption band of SiH_7^+ was observed in the 3800–3925-cm^{-1} region, as shown in Figure 2. This band has clear P, Q, and R branches, with the Q branch centered at 3866 cm^{-1}. The only photofragment ion observed was SiH_5^+, indicating that the photodissociation process involved was $SiH_7^+ \rightarrow SiH_5^+ + H_2$. Due to the broad line width of the OPO laser (1.5 cm^{-1}), rotational structure of this band was not resolved. There were no other absorptions found from 3500 to 4200 cm^{-1}.

On the basis of the relatively high frequency and the strength of this absorption band, we assign it to an H–H stretching motion. This stretch is strongly perturbed, as evidenced by its 300-cm^{-1} frequency shift from the free H_2 fundamental of 4161 cm^{-1}. This assignment supports the notion that SiH_7^+ is an ionic cluster with at least one H_2 molecule bound to the charge center. The H–H stretch excitation in a free H_2 molecule is dipole forbidden; thus, the H–H stretch in the SiH_7^+ obtains its transition dipole moment through coupling with degrees of freedom that possess oscillator strength, e.g., motion of the charge center relative to the center of mass.

The observed frequency of 3866 cm^{-1} for SiH_7^+ is close to the harmonic frequency of 3991 cm^{-1} for SiH_5^+ predicted by Hu *et al.*, given that *ab initio* frequencies are generally 5–10% higher than experimental values. This agreement at first suggests that SiH_7^+ could be a complex with an H_2 molecule very weakly bound to the SiH_5^+ ion core, analogous to the structure proposed by Boo, Price, and Lee for the CH_7^+ ion (Figure 3B).[23] However, this H_2 moiety would be perturbed by the SiH_5^+ core and therefore exhibit an absorption band slightly below 4161 cm^{-1}, the vibrational frequency of a free H_2. In all previous cases involving an ion–molecule cluster with H_2 ligands, such an absorption band has been observed. In the case of CH_7^+, this absorption band occurs at 4077 cm^{-1}. We scanned the region from 3500 to 4200 cm^{-1}, but SiH_7^+ showed no evidence of a second absorption band. In addition, we observed that the SiH_7^+ ions could exist even under "hot" source conditions that made mostly SiH^+ ions, which suggests that the SiH_7^+ binding energy is quite large, much greater than the CH_7^+ binding energy of 1–2 kcal/mol.[23]

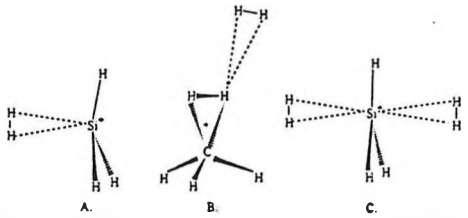

Figure 3. (A) SiH_5^+ structure predicted by Hu, Shen, and Schaefer. (B) CH_7^+ structure based on the experimental results of Boo, Price, and Lee. (C) The proposed structure of SiH_7^+.

We therefore propose that SiH_7^+ has the structure shown in Figure 3C: a planar SiH_3^+ with two H_2 ligands bound to opposite faces of the ion, equidistant from the Si atom. The H_2 most likely bind perpendicular to the SiH_3^+ symmetry axis, with the σ electrons donating into the empty p orbital of the silicon cation. Sideways binding generally occurs for molecular hydrogen in ion–molecule complexes, e.g., SiH_5^+ [15] and H_{2n+1}^+,[21] as well as in transition-metal dihydrogen complexes.[28] This structure is a near-prolate top. The two H_2 ligands rotate around the symmetry axis with a small energy barrier. This structure should result in two H–H stretching bands: the symmetric and antisymmetric combinations of the two H_2 stretches. The antisymmetric motion, with the two H_2 ligands vibrating 180° out of phase, will cause the Si^+ charge center to oscillate along the symmetry axis as it moves toward the extended H_2. This gives rise to the observed parallel band, which has apparent P, Q, and R branches. The symmetric combination, in which the two H_2 ligands expand and contract in phase, will induce little movement of the charge center and thus should have much weaker absorption intensity. Our current interpretation of the spectrum is that the symmetric combination is in fact weaker and obscured by the stronger antisymmetric mode.

In previous spectroscopic work on ion–molecule clusters with an H_2 ligand, a semiquantitative correlation between the frequency of the H–H stretching mode and the binding energy of that cluster was observed. The larger the frequency shift from the free H_2 fundamental, the more strongly the H_2 moiety is bound. With a frequency shift of 300 cm^{-1}, the SiH_7^+ binding energy is estimated as 7–9 kcal/mol. This crude binding energy estimate is about half of the experimental value of the SiH_5^+ binding energy, supporting the proposed structure of SiH_7^+, in which both of the H_2 ligands compete for the charge on the silicon atom.

Our proposed structure for SiH_7^+ is quite distinct from the structure proposed by Boo *et al.* for CH_7^+.[23] The differences can be rationalized by comparing the CH_5^+ and SiH_5^+ ions. The dissociation energy for $CH_5^+ \rightarrow CH_3^+ + H_2$ is 40 kcal/mol, and the strong three-center, two-electron bond in CH_5^+ results in charge delocalization among the three centers. In contrast, the dissociation energy for $SiH_5^+ \rightarrow SiH_3^+ + H_2$ is only 17.8 kcal/mol. The SiH_5^+ ion is thus closer to an $SiH_3^+ \cdot H_2$ complex, as

Hu *et al.* predict.[15] A second H_2 will bind to the Si atom, where most of the charge remains localized.

These results shed some light on the nonclassical structures of SiH_5^+ and SiH_7^+. A more definitive structure determination requires recording the rotationally resolved spectrum. If the H_2 ligands are about 2 Å from the planar SiH_3^+, then SiH_7^+ is a prolate top with a rotational constant B of 0.85 cm^{-1}. A fit to our unresolved infrared spectrum results in a rotational temperature of 90 K. Our newly upgraded OPO has a line width of 0.15 cm^{-1} and will easily resolve the spectra. The next step in silanium ion spectroscopy would be SiH_5^+. Since the dissociation energy for $SiH_5^+ \rightarrow SiH_3^+ + H_2$ is 17.8 kcal/mol, SiH_5^+ spectra can be obtained through two-photon photodissociation. Larger silicon hydride ions are also believed to possess unusual geometries. In $Si_2H_7^+$, for example, the two Si atoms are thought to bond through an H atom, with a structure of $H_3Si\text{-}H^+\text{-}SiH_3$. By using multiphoton dissociation techniques, we hope to probe the structure and novel bonding of these species as well.

Acknowledgment. We gratefully acknowledge the support of a NSF Presidential Young Investigator Award CHEM-8957243. Additional support was received from a Dreyfus Newly Appointed Faculty Award, the Irvine Foundation, the Chevron Fund, an AT&T Special Purpose Grant, and a Grace Fellowship (M.S.J.). We thank D. W. Boo and Prof. Y. T. Lee for their unpublished results.

References and Notes

(1) Yu, T. Y.; Cheng, T. M. H.; Kempten, V.; Lampe, F. W. *J. Phys. Chem.* 1972, *76*, 3321.
(2) Henis, J. M. S.; Stewart, G. W.; Tripodi, M. K.; Gaspar, P. P. *J. Chem. Phys.* 1972, *57*, 389.
(3) Cheng, T. M. H.; Yu, T. Y.; Lampe, F. W. *J. Phys. Chem.* 1974, *78*, 1184.
(4) Boo, B. H.; Armentrout, P. B. *J. Am. Chem. Soc.* 1987, *109*, 3549.
(5) Mandich, M. L.; Reents Jr., W. D.; Jarrold, M. F. *J. Chem. Phys.* 1988, *88*, 1703.
(6) Reents Jr., W. D.; Mandich, M. L. *J. Phys. Chem.* 1988, *92*, 2908.
(7) Mandich, M. L.; Reents Jr., W. D. *J. Chem. Phys.* 1989, *90*, 3121.
(8) Mandich, M. L.; Reents Jr., W. D.; Kolenbrander, K. D. *J. Chem. Phys.* 1990, *92*, 437.
(9) Reents Jr., W. D.; Mandich, M. L. *J. Chem. Phys.* 1990, *93*, 3270.
(10) Raghavachari, K. *J. Chem. Phys.* 1988, *88*, 1688.
(11) Raghavachari, K. *J. Phys. Chem.* 1988, *92*, 6284.
(12) Raghavachari, K. *J. Chem. Phys.* 1990, *92*, 452.
(13) Al-Laham, M. A.; Raghavachari, K. *J. Chem. Phys.* 1991, *95*, 2560.
(14) Olah, G. A.; Prakash, G. K. S.; Williams, R. E.; Field, L. D.; Wade, K. *Hypercarbon Chemistry*; Wiley-Interscience: New York, 1987.
(15) Hu, C. H.; Shen, M.; Schaefer III, H. F. *Chem. Phys. Lett.* 1992, *190*, 543.
(16) Curtis, M. C.; Jackson, P. A.; Sarre, P. J.; Whitham, C. J. *Mol. Phys.* 1985, *56*, 485.
(17) Sarre, P. J.; Walmsley, J. M.; Whitham, C. J. *Philos. Trans. R. Soc. London, A* 1988, *324*, 233.
(18) Hall, D. I.; Levick, A. P.; Sarre, P. J.; Whitham, C. J.; Alijah, A.; Duxbury, G. *J. Chem. Soc., Faraday Trans.* 1993, *89*, 177.
(19) Dyke, J. M.; Jonathan, N.; Morris, A.; Ridha, A.; Winter, M. J. *Chem. Phys.* 1983, *81*, 481.
(20) Smith, D. M.; Martineau, P. M.; Davies, P. B. *J. Chem. Phys.* 1992, *96*, 1741.
(21) Okumura, M.; Yeh, L. I.; Lee, Y. T. *J. Chem. Phys.* 1988, *88*, 79.
(22) Yeh, L. I.; Okumura, M.; Myers, J. D.; Price, J. M.; Lee, Y. T. *J. Chem. Phys.* 1989, *91*, 7319.
(23) Boo, D. W.; Price, J. M.; Lee, Y. T. Preprint.
(24) Price, J. M.; Crofton, M. W.; Lee, Y. T. *J. Phys. Chem.* 1991, *95*, 2182.
(25) Johnson, M. A.; Lineberger, W. C. In *Techniques for the Study of Ion-Molecule Reactions*; Farrar, J. M., Saunders Jr., W. H., Eds.; Wiley-Interscience: New York, 1988; p 591.
(26) Proch, D.; Trickl, T. *Rev. Sci. Instrum.* 1989, *60*, 713.
(27) Brosnan, S. J.; Byer, R. L. *IEEE J. Quantum Electron.* 1979, *QE-15*, 415.
(28) Kubas, G. J. *Acc. Chem. Res.* 1988, *21*, 120.